МОСКОВСКИЙ ГОСУДАРСТВЕННЫЙ УНИВЕРСИТЕТ

имени М.В. ЛОМОНОСОВА

БИОЛОГИЧЕСКИЙ ФАКУЛЬТЕТ

На правах рукописи

Ван Юэци

Особенности структурной организации и взаимодействия хвостатых бактериофагов с биопленкообразующими бактериями

1.5.2 Биофизика

1.1.10 Биомеханика и Биоинженерия

ДИССЕРТАЦИЯ

на соискание ученой степени

кандидата биологических наук

Научный руководитель:

доктор биологических наук, профессор РАН,

Соколова Ольга Сергеевна

Москва – 2026

MOSCOW M.V. LOMONOSOV STATE UNIVERSITY

BIOLOGY DEPARTMENT

As a manuscript

Wang Yueqi

Features of the structural organization and interaction of tailed bacteriophages with biofilm-forming bacteria

1.5.2. Biophysics

1.1.10 Biomechanics and Bioengineering

DISSERTATION

for the degree of

Candidate of Biological Sciences

Supervisor, Doctor of Science, Professor RAS

Olga S. Sokolova

Moscow-2026

Table of Contents

1. List of abbreviations

AMR – Antimicrobial Resistance

CFU – Colony-Forming Unit

c-di-GMP – Cyclic Dimeric Guanosine Monophosphate

CCK-8 – Cell Counting Kit-8

CLSM – Confocal Laser Scanning Microscopy

CRISPR- – Clustered Regularly Interspaced Short Palindromic Repeats

Cas - CRISPR-associated proteins

Cryo-EM – Cryo-Electron Microscopy

Cryo-ET – Cryo-Electron Tomography

CV – Crystal Violet

DAPI – 4',6-Diamidino-2-Phenylindole

DPO – 3,5-Dimethylpyrazin-2-ol

DSM – Defined Synthetic Medium

EPI – Early Phage Infection

EPS – Extracellular Polymeric Substance

FDA – U.S. Food and Drug Administration

LB – Luria-Bertani

MDR – Multidrug-Resistant

MOI – Multiplicity of Infection

NB – Nutrient Broth

OD600 – Optical Density at 600 nm

PAM – Protospacer Adjacent Motif

PAC – Phage-Antibiotic Combination

PBS – Phosphate-Buffered Saline

PEI – Polyethyleneimine

PFU – Plaque-Forming Units

PI – Propidium Iodide

PT – Phage Therapy

QS – Quorum Sensing

RM – Restriction-Modification

SEM – Scanning Electron Microscopy

SF – Silk Fibroin

SFG – Silk Fibroin-Gelatin

SFGC – Silk Fibroin-Gelatin-Chitosan

SM – Saline Magnesium Buffer

TEM – Transmission Electron Microscopy

vOTUs – Viral Operational Taxonomic Units

WHO – World Health Organization

XDR – Extensively Drug-Resistant

2. Introduction

2.1 Relevance of the research topic

Ecological and nosocomial infections caused by multidrug-resistant (MDR) bacteria currently pose a serious threat to public health. Antimicrobial resistance is responsible for over 700,000 deaths annually [1]. Drug resistance urgently necessitates the search for new antibacterial agents. In this context, bacteriophages, especially those of the class Caudoviricetes, are attracting attention as an alternative to antibiotics [2]. In the last decade, the development of phage therapy (PT) applications has become a highly relevant direction.

Bacterial viruses are considered safe for humans and animals, can effectively penetrate the complex structure of biofilms formed by bacteria, and are characterized by high specificity to particular bacteria [3]. For over 90 years in the Soviet Union and the Russian Federation, treatment with bacteriophages, mainly administered orally or topically in liquid form, has been conducted. Both monovalent and combined preparations containing several phages are used [4]. At the same time, biocompatible and biodegradable systems for the delivery and prolonged release of bacteriophages at the site of infection have not yet been developed. There is a lack of comparative data on the interaction of bacteriophages with biofilms formed by Gram-negative and Gram-positive bacteria.

Tailed bacteriophages have a characteristic structure, including a head and a tail [5], which determines their ability to effectively bind to bacterial cells. The multiprotein complex (connector) between the head and tail provides a reliable connection between

the two structures, which is critical for successful bacterial infection. Studying the connector structure will help understand how phages effectively infect host cells and how these processes can be modified for practical application.

This research is dedicated to studying the features of interaction of three bacteriophages of the class Caudoviricetes with Gram-negative bacteria *Acinetobacter baumannii* and *Pseudomonas aeruginosa*, classified by WHO as critical threats due to their ability to form biofilms and increased antibiotic resistance [6], and Gram-positive bacteria *Bacillus subtilis*, also capable of forming biofilms [7]. The high-resolution 3D structure of the head-tail connector of phage TaPaz was investigated, and the formation of early phage infection vesicles (EPIV) by phage phiKZ was demonstrated. New biocompatible substrates for delivering bacteriophages to the infection site were developed, and a search for new tailed phages that destroy biofilms formed by clinical isolates was conducted. Research with a potential focus on developing PT for common bacterial diseases is relevant and one of the most important tasks from a practical point of view.

2.2 Development of the research topic

The goal of PT is to destroy pathogenic bacterial strains without disrupting the balance of the patient's natural microflora undergoing treatment. Most often, lytic and modified phages [8], phage proteins [9], or a combination of phages with antibiotics are used for this purpose. Key factors influencing the pharmacokinetics of bacteriophage preparations include phage adsorption, biodistribution, metabolism, and elimination [10]. Adsorption mainly depends on the method of phage administration [11], its structure, and

size [12]. Giant phages (with a capsid diameter ~150 nm) can infect a wide range of hosts (including both Gram-negative and Gram-positive bacteria). It has been found that some giant phages form pseudo-nuclear structures in bacteria, protecting their genomes from bacterial nucleases [13]. However, how phage DNA is delivered to the phage nucleus in the first minutes after infection has not been established. Phage metabolism can be influenced by environmental pH [14]. Pharmacodynamics, in turn, is related to the antibacterial activity of phage preparations. It is based on the analysis of the multiplicity of infection (MOI). This is an important factor for preventing the development of phage resistance [15].

In hospitals, biofilms formed by pathogenic bacteria are a major problem when using implants. In particular, *P. aeruginosa* most often infects venous and urinary catheters, as well as artificial hip prostheses [16]. Biofilms are formed due to the extracellular matrix (EM) produced by a bacterial population of cells. It is a polyfunctional structure formed on the basis of capsules, pseudocapsules, and extracellular slime synthesized by individual cells. EM components consist of exopolysaccharides (EPS), as well as lipopoly- and lipooligosaccharides, cyclic glucans, and lipoproteins. The EM protects bacterial cells and the biofilms they form from unfavorable environmental conditions and the effects of various abiotic and biotic factors; therefore, bacteria within biofilms are more resistant to various disinfectants and antimicrobial agents [17]. To date, changes in the structure of the biofilm and individual bacterial cells as a result of exposure of antibiotic-resistant clinical isolates of *P. aeruginosa* to bacteriophages have not yet been sufficiently studied.

To use bacteriophages as antimicrobial agents with increased effectiveness,

attempts have been made in recent years to immobilize them on various substrates [18]. This can be achieved through direct physical adsorption [16] or chemical/covalent immobilization [19].

The high-resolution structure of bacteriophages is studied using cryo-electron microscopy (cryo-EM) [20]. Currently, a number of high-resolution structures of individual parts of tailed bacteriophages have been obtained; however, their diversity leads to the constant discovery of new structural features. Particularly diverse is the region connecting the capsid with the tail, including the portal, which regulates the movement of DNA into the capsid during the assembly of the infectious virion and into the host cell during infection [21].

2.3 Goal and objectives of the work

Goal of the work: determine the features of the structural organization and antibacterial action of tailed bacteriophages, as well as the development of bioengineering constructs for their controlled delivery.

To achieve this goal, the following **objectives** were set:

- Study the structural features and interaction of tailed phages with bacterial cells using methods of cryo-electron microscopy and tomography;

- Investigate the effect of selected bacteriophages on the architecture and viability of biofilms formed by clinical isolates and reference strains;

- Develop and characterize new biocompatible substrates/carriers for immobilization, stabilization, and controlled delivery of bacteriophages.

2.4 Scientific novelty

The novelty of the work based on the fact that the effectiveness between phage and biofilms interaction depends on the features of biofilm structural organization. The integrative approach is developed for critical biofilm-forming pathogens, which allows to understand fundamental mechanisms of antibacterial action and to develop new practical strategies to overcome antibiotic resistance.

2.5 Theoretical and practical significance

The theoretical significance of the work lies in deepening the fundamental understanding of the structural-functional organization of bacteriophages and the mechanisms of their interaction with bacterial biofilms. The practical significance consists in developing new, phage-based strategies and biomaterials to combat chronic infections caused by antibiotic-resistant pathogens, contributing to solving the problem of global antimicrobial resistance.

2.6. Methodology

1. Bioengineering: engineering substrates/carriers from silk fibroin functionalized with PEI and bacteriophages for targeted bacteriophage delivery;

2. Biophysics: cryo-EM was used to obtain a reconstruction of the portal complex of phage TaPaz, electron tomography was applied to study EPIV; biofilms and biomaterials (substrates) were characterized using SEM, transmission electron microscopy (TEM); substrates were studied using swelling/degradation analysis, Raman spectroscopy, and IR spectroscopy;

3. Microbiology: quantitative assessment of phage efficacy.

2.7 Provisions put forward for defense

1. An integrated approach combining structural analysis, study of phage interaction with biofilms, and delivery material engineering is an effective strategy for transitioning from the fundamental study of bacteriophages to the development of practical tools to combat antibiotic-resistant infections.

2. As a result of applying the integrated approach, high-resolution structures of key proteins of bacteriophage TaPaz were determined, the dynamics of early infection by bacteriophage phiKZ were visualized, and innovative biomaterials for targeted phage delivery were created.

2.8 Degree of reliability and validation

The reliability of the results presented in the dissertation is determined by the representative volume of conducted experimental research, the comprehensive application of modern research methods, and is confirmed by statistical processing of the obtained data. In the publication (Osire, Wang et al, 2024), the applicant studied the influence of the environment and temperature on the growth and structure of biofilms. In the publication (Antonova, Nichiporenko, Sobinina, Wang et al, 2024), the author studied the early stages of infection using electron tomography. In (Wang et al, 2025), the author conducted work on the formation of biofilms and studied the effect of bacteriophages at different pH levels. In the publication (Osire, Wang, et al, 2024), she developed bacteriophage-functionalized substrates and studied them using TEM and SEM.

3. Literature Review

3.1 Bacteriophage diversity and classification

Bacteriophages (phages), ubiquitous bacterial viruses with an estimated global population of 10^{31} exhibit co-evolutionary relationships with their bacterial hosts and can be found everywhere [22]. Bacteriophages, ubiquitously distributed in natural environments, exhibit remarkable morphological and genetic diversity. Currently classified phages span 4 viral realms, 7 phyla, and 8 classes [23-25]. Classification systems further subdivide phages based on genomic architecture: double-stranded DNA (dsDNA) phages [26], single-stranded DNA (ssDNA) phages [27], double-stranded RNA (dsRNA) phages [28], and single-stranded RNA (ssRNA) phages [29]. Morphotypes of different bacteriophages are shown in Fig.1 [30]. The structures of different bacteriophages vary greatly, yet most types of bacteriophages have capsids or tail structures.

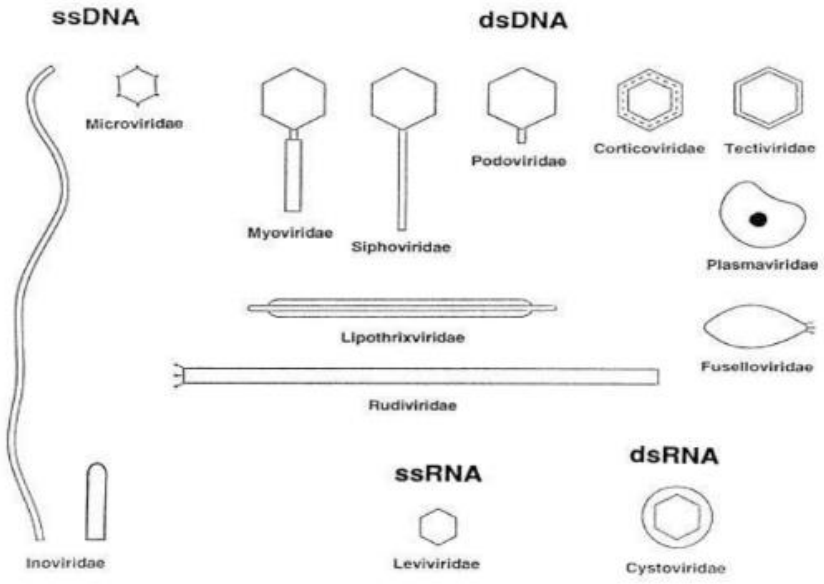

Figure 1 Morphotypes of bacteriophages.[30]

Most characterized phages possess dsDNA genomes. According to morphology, dsDNA phages segregate into tailed (called Caudoviricetes) and tailless forms. Tailed phages are subclassified by the length of the tail and whether it can be contracted: Siphovirus (long noncontractile tails) [31], Podovirus (short noncontractile tails), and Myovirus (contractile tails) [32]. Phylogenetically, these distribute across two realms:

Realm Duplodnaviria, which is characterized by icosahedral capsids containing the conserved HK97-fold major capsid protein. This realm encompasses phylum Uroviricota, class Caudoviricetes, comprising 52 families and 4,863 documented species of bacteria-infecting viruses [33];

Realm Varidnaviria, which is defined by major capsid proteins containing one or two β-barrel domains. Includes families Tectivirus, Corticovirus and Autolykivirus.

Until the end of 2024, the INPHARED database archives 28,468 complete phage genomes (excluding those with uncharacterized hosts), with phylogenetic distribution revealing ~85% in dsDNA realm Duplodnaviria, and ~14% in ssDNA realm Monodnaviria, and only <1% across other realms [34].

Rapid advances in metagenomics and metaviromics have dramatically expanded phage genomic records. The IMG/VR database now catalogs >5 million high-confidence viral genomes, representing 2.9 million viral operational taxonomic units (vOTUs) [35]. In addition, environmental virome studies continue to reveal unprecedented diversity:

Marine ecosystems yield plenty of novel species-level vOTUs [36], also soil viromes [37] and wastewater systems [38] exhibit comparable diversification, which has been greatly expanded the diversity of Caudoviricetes and Leviviricetes phages. Notably, human gut virome analyses from 12 independent studies identify >168,000 species-level

vOTUs—far exceeding all currently classified phage diversity [35]. This richness is evidenced genomically by extreme size variation: from Lactobacillus phage ADMH1 Phi (1,761 bp, smallest known) to Bacillus phage G (497,513 bp), with recent metagenomic studies revealing even larger phages (>540 kbp) in marine and human gut ecosystems [39]. Such genomic plasticity underscores phages' exceptional adaptability, positioning them as ideal candidates for applications in clinical, environmental, and agricultural domains.

3.2 Bacteriophages structure

The Myovirus family represents a major group within the order Caudoviricetes, distinguished by their characteristic contractile tails. These complex, double-stranded DNA phages are potent predators of bacteria and archaea, and their sophisticated structure is finely tuned for efficient host recognition, attachment, and genome delivery. Understanding the structure of myoviruses is important for understanding their infection mechanisms and this can be applicated in biotechnology and medicine. The structure of a Myovirus phage contains an icosahedral head with viral genome inside, collar part, tail sheaths, tail fibres, base plates and pins (Fig. 2) [40].

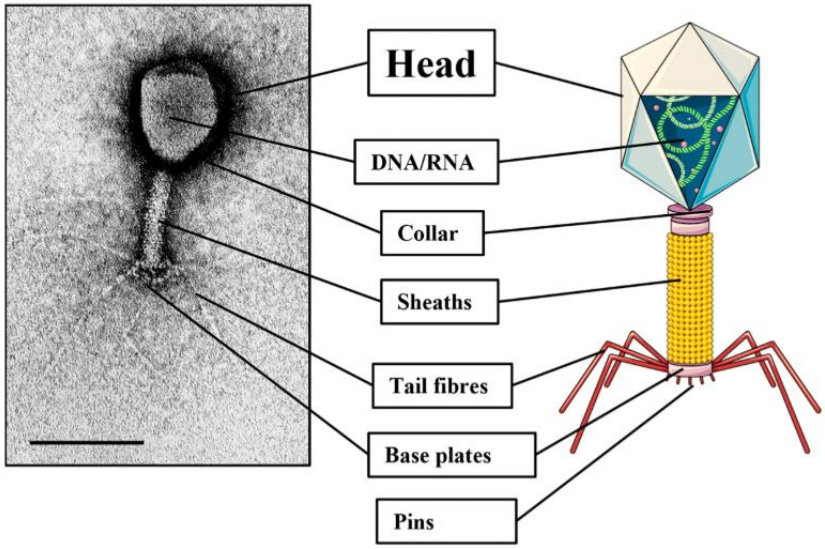

Figure 2 Typical structure of Myovirus [40]

The icosahedral capsid is an icosahedral protein shell (capsid) composed primarily of multiple copies of the major capsid protein. This rigid structure protects the tightly packed, pressurized viral genome (dsDNA).

The portal vertex is a unique 12-fold symmetric structure embedded in one pentameric capsid vertex. It serves as the gateway for genome packaging during virion assembly and subsequent ejection during infection. The portal protein oligomer forms a central channel [41].

The neck / connector complex attached to the portal vertex, which is a multi-protein complex acting as the interface between the capsid and the tail. This complex typically includes the portal itself, adaptor proteins, and a collar structure. The collar often sits atop the tail sheath and may have attached whiskers or fibers involved in stabilization or host sensing. Key proteins in this region act as gatekeepers, sealing the portal channel to prevent premature DNA leakage. Signals from the tail trigger conformational changes in these gatekeepers to open the channel for DNA ejection [42].

The contractile tail is the hallmark feature of Myovirus and consists of three main

components:

Tail Sheath is a large, outer tube which composed of many copies of the tail sheath protein, arranged in a helical lattice. In the pre-infection ("extended") state, the sheath surrounds the inner tube. Upon host recognition, it undergoes a dramatic contraction, sliding over the tail tube and driving it downwards.

Tail Tube is a rigid, internal tube which composed of the tail tube protein, forming a hollow channel through which the viral DNA passes into the host cell. The distal end of the tube is sharpened into the tail needle or spike, which penetrates the host envelope during contraction.

Baseplate is a complex, multi-protein structure located at the distal end of the tail (before contraction). It serves as the central hub for host recognition and signal transduction [43].

3.3 Bacteriophages antimicrobial applications

The antimicrobial potential of phages was first recorded in 1896 by British bacteriologist Ernest Hankin. Then independent confirmations have been emerged in 1917 through the work of Frederick Twort (UK) and Félix d'Hérelle (French-Canadian microbiologist), who formally designated these entities as "bacteriophages" [44]. Pioneering therapeutic applications were established by d'Hérelle in 1919, successfully treating fowl typhoid and bacillary dysentery, which earned him multiple Nobel Prize nominations [45]. After these early successes, phage therapy gained widespread acceptance among clinicians and researchers, leading major pharmaceutical companies for commercial production.

The appearance of penicillin in 1928 leaded a decline in phage therapy adoption across Western nations. However, d'Hérelle kept promoting his work in many countries, including Indonesia, Egypt. India the United States and Soviet Georgia. This leaded to real clinical use there. Consequently, phage therapeutics continued through the mid-20th century, particularly in the Soviet Union and Eastern Bloc nations, where they remained that as main treatments for bacterial dysentery, typhoid, and cholera. The Eliava Institute in Tbilisi, Georgia, studied phages for over eighty years. Today, it is one of the world's largest phage therapy centers. Every year, this institution provides successful interventions for plenty of international patients with multidrug-resistant infections [46].

The mounting worldwide challenge of AMR has already reached to an alarming level, with the global spread of MDR and XDR bacterial pathogens. AMR is predicted to result in 10 million annual deaths by 2050 without effective interventions, representing a significant threat to modern medicine and global health systems. [47]. Facing this intensifying public health crisis alongside the limited development of new antibiotics, scientific focus has shifted towards bacteriophages as targeted therapeutic agents against resistant bacteria.

Consequently, phage therapy infrastructure is experiencing robust revitalization: Belgium has established a national phage repository, the Center for Innovative Phage Applications and Therapeutics operates at UC San Diego, and China has inaugurated five dedicated research institutes for phage-resistant pathogen management. These developments signify phage therapy's emergence as a personalized antimicrobial modality for recalcitrant infections [48]. Furthermore, phages are being deployed as antibiotic alternatives across multiple sectors: Food safety systems (pathogen biocontrol),

Environmental remediation (bacterial load reduction) and Veterinary medicine (prophylaxis against zoonotic pathogens) [49]. Phages, as antibacterial weapons, are widely used in different areas including human medicine, food industry, animal husbandry, and agriculture (Fig.3) [50].

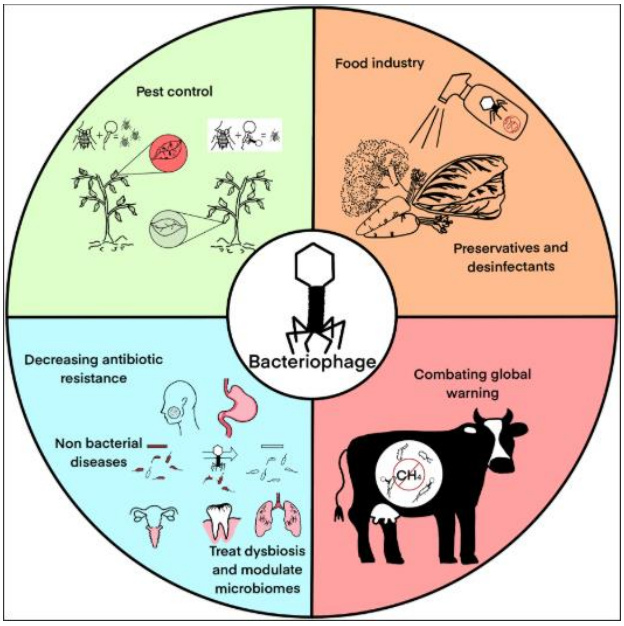

Figure 3 Main bacteriophage applications [50]

The U.S. Food and Drug Administration (FDA) has approved several bacteriophage products for food safety applications in the United States and Europe. Commercial phage cocktails include: (1) ListShield™ (Intralytix)comprising six Herellevirus phages (LIST-36, LMSP25, 1ta-34, 1ta-57, 1ta-94, and 1ta-148) targeting *L. monocytogenes* [51, 52]; (2) PhageGuard L (Listex™), formulated with the broadly lytic phage P100 against *L. monocytogenes* [53]; (3) SalmoFresh™ (Intralytix), containing six Salmonella-specific phages (SPT-1, STML-198, SSE-121, SBA-1781, SKML-39, and STML-13-1) [54].

Global regulatory shifts toward antibiotic restriction in animal agriculture have

intensified since 2022, with international and national agencies implementing comprehensive bans to safeguard animal-derived food safety and public health [55]. This "restrict-reduce-limit" antibiotic paradigm has accelerated development of bacteriophage-based alternatives for veterinary use. Currently, nine phage products hold FDA approval for commercially available for the treatment of infections in companion animals including *Salmonella, Escherichia coli,* and *Staphylococcus aureus* [56].

3.4 Bacteriophages in human medicine

In recent years, amid the global rise of antimicrobial resistance and the scarcity of novel antibiotics, bacteriophage therapy has emerged as a compassionate use option for patients with otherwise untreatable drug-resistant infections. Over 40 registered clinical trials at various stages—accessible via international clinical trial registries—are currently evaluating the safety and efficacy of phage preparations for treating human infections. Additional retrospective studies and foundational research further document phage applications in humans. While no phage products have yet received FDA approval for routine clinical use, phage therapy is sanctioned for emergency deployment in cases where antibiotic treatment has failed. This is particularly relevant for common infections caused by multidrug-resistant bacteria, including wound infections, urinary tract infections, and respiratory infections. Currently, the clinical trials of investigating phage therapy have applied in treating chronic otitis, life-threatening infections, burn wounds, bacterial infections, gastrointestinal disorders, urinary tract infections, venous leg ulcers, and diabetic foot ulcers (Fig.4), with outcomes ranging from completed studies to terminated trials due to lack of efficacy [57].

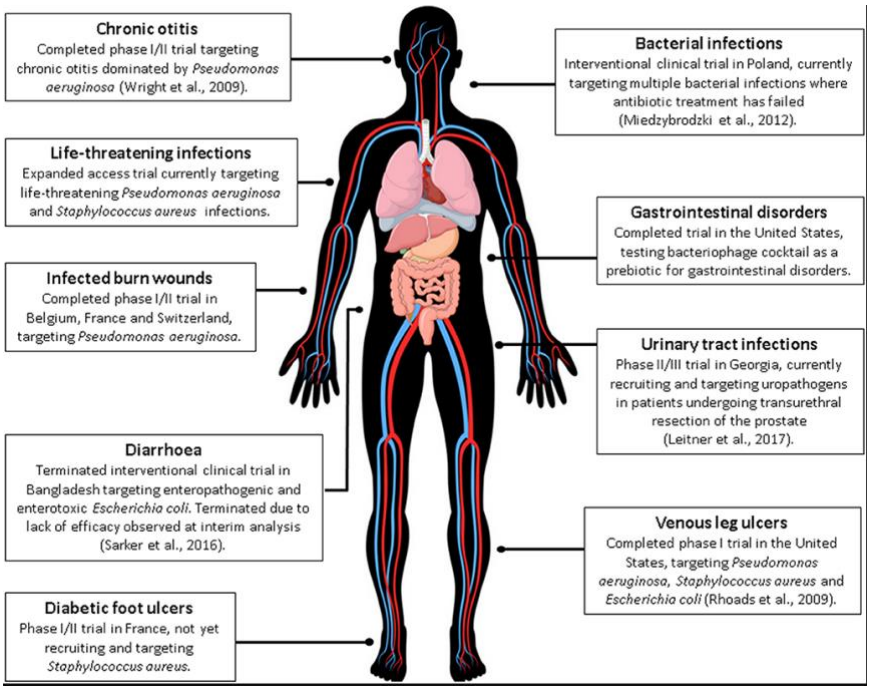

Figure 4 A current summary of human phage therapy trials and the range of target sites/infections [57]

3.4.1 Bacteriophage applications in wound infections

Clinically significant wound infections encompass surgical site infections (SSIs), traumatic wounds, burn wounds, and skin ulcerations. SSIs, defined as infections occurring near the surgical incision within 90 days post-operation, represent one of the most prevalent types of healthcare-associated infections [58, 59]. Leitner et al. [60] combined phage therapy with antibiotics in 474 patients undergoing transurethral resection of the prostate (TURP). Their results indicated that most patients experienced reduced wound symptoms and fewer adverse effects compared to the antibiotic-only group, confirming the efficacy and safety of phage therapy. Similarly, Nadareishvili et al. [61] conducted a retrospective analysis of two patients with chronic osteomyelitis, one with a diabetic foot ulcer, and one experiencing severe infectious complications following skin grafting. Phage therapy improved the overall health status and promoted wound

healing in all cases. Tkhilashvili et al. [62] reported the case of an 80-year-old woman with recurrent periprosthetic knee joint infection caused by multidrug-resistant (MDR) *P. aeruginosa*. Combined treatment involving phage therapy applied to the surgical site and antibiotic-loaded bone spacers resulted in rapid surgical wound healing.

Traumatic wounds are characterized by their complexity, large surface area, high degree of contamination, and infection. They always intend to exhibit infection and a biofilm formation. Traditional antibiotics often lead to resistance, posing significant challenges to patient recovery. Bhartiya et al. [63] treated 54 patients with traumatic wound infections using either phage therapy or antibiotics. Phage therapy demonstrated faster clearance of tissue infection, higher wound healing rates and shorter hospital time. This suggests that the potential superiority over antibiotics for dealing with large traumatic wound infections. Racenis et al. [64] reported a case of MDR *P. aeruginosa* and MDR *Acinobacter baumannii* infection in a trauma wound from a traffic accident, which both debridement and antibiotic therapy were failed. Combination therapy involving antibiotics and topical phage application resolved the clinical symptoms, with no recurrence observed after 9 months of follow-up.

Severe burns, involving compromised skin barriers, are highly susceptible to wound infection, potentially progressing to sepsis and septic shock, leading to significant morbidity and mortality [65]. The bacterial profile of burn wound infections evolves during healing: Gram-positive bacteria like *Staphylococcus epidermidis* dominate early stages, while Gram-negative bacteria, particularly *P. aeruginosa*, are common in later stages [66].

Diabetic patients are prone to foot ulcer infections involving various pathogens.

Staphylococcus aureus and *P. aeruginosa* are significant opportunistic MDR bacteria in diabetic foot infections (DFIs), hindering ulcer healing [67, 68]. Young et al. [67] administered topical phage therapy to 10 diabetic patients with *S. aureus* DFIs at high risk of amputation. Clinical symptoms resolved in 6 patients, preserving their limbs, and the pathogen was completely eradicated in one patient. Furthermore, Mohamed et al. [68] isolated *P. aeruginosa* phages from sewage and tested them in vitro against *P. aeruginosa* strains isolated from 185 DFI patients. The phages demonstrated favorable temperature and pH stability and exhibited broad-spectrum lytic activity against the clinical isolates.

Collectively, these studies confirm that phage therapy demonstrates efficacy against clinically prevalent resistant bacterial wound infections, including surgical sites, traumatic wounds, burns, and skin ulcers. This evidence supports phage therapy's potential as a complementary therapeutic approach for managing antibiotic-resistant infections in patients with challenging wound types.

3.4.2 Use of bacteriophages to treat bacterial biofilm-related infections

Bacterial biofilms represent complex three-dimensional aggregates of bacteria that adhere to biotic or abiotic surfaces and become firmly embedded within an extracellular polymeric substance (EPS) matrix. Their formation typically progresses through five stages: attachment, colonization, development, maturation, and dispersal, with dispersal marking the initiation of new biofilm formation cycles [69].

Biofilms are ubiquitous in all kinds of environments. Bacteria within biofilms exhibit significantly reduced susceptibility to antimicrobial agents and host immune mechanisms compared to their planktonic counterparts, consequently demonstrating

enhanced pathogenicity and resistance [70]. Clinically, biofilms frequently contribute to persistent infections [71], while in industrial contexts, they accelerate corrosion processes and increase the release of harmful byproducts. Furthermore, biofilms provide a "protective barrier" for foodborne pathogens, limiting their exposure to antimicrobial substances and thereby posing serious threats to food safety [72]. Particularly noteworthy is the observation that biofilm formation can increase bacterial resistance to antibiotics by approximately 1,000-fold, substantially complicating biofilm eradication efforts [73].

In the ongoing search for effective strategies against biofilm-associated infections, phages, chelating agents, ultrasound, quorum sensing (QS) inhibitors, and plant-derived bioactive compounds have all demonstrated promising anti-biofilm effects. Among these strategies, phages shown advantages with high specificity, minimal residual effects, rapid self-replication, low dosage requirements, and potential ability for modification. They were established as powerful agents for biofilm-related infections [74].

3.5 Phage - bacterial biofilm interactions

As one of Earth's most abundant microbial resources, bacteriophages use unique mechanisms for disrupting bacterial biofilms, which is different from conventional antibiotics and disinfectants. Phages not only effectively kill bacterial biofilms but also efficiently touch bacteria through the biofilm matrix. This provides novel insights and approaches for treatment of biofilm-associated infections. Fig. 5 demonstrates the dynamic interactions between bacterial biofilm and phage - bacterial biofilm can defend phage through signal molecules, while phages can also produce different types of lyase to inhibit biofilm formation [75].

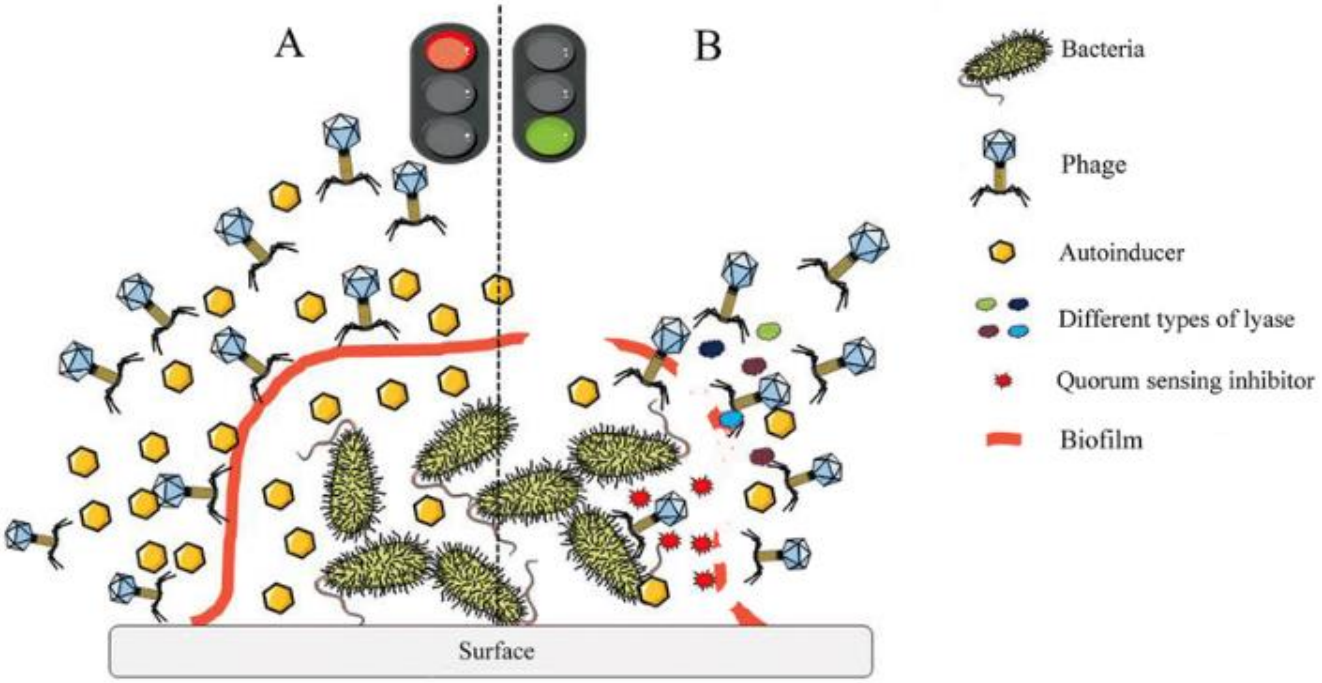

Figure 5 Interactions between bacterial biofilm and phage. (A) Bacterial biofilm formation induced by signal molecules of QS systems lead to resistance to phage. (B) The phage or related substance produced by phage hinders the formation of bacterial biofilm [75].

3.5.1 Enzymatic degradation

Phage genomes encode diverse enzymes—including endolysins, depolymerases, and virion-associated peptidoglycan hydrolases—that degrade cellular components such as peptidoglycan and capsular polysaccharides. These enzymes disrupt biofilm integrity, facilitating efficient phage penetration into the biofilm structure [76]. Among them, endolysins and depolymerases play particularly critical roles, forming the primary foundation for phage-based biofilm control [77].

Endolysins, produced during the terminal phase of the phage replication cycle, specifically degrade peptidoglycan in bacterial cell walls. This action inhibits biofilm formation and enables rapid phage penetration [76]. These enzymes are typically encoded

internally or in localized regions of phage particles, allowing them to cleave peptidoglycan from both intracellular and extracellular directions [78].

Depolymerases often adopt filamentous structures displayed at phage apexes. As tail fiber proteins or free enzymes, they degrade capsular polysaccharides, lipopolysaccharides, O-antigen chains, or biofilm exopolysaccharides, thereby weakening biofilm architecture and promoting phage diffusion [79].

Notably, phages not only encode depolymerases but can also induce host bacteria to produce extracellular polymeric substance (EPS)-degrading depolymerases. These enzymes efficiently hydrolyze polysaccharides and proteins within the EPS matrix, enhancing phage penetration and replication through their lytic activity [80].

3.5.2 Diffusion via biofilm water channels

Biofilms contain specialized water channels whose size-restricted pores impede the penetration of large antimicrobial agents [81]. Phages, however, exploit their small size to diffuse directly through these channels. During diffusion, phages penetrate deeper biofilm layers via gravity-assisted movement while increasing their population without self-concentration depletion [82]. This renders phage diffusion significantly more efficient than antibiotic penetration.

3.5.3 Carrier bacteria-mediated biofilm penetration

Within microbial community ecosystems, phages utilize a unique adsorption mechanism to attach non-specifically or specifically to motile bacteria ("carriers") that penetrate biofilms [80]. Critically, the motility of these carrier bacteria facilitates directed phage migration toward nutrient-rich zones within biofilms. This targeted transport

proves more efficient than random diffusion [81].

3.5.4 Modulation of bacterial quorum sensing systems

Quorum sensing (QS) serves as a critical regulatory mechanism for bacterial collective behavior, governing gene expression through the production and detection of specific small-molecule signaling compounds (autoinducers) within biofilms [83]. When biofilms encounter external stressors (e.g., phages), the QS system fine-tunes the expression of genes involved in synthesizing key biofilm components—such as polysaccharides and extracellular DNA—thereby maintaining biofilm stability [75]. However, while bacteria may modulate QS to resist phage infection, phages can counteract this defense by producing QS inhibitors that disrupt signaling pathways. For example, *P. aeruginosa* phage DMS3 encodes the novel QS anti-activator protein Aqs1, which inhibits the master QS regulator LasR. This interference disrupts QS-mediated anti-phage strategies. Simultaneously, Aqs1 interacts with and inhibits PilB—a type IV pilus assembly protein—impairing bacterial twitching motility and reducing virulence [84].

Beyond secreting QS inhibitors, some phages exploit QS molecules to trigger their lytic cycle. Vibrio cholerae phage VP882 encodes VqmA, a homolog of the vibrio QS receptor transcriptional factor. When VqmA binds to the Vibrio QS autoinducer 3,5-dimethylpyrazin-2-ol (DPO), it not only activates the host gene vqmR (disrupting Vibrio QS pathways) but also induces expression of the phage lysis protein Qtip, initiating the phage lytic program [85]. Thus, phages employ multifaceted strategies to manipulate QS signaling within biofilms—either by disrupting QS cascades or co-opting QS molecules

to induce lysis—thereby inhibiting biofilm formation and maturation.

Notably, QS systems play pivotal roles in biofilm dispersion. In *P. aeruginosa*, the LasI/LasR QS system positively regulates tyrosine phosphatase A synthesis, which suppresses pel gene expression and reduces cyclic dimeric guanosine monophosphate (c-di-GMP) levels. This reduction in intracellular c-di-GMP promotes biofilm dispersion—a mechanism now recognized as a novel strategy for biofilm eradication [69]. Regarding whether bacteriophages can influence the content of c-di-GMP in biofilms by regulating the QS system, and thereby becoming a potential biofilm dispersant, further research will further explore more possibilities in this field.

3.5.5 Targeting persister bacteria

Persister bacteria represent a transient, antibiotic-tolerant dormant subpopulation within biofilms or planktonic bacteria [81]. While antibiotics primarily target metabolically active bacteria, dormant persisters may reactive after treatment discontinuation, leading to recurrent biofilm formation [86]. Phages exhibit distinct advantages in this context: they effectively infect and lyse dormant persisters while capable of entering a reversible, hibernation-like state upon invasion. This phage dormancy allows reactivation upon nutrient restoration to resume biofilm disruption [81].

3.5.6 Overcoming bacterial RM and CRISP1R-Cas defense systems

Bacteria employ two well-characterized defense systems—restriction-modification (RM) and clustered regularly interspaced short palindromic repeats with CRISPR-associated proteins (CRISPR-Cas)—to recognize and cleave phage DNA at specific genomic loci, thereby safeguarding their genomes [87]. Nevertheless, phages have

evolved sophisticated counterstrategies to subvert these immune mechanisms.

The RM system relies on restriction enzyme (REases) to degrade foreign DNA at recognition sites [88]. Phages circumvent this through multiple approaches: they utilize methyltransferases (MTases) to modify their own genomes, effectively camouflaging them as host DNA; co-inject specialized proteins (e.g., DarA and DarB encoded by phage P1) that mask restriction sites; and produce anti-restriction proteins (e.g., Ral from phage λ) that enhance MTase activity while inhibiting REases [89]. Additionally, some phages minimize vulnerability by maintaining genomes with sparse restriction sites or positioning existing sites beyond functional cleavage distances, thereby evading detection [88].

CRISPR-Cas systems—comprising CRISPR sites and cas genes—represent the only known adaptive and heritable bacterial immunity [65]. However, phages neutralize this defense through diverse tactics, including the production of anti-CRISPR proteins (e.g., Acr) that directly inactivate CRISPR-Cas immune complexes and evade recognition through mutations in protospacer adjacent motifs (PAMs) or seed sequences, deletion of protospacer regions, or chemical modification of protospacer DNA, all of which impair CRISPR RNA targeting [81]. Jumbo phages deploy an even more sophisticated strategy by forming nucleus-like compartments that sequester phage DNA, physically blocking Cas complex assembly and preventing targeted cleavage [90].

Notably, covalent modifications of phage genomes—such as heteromethylation and glucosylation—confer resistance to CRISPR systems while enabling rapid evolutionary adaptation under selective pressure [87]. This phenomenon underscores a profound interconnection between RM and CRISPR-Cas defenses rather than their

functional isolation. Critically, these evasion mechanisms collectively empower phages to penetrate bacterial immunity, thereby enhancing their capacity to disrupt biofilm-associated infections.

3.5.7 Mechanisms of phage-antibiotic synergy in combating bacterial biofilm-associated infections

The synergistic effects observed when combining phages with antibiotics are attributed to multiple interconnected mechanisms. Firstly, while extracellular polymeric substances (EPS) impede antibiotic diffusion, phages penetrate the biofilm matrix and compromise bacterial cell walls, thereby enhancing antibiotic permeability and efficacy [91]. Secondly, suitable antibiotic concentrations can amplify phage activity—demonstrated by agents like meropenem and ceftazidime increasing plaque size of *P. aeruginosa* phage KPP22 by 2-3-fold [92]. Thirdly, antibiotic-induced filamentation of bacterial cells exposes peptidoglycan layers, rendering bacteria more susceptible to phage-encoded lytic enzymes [93]. Fourthly, this combination therapy impedes the development of antibiotic resistance while substantially reducing the emergence of phage-resistant mutants [94]. Fifthly, the synergistic effect of bacteriophages and antibiotics may also be due to the reduction of the minimum inhibitory concentration of antibiotics [95].

Nevertheless, the precise mechanisms governing how phage-antibiotic interactions within biofilms modulate host immune responses remain poorly characterized and warrant further investigation.

3.6 Methodologies for studying phage-bacteria interactions

3.6.1 Direct visualization techniques

Direct visualization techniques provide uncomparable insights into the physical interactions and morphological transformations occurring in the phage infection cycle. Transmission Electron Microscopy (TEM) stands as a cornerstone technique for ultrastructural analysis. By transmitting a beam of electrons through a thin specimen, TEM can generate high-resolution, two-dimensional images based on different electron density. This capability makes it crucial for characterizing the intricate structure of phages, including the icosahedral heads, contractile or non-contractile tails, baseplates, and attachment fibers. Furthermore, TEM is also crucial for confirming the distinct stages of infection, such as the specific adsorption of phages to bacterial surface and the injection of viral genetic material. And it is also important for visualizing the intracellular assembly of progeny virions in the infected host cell. The primary strength of TEM is its great resolution for revealing nanoscale details. However, this comes with significant limitations, including sample preparation with chemical fixation, dehydration, resin embedding, and ultrathin sectioning, which can be introduced artifacts. And also the inability to observe dynamic processes in real-time as samples are fixed and examined in vacuum. Ackermann et al. provides a foundational reference on phage morphology with the usage of TEM [30].

Complementing TEM, Scanning Electron Microscopy (SEM) offers detailed topographical information about surface morphology. SEM works by scanning a focused beam of electrons across the sample surface and detecting secondary or backscattered

electrons, then generating 3D-like images. This technique is particularly useful for examining the surface interactions between phages and bacteria, revealing the spatial distribution of phage infection. SEM also perform excellent in visualizing the structural disruption of bacterial biofilms by phages or phage-derived depolymerases. This may allow researchers to observe the breakdown of the extracellular matrix and changes in biofilm structure before and after treatment. While SEM provides excellent surface detail, sample preparation also requires fixation and dehydration, and it typically does not offer the internal structural detail as TEM.

3.6.2. Quantifying antibacterial effects

Beyond structural visualization, quantitative methods are essential for measuring the results of phage infection, particularly the antibacterial efficacy. The Plaque Assay is still the most fundamental and widely used method for quantifying viable, lytic phage particles and determining the host range. This method is to mix phages with susceptible bacteria in a soft agar, which overlay on a solid agar plate. Each infectious phage particle infects a bacterium, lyses it, and releases progeny that infect neighboring cells, creating a visible clearing or "plaque" in the bacterial lawn after incubation. Counting these plaques allows the determination of the phage titer (plaque-forming units, PFU/mL). Closely related is the Efficiency of Plating (EOP) assay, which compares the plaque-forming ability of a phage on different bacterial strains relative to a reference host. EOP is crucial for assessing the host range specificity of a phage, a critical parameter for therapeutic applications. While simple and highly informative, plaque assays require actively growing host cells and may not detect phages with non-lytic or chronic infection cycles

[96].

To measure the kinetics of bacterial killing by phages in liquid culture, Growth Curves monitored by Optical Density at 600 nm (OD600) and Time-Kill Assays are employed. Growth curves involve inoculating bacteria with phages at a specific multiplicity of infection (MOI) and measuring the turbidity (OD600) of the culture at regular intervals. Phage-mediated lysis typically results in a characteristic drop in OD600 after an initial growth period. Time-kill assays provide a more direct and dynamic measure of bacteriolytic activity. Samples are taken from the infected culture at specific time points, serially diluted, and plated on solid agar to determine the number of surviving colony-forming units (CFU/mL). Plotting log CFU/mL versus time reveals the rate and extent of bacterial killing by the phage over the course of the infection. These assays are vital for evaluating phage potency under various conditions and comparing different phage candidates or treatment regimens. Hyman. P. et al. comprehensively covers methods for quantifying phage growth and killing kinetics [97].

Biofilms represent a significant challenge in bacterial infections due to their inherent resistance to antibiotics. Crystal Violet (CV) Staining is a widely adopted, colorimetric method for quantifying total biofilm biomass. Biofilms are grown under static or flow conditions in microtiter plates or other suitable surfaces. After incubation, non-adherent cells are removed by washing, and the remaining adherent biofilm is stained with crystal violet, a dye that binds to negatively charged surface molecules and extracellular DNA in the biofilm matrix. The bound dye is then dissolved in a solvent (like ethanol or acetic acid), and the absorbance of the solution is measured, providing a quantitative correlate of the total biofilm biomass. This assay is extensively used to assess

the efficacy of phages or phage-derived depolymerases in preventing biofilm formation or eradicating pre-formed biofilms by measuring the reduction in stained biomass compared to untreated controls. While simple and high-throughput, CV staining does not distinguish between live and dead cells within the biofilm. O'Toole, G. A. is the canonical protocol for this essential biofilm quantification method [98].

3.7 Targeting strains: *P. aeruginosa* and *B. subtilis*

Understanding the fundamental principles of phage-bacteria interactions necessitates the use of well-characterized model organisms. *B. subtilis* and *P. aeruginosa* represent two important models and offer distinct advantages and insights due to their different biological characteristics. *B. subtilis* is a Gram-positive, which were found commonly in soil and associated with plants. It has long served as a basic model organism in molecular biology and microbiology. It is easy for genetically study, because of a fully sequenced genome and a plenty of well-developed genetic tools for manipulation, which make it suitable for dissecting the molecular mechanisms of phage infection. Researchers can generate targeted gene knockouts, introduce specific mutations, and use fluorescent reporters to track gene expression and cellular processes in real-time during phage infection. *B. subtilis* have a relatively simple cell envelope structure compared to Gram-negatives, facilitating the study of phage adsorption. Furthermore, its ability to form complex biofilms provides a robust system for investigating how phages interact with and disrupt bacterial communities. The well-characterized phages corresponding *B. subtilis*, such as the large myoviruses SPO1 and SPP1 or the podovirus φ29, provide a rich toolbox for exploring different infection strategies, including the dynamics of genome injection,

replication, and host takeover mechanisms [99].

In contrast, *P. aeruginosa*, the Gram-negative opportunistic pathogen, is studied primarily due to its profound clinical importance and its resistance mechanisms. It is a major cause of severe, chronic and difficult-to-treat infections, particularly in immunocompromised persons, cystic fibrosis patients (where it colonizes the lungs with thick biofilms) and burnt patients. *P. aeruginosa* exhibits high intrinsic and acquired resistance to a wide range of antibiotics, driving the urgent search for alternative therapeutics like phage therapy. Its complex, multi-layered cell envelope, featuring an outer membrane rich in lipopolysaccharide (LPS), a thin peptidoglycan layer, and efflux pumps, presents significant barriers that phages must overcome, making it an excellent model for studying adsorption mechanisms and resistance evolution (e.g., through LPS modification). *P. aeruginosa* is also renowned for its ability to form robust, antibiotic-tolerant biofilms on both biotic and abiotic surfaces, a key virulence factor. Consequently, it is a premier model for investigating phage-biofilm interactions, including the efficacy of phage-encoded depolymerases in degrading the biofilm matrix polysaccharides (e.g., alginate, Psl, Pel) and the ability of phages to penetrate and replicate within these structured communities. The extensive collection of well-studied phages infecting *P. aeruginosa*, including podoviruses (e.g., LUZ7, LKD16), myoviruses (e.g., PAK_P1, PB1), and siphoviruses (e.g., D3112), allows researchers to probe diverse infection cycles and host range determinants relevant to clinical applications [100]. The study of phage interactions with both *B.subtilis* and *P.aeruginosa* thus provides complementary insights, spanning fundamental molecular mechanisms in a genetically amenable host to the complex challenges of combating resilient, biofilm-forming pathogens in clinical settings.

4. Materials and Methods

4.1 Bacteria and phages used in this work

4.1.1 Bacteria isolates used in the work

LAMME Wuxi (China), kindly provided *B. subtilis* 168, the phage's host strain.

Standard laboratory strain *P. aeruginosa* PAO1 is a museum laboratory strain from the collection of the Laboratory of Bacteriophage Genetics at the I.I. Mechnikov Research Institute of Bacteriophage Genetics.

Clinical isolates of *P. aeruginosa* used in this work are antibiotic-resistant strains obtained from patients with chronic urologic (19 pcs.) infections, from the collection of the Laboratory of Bacteriophage Genetics of the I.I. Mechnikov Research Institute of Bacteriophage Genetics. Received earlier from the I.I. Mechnikov Research Institute of Urology. Previously obtained from N.A. Lopatkin Research Institute of Urology, Research Institute of Pulmonology of FMBA of Russia, Museum of Bacterial Cultures of I.M. Sechenov First Moscow State Medical University, Institute of Microbiology and Epidemiology named after N.F. Gamaley. N.F. Gamaley Institute of Microbiology and Epidemiology.

4.1.2 Bacteriophages used in the work

PhiAR9 purified phage was a gift from Dr Maria Yakunina (Peter the Great St.Petersburg Polytechnic University (SPbPU).

Tapaz: Purified phage was a gift from Dr Konstantin Miroshnikov (Institute of Bioorganic Chemistry RAS, Moscow).

Species phiKZ: phages phiKZ, phiNN, phiOP were isolated in the Laboratory of Bacteriophage Genetics of the I.I. Mechnikov Research Institute of Bacteriophage Genetics from different sources. Species KMV: bacteriophage phiNFS, phiFMV - isolated in the Laboratory of Bacteriophage Genetics of the I.I. Mechnikov Research Institute of Bacteriophage Genetics from a natural source.

PB1 species: phage phiPB1 was obtained earlier from Prof. H. Ackerman (Canada) from the Lindberg typing collection; phages phi10/2 and phi14/1 were isolated in the Laboratory of Bacteriophage Genetics of the I.I. Mechnikov Research Institute of Bacteriophage Genetics from natural sources.

4.2 Phage propagation and purification

4.2.1 Solution preparation

LB (Luria-Bertani) Liquid Medium: Tryptone (10 g), yeast extract (5 g), and NaCl (10 g) were weighed and dissolved in 950 mL of deionized water. Following dissolution, the pH was adjusted to 7.0 using 5 mol/L NaOH. The solution was brought to a final volume of 1 L with deionized water, sterilized at 121 ℃ for 20 minutes, and stored at 4 ℃ until use.

LB (Luria-Bertani) Solid Medium: Tryptone (10 g), yeast extract (5 g), NaCl (10 g), and agar (15 g) were weighed and dissolved in 950 mL of deionized water. Following dissolution, the pH was adjusted to 7.0 using 5 mol/L NaOH. The solution was brought to a final volume of 1 L with deionized water and sterilized at 121 ℃ for 20 minutes. After cooling sufficiently, the medium was poured into disposable sterile Petri dishes. Once the agar solidified, the plates were inverted and placed on a laminar flow hood

overnight at room temperature to evaporate residual moisture. The plates were subsequently stored at 4 ℃ until use.

Semi- LB Solid Medium: Agar was dissolved in distilled water at half the concentration used for solid nutrient agar plates. The solution was transferred to an Erlenmeyer flask, the mouth of which was covered with aluminum foil. The flask was sterilized in an autoclave at 121 ℃ for 20 minutes. After sterilization, the medium was allowed to cool to 50 ℃ before use.

SM Buffer: Gelatin (0.1 g), $MgSO_4 \cdot 7H_2O$ (2 g), and NaCl (5.8 g) were weighed. These components were added to 50 mL of 1 M Tris-HCl (pH 7.5) and dissolved. The solution was brought to a final volume of 1 L with deionized water, sterilized at 121 ℃ for 20 minutes, and stored at 4 ℃ until use.

PBS Buffer: KCl (0.2 g), NaCl (8.0 g), KH_2PO_4 (0.2 g), and $Na_2HPO_4 \cdot 12H_2O$ (3.6 g) were weighed and dissolved in 950 mL of Milli-Q ultrapure water. The pH was adjusted to 7.2-7.4 using 6 M HCl. The solution was brought to a final volume of 1 L with Milli-Q water, sterilized at 121 ℃ for 20 minutes, and stored at room temperature until use.

Saline solution: Sodium chloride (NaCl, 3.6 g) was dissolved in 400 mL of ultrapure water within a glass vessel. The solution was subjected to moist-heat sterilization via autoclaving (121 ℃, 15 psi saturated steam) for 20 minutes. Prepared saline aliquots were stored at ambient temperature until required for experimental procedures.

4.2.2 Phage propagation via liquid lysate

The bacterial host was cultured in LB with overnight incubation at 37 ℃ under 200

rpm agitation. For primary amplification, 50μL of this culture was inoculated into 10 mL fresh LB broth and supplemented with 50 μL high-titer phage lysate (>10^8 PFU/mL) during mid-logarithmic growth. Following incubation at 37 ℃ with vigorous shaking (250 rpm) until complete lysis occurred (typically 12-18 h), a secondary amplification was performed by adding 50 μL fresh overnight host culture and incubating for an additional 12 h. The resultant clarified lysate was decanted and stored at 4℃ prior to purification.

4.2.3 Phage purification and sterilization

Lysates underwent centrifugation at 12,000g for 10 min at 4 ℃ to pellet cellular debris, whereupon supernatants were aseptically transferred using serological pipettes. A trace volume of chloroform (0.5% v/v) was added to the supernatant with brief vortex mixing, followed by phase separation centrifugation at 12,000g for 4 min. The aqueous phase was carefully recovered and filtered through 0.22 μm PVDF membranes under sterile conditions to generate bacterial cell-free lysates. Purified phage preparations were stored at 4 ℃ and titers quantified via double-layer plaque assay before experimental use.

4.2.4 Bacterial culture activation

Cryopreserved bacterial stocks were revived under aseptic conditions. Sample was retrieved using sterile pipette tips and transferred into a conical tube containing fresh sterile liquid medium. The inoculated tube was incubated overnight (12-16 h) in a temperature-controlled orbital shaker maintained at 37 ℃ with continuous agitation at 200 rpm until turbid growth was observed. Subsequently, a sterile inoculation loop was used to streak the broth culture onto solid agar plates. Plates were incubated inverted at

37 ℃ for 18-24 h to obtain isolated colonies. A morphologically representative single colony was then aseptically picked using a pipette tip and inoculated into fresh sterile liquid medium for expansion culture. Following a second overnight incubation at 37 ℃ with shaking (200 rpm), this subculturing procedure was repeated 1-2 times to achieve strains without infection for subsequent antimicrobial assays. All culture media were pre-warmed to 37 ℃ prior to inoculation.

4.2.5 Bacteriophage titer determination

The bacteriophage titer was determined using the double agar overlay method (spot testing). 50μLof 10^8 CFU/ml *P. aeruginosa* logarithmic-phase culture were mixed with 5ml melted (about 60ºC) semi LB agar medium then were added to a prepared Petri dish containing a bottom layer of LB agar medium. The plate was gently rocked to ensure uniform distribution of the bacterial - semi agar surface. Then the plate was left undisturbed in the laminar flow hood for 10 minutes to allow adsorption. Meanwhile the bacteriophage sample was serially diluted (10-fold dilutions). Ten microliters (10 μL) of each diluted phage sample were spotted onto the prepared agar surface. The plate was again left undisturbed in the laminar flow hood for 30 minutes to allow complete absorption of the phage dilution into the agar. The plate was inverted and incubated at 37 ℃ for 12 hours. Plaques were counted following incubation. Each sample was assayed in triplicate.

The bacteriophage titer (expressed as Plaque-Forming Units per milliliter, PFU/mL) was calculated using the following formula:

Phage titer (PFU/mL) = Plaque count × Dilution factor × 100

4.2.6 Zone of inhibition assay

The antimicrobial efficacy of solid materials was evaluated using the agar diffusion method, wherein inhibitory compounds diffuse through the solid medium to form a concentric zone of bacterial growth inhibition surrounding the test specimen. Bacterial suspensions were applied from 1×10^6 CFU/mL to 1×10^8 CFU/mL, and 50 μL of bacterial suspension were mixed with 5ml melted (about 60°C) semi-LB agar medium then were added to a prepared Petri dish containing a bottom layer of LB agar medium. The plate was gently rocked to ensure uniform distribution of the bacterial - semi agar surface, after which functionalized scaffolds were firmly applied onto the top agar surface. Plates were sealed, inverted, and incubated at 37 °C for 24 h in a constant-temperature incubator. Following incubation, digital images of inhibition zones were captured using a gel documentation system under white transillumination. The diameter of each clear inhibition zone (including material diameter) was measured in triplicate using digital calipers, with mean values reported as quantitative indicators of antimicrobial activity.

4.3 Cryoelectron microscopy

4.3.1 Cryo-EM specimen preparation

Specimen preparation was performed at the Chinese University of Hong Kong (Shenzhen). Quantifoil grids were rendered hydrophilic using a Tergeo Plasma Cleaner (PIE Scientific) for glow discharge treatment. For vitrification, 3 μL of TaPaz phage suspension was applied to the glow-discharged grids, followed by 1-second blotting and rapid plunging into liquid ethane using an automated vitrification system (Vitrobot Mark IV, Thermo Fisher Scientific). The frozen grids were then immediately transferred from

liquid ethane to liquid nitrogen using precooled forceps. The self-locking mechanism of the forceps was released, and the grid was carefully mounted onto a cryo-EM specimen holder. All steps were conducted under liquid nitrogen cooling to prevent ice crystal formation due to temperature fluctuations. Prepared samples were stored in a liquid nitrogen Dewar at −180 ℃ until further use.

4.3.2 Cryo-EM data collection

Cryo-EM data collection was performed at the Chinese University of Hong Kong (Shenzhen) using SerialEM software on a Titan Krios TEM (Thermo Fisher Scientific) operating at 300 kV. Initial grid screening involved acquiring a full montage to identify squares with optimal ice conditions characterized by appropriate thickness, minimal contamination, and structural integrity. Selected areas were then imaged at low dose to locate suitable holes exhibiting homogeneous particle distribution and clean ice for high-resolution data collection. Micrographs were recorded using a Gatan K3 direct electron detector in counting mode at 1.06 Å/pixel magnification with a total dose of 17.5 e/Å^2 delivered over 2.5 seconds. The system was configured with a spherical aberration (Cs) value of 2.7 mm, and each exposure was fractionated into 50 frames, yielding a final dataset of 1,486 micrographs for subsequent processing.

4.3.3 Image processing with RELION

The cryo-EM data processing was carried out using RELION software for single particle analysis and high-resolution structure determination. Following data acquisition, the raw movies were imported into the processing pipeline where motion correction was initially performed using RELION's integrated MOTIONCOR2 algorithm to align all 50

frames from each exposure. This correction step compensated for sample drift and beam-induced movements during acquisition, generating stabilized micrographs with improved contrast by combining the aligned frames. The motion-corrected images were then subjected to contrast transfer function (CTF) estimation using CTFFIND-4.1, which efficiently calculated defocus values by analyzing the movie-averaged power spectra through RELION's implementation. The quality of CTF estimation was visually verified by examining Thon ring patterns, ensuring proper alignment between experimental and theoretical zeros. Micrographs displaying substantial ice contamination or poor CTF fitting were manually excluded from subsequent processing steps, while the remaining high-quality images were retained for further structural analysis.

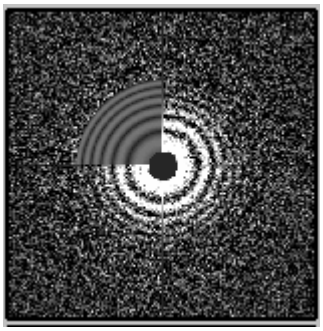

Figure 6 Thon rings of cryo-electron microscopy images.

The upper left corner in Fig. 6 is the Thon ring of the computer simulated cryo-electron microscope image, and the remaining part is the Thon ring obtained by Fourier transform of cryo-electron microscope image. The image is obtained from RELION during our structural reconstruction.

4.3.4 Asymmetric portal complex reconstruction

Due to the replacement of one icosahedral fivefold vertex by the portal complex, phage capsids exhibit noncanonical pseudo-icosahedral symmetry. Initial icosahedral

symmetry imposition during conventional reconstruction averaged out portal density. To resolve the portal structure, a symmetry-mismatch reconstruction strategy was implemented in RELION-3.1: Single-particle analysis of capsids was performed at binning (2.24 Å/pixel) under I3 symmetry (fivefold axis aligned with Z-axis), yielding a reconstruction model with associated particle.star metadata. Icosahedral symmetry expansion via relion_particle_symmetry_expand generated asymmetric particles (60 orientations/original particle), with fivefold vertices centered at (x=0, y=0, z=424 pixels) relative to capsid centroid. Fivefold vertex subparticles were extracted using 400-pixel boxes.

Duplicate extractions from symmetry expansion were removed via RELION's Duplicates function. Subparticles underwent 3D classification (8 classes, τ=20, 25 iterations), identifying one class exhibiting portal morphology (10.3% particles, matching 1/12 theoretical distribution).

Final portal structure was resolved through local refinement with C5 symmetry and CTF refinement.

The head 3D reconstruction models are from previous work. The particles were taken from the best Refine3d and 3d classification was launched with Perform Image Alignment set to No. Only the best-looking class was selected after 3d classification. Selected particles were re-extracted using the "extract refined particles" option within the extraction job. Subsequently, the particles were rescaled to a size of 200 pixels. Symmetry expansion was performed on the extracted particles with respect to the I3 symmetry group. A 200-pixel 3D model, intended for use as a reference volume, was generated utilizing the relion_image_handler command. The Chimera software was employed to draw a

mask that covers one of the icosahedron vertices of the reference volume. This mask was then resampled onto the initial map to ensure it possesses the same volume dimensions. Enhancement of the mask from the resampled volume was carried out through the Relion MaskCreate job. A Class3d analysis was performed without conducting orientation searches (Fig. 7). For this classification, the expanded particles .star file served as the input, along with the rescaled reference volume and the mask covering the penton. The C5 symmetry was applied in this classification process.

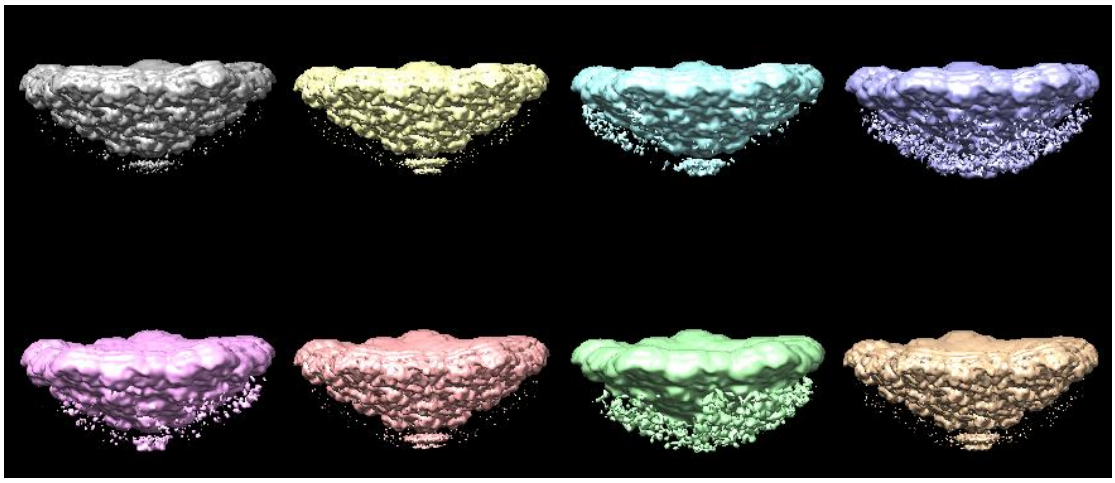

Figure 7 Result of 3d classification, which after capsid symmetry expansion, the portal part is solved in these classifications. The image is obtained from RELION during our structural reconstruction.

From the obtained results, aiming to enhance the signal-to-noise ratio of the map regions with low signal-to-noise ratio, a cylindrical mask was created. Specifically, a cylinder shape was drawn using Chimera and positioned over the tail density region. The newly created volume was resampled, expanded via the MaskCreate function, and the classification was repeated with C5 symmetry. Additionally, classification under C1 symmetry (instead of C5 symmetry) was performed, and the results of these two classifications were compared (Fig. 8).

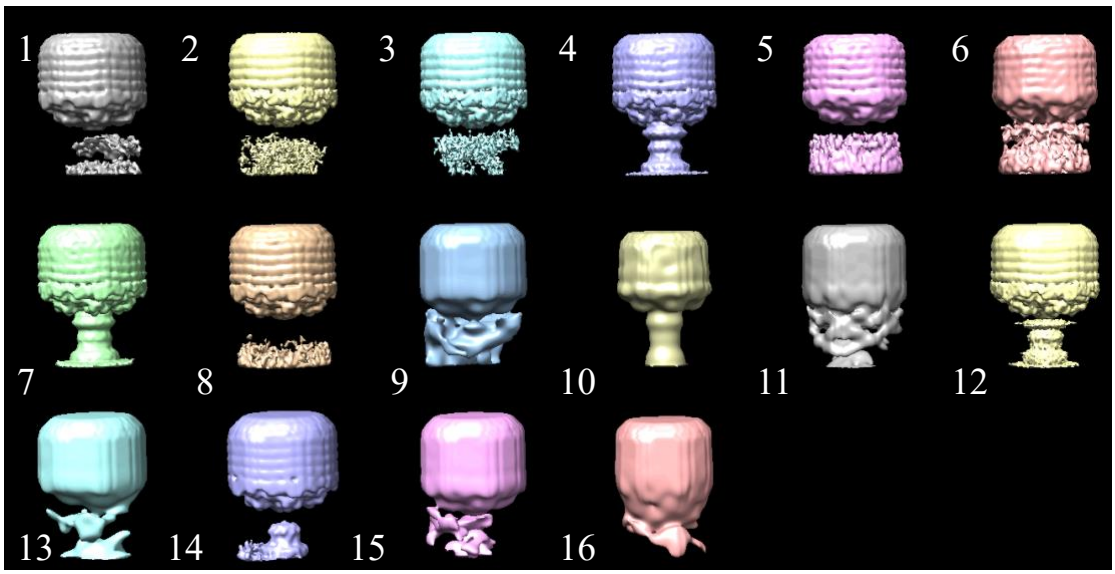

Figure 8 Result of 3d classification: 1-8 classes with C5 symmetry and 9-16 classes with C1 symmetry. The image is obtained from RELION during our structural reconstruction.

Furthermore, the number of particles in the classes exhibiting tail density was examined. It is expected that this number accounts for approximately 1/12 of the total number of particles. According to the classification under C5 symmetry, the proportion of tail classes is 0.103, which is slightly higher than 1/12. In contrast, the proportion of tail classes in the classification under C1 symmetry is 0.78, which is significantly higher than 1/12. This indicates that the tailed classes contain a mixture of tail vertices and empty vertices.

Ultimately, the output from the C5 classification was selected. Only the tailed classes were chosen, and after removing duplicates, 5189 particles remained. Following the re-extraction of these particles with a size of 400 pixels, a reference model was prepared by reconstructing the volume using the relion_reconstruct command.

Particles were extracted from the previous refinement and binned to a size of 200 pixels. These particles were refined against the model containing the tail, utilizing a

cylindrical mask that covers the tail region. Local searches were conducted with C5 symmetry. Additionally, 3D classification with C5 symmetry was performed using the cylindrical mask, aiming to exclude particles without the tail (Fig. 9).

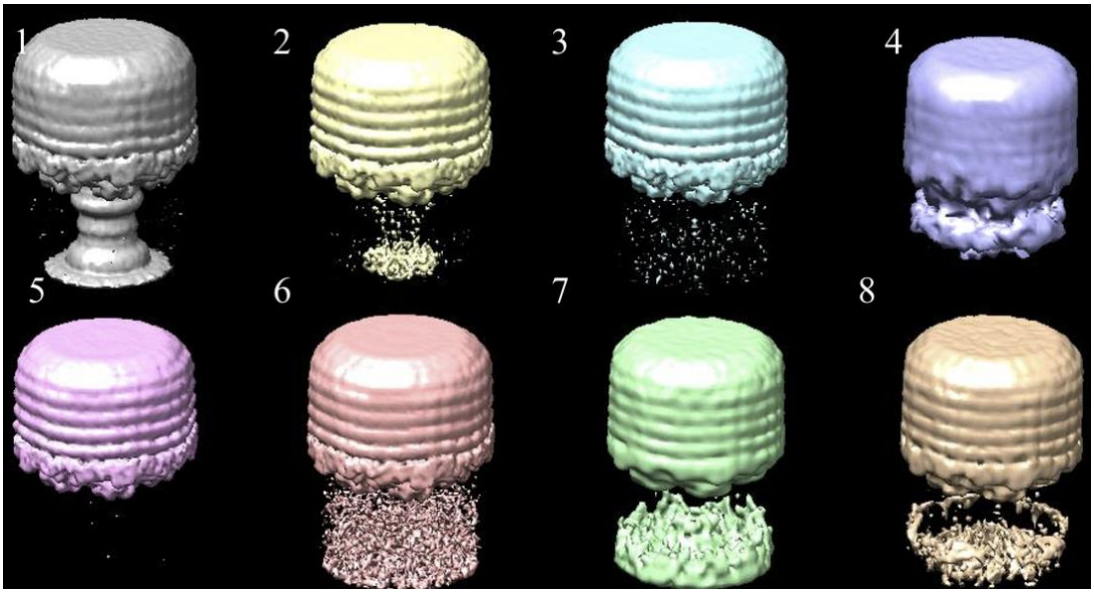

Figure 9 Result of 3d classification, only the class 1 was chosen. The image is obtained from RELION during our structural reconstruction.

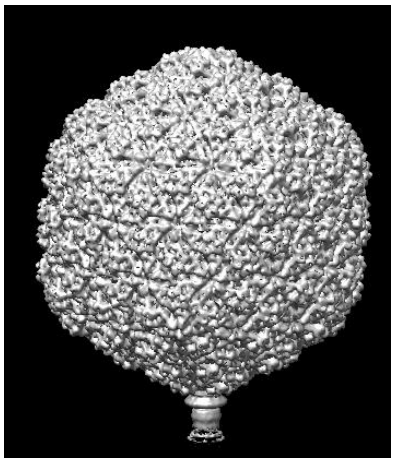

Figure 10 Result of binned 400pix refinement model. The data is obtained from RELION during our structural reconstruction and visualized in Chimera.

Particles from tail-containing classes were refined to obtain the binned C5 model (Fig. 10).

Chimera was used to determine the appropriate center for the new box, which was

designed to encompass the portal protein, the head-tail interface, and the tail density. Ultimately, a box size of 450×450×450 was selected. The refined particles were re-extracted using this new box, with the "Re-center on X, Y, Z" option enabled (coordinates: (0,0,75)), and were also binned to 200 pixels. A model was constructed without re-aligning the particles via the relion_reconstruct command (Fig. 11). Subsequently, refinement with full angular search was performed under C6 symmetry, using a cylindrical mask that covers the interface region.

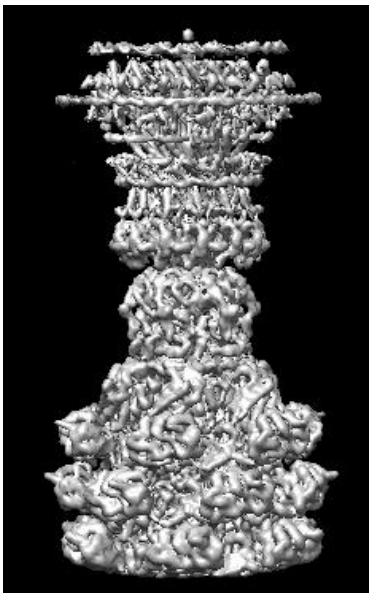

Figure 11 Result of interface refinement and the resolution is 4.82 Å. The data is obtained from RELION during our structural reconstruction and visualized in Chimera.

A mask was created from the density using Chimera, followed by extension of the mask within Relion (Fig. 12).

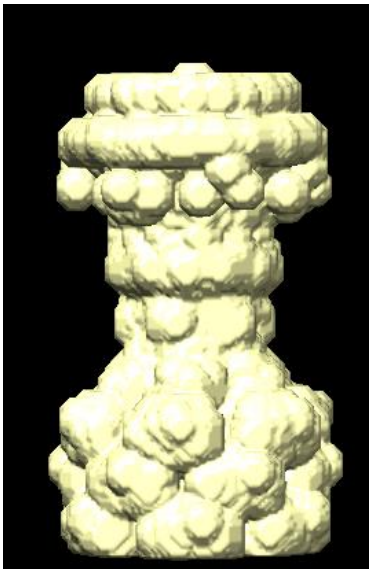

Figure 12 Image of the mask which was created by Chimera. The data is obtained from RELION during our structural reconstruction and visualized in Chimera.

Then, C6 classification was performed without particle alignment to exclude unsatisfied particles.Finally, 8044 particles were selected from the initial 8397 particles. The unbinned particles were re-extracted, and masked in Chinera. Refine3D was performed with local searches function only. In this way, the refinement was calculated at a resolution of 3.45 Å.

4.3.5 AlphaFold model

The AlphaFold system was developed by DeepMind for protein structure prediction. It employs advanced internal validation metrics for evaluate prediction reliability. These confidence measurements play a crucial role for interpretation and experimental design. The key point, Per-Residue Confidence Score (pLDDT), provides a quantitative assessment ranging from 0-100. It can represent the model's certainty in local backbone atom positioning accuracy for each amino acid. The pLDDT values are conventionally categorized into distinct reliability tiers: predictions scoring above 90

demonstrate exceptional confidence with approximately 1Å backbone deviation, while scores between 70-90 indicate reliable structural elements. Regions scoring 50-70 require cautious interpretation due to potential inaccuracies, and scores below 50 typically correspond to intrinsically disordered segments or regions lacking well-defined electron density in experimental structures. These confidence levels are frequently represented through color-coded visualization in molecular viewers, with a spectrum from blue (high confidence) to red (low confidence) mapped onto the protein structure [101].

4.3.6 Atomic model refinement

The head-rail interface atomic model was initially constructed through homology modeling in Alphafold, and the model with the higher pLDDT score were saved as PDB format. This initial model was rigid-body fitted into the cryo-EM density map (3.18Å resolution) within UCSF Chimera1.16, followed by conversion of the density map from MRC to MTZ format using CCP4 utilities.

For head-tail adaptor protein model building, we used DeepTracer [102] and receive the output result that the initial model was automatically docked into the density map. For all the four proteins, we corrected and adjusted them manually by real-space refinement function in WinCoot [103]. After several rounds of real-space refinement, the problematic geometry, Ramachandran outliers and poor rotamers were manually corrected as they were eliminated or moved to favored regions in WinCoot. The refinement density map was performed Map_symmetry in PHENIX [104] to obtain the the file with NCS information. The atomic models were applied NCS operators with Apply_NCS_operators function in PHENIX. For portal protein and gp54, we prepared 2

copies in Chimera as the input files and for collar protein and head-tail adaptor protein, 1 copy for each was prepared for input. The full structures with symmetry were generated for each protein and then were performed Combine_PDB_files for receiving the completed head-tail interface atomic model in PHENIX. The whole resulting model was then refined with Real_space_refine with using secondary structure restraints and Ncs constraints in PHENIX. The validation was checked again through the result of phenix.real_space_refine and the problematic clashes, CaBLAM outliers, Ramachandran outliers and poor rotamers were manually adjusted again to make the model more accurate.

4.4 Scaffold preparation

4.4.1 Regeneration of silk fibroin (SF)

The silk fibroin (SF) solution was regenerated using an adapted literature method [105]. The processing protocol involved dissolving 6 g of SF in a ternary solvent system containing calcium chloride, water, and ethanol (molar ratio 1:8:2) with constant heating at 85 ℃ for 6 hours in a water bath. Following complete dissolution, the SF solution was allowed to gradually cool to ambient temperature before undergoing extensive purification through dialysis against ultrapure water over 72 hours. The dialyzed solution was subsequently clarified by centrifugation and adjusted to a working concentration of 20 mg/mL through controlled dilution with ultrapure water for subsequent scaffold preparation.

4.4.2 Silk-based scaffold

The silk fibroin (SF) composite scaffolds were fabricated by homogeneously

blending the 20 mg/mL stock solution with 1% dimethyl sulfoxide (DMSO). This mixture was uniformly distributed across 48-well culture plates and subjected to controlled cryogenic treatment at -80 ℃ for 120 hours to facilitate scaffold formation. Following this freezing protocol, the SF composites had a sequential thawing process in pure ethanol. Then they were multiple rinsed with distilled water to ensure complete removal of residual solvent and ethanol.

4.4.3 Silk-based scaffold with gelatin (SFG)

SFG scaffolds were prepared by homogenizing the stock solution (20 mg/mL) with 20 mg/mL gelatin solution at a 7:3 volumetric ratio. This mixture was supplemented with 1% (v/v) DMSO, uniformly dispensed into 48-well plates, and frozen at -30 ℃ for 7 days. Prior to use, composites underwent progressive thawing through ethanol immersion followed by distilled water rinsing to eliminate residual solvent.

4.4.4 Silk-gelatin-chitosan (SFGC) scaffold preparation

Chitosan solutions (3% w/v) were prepared by dissolving chitosan in 0.1 M acetic acid under continuous stirring at room temperature until complete dissolution. The SFGC composites were fabricated by homogenizing silk fibroin stock solution (20 mg/mL) with 20 mg/mL gelatin solution and chitosan solution at volumetric ratios of 7:3:1, 7:3:3, and 7:3:5 respectively. Following supplementation with 1% (v/v) DMSO, the mixtures were dispensed into 48-well plates, cryopreserved at -30 ℃ for 7 days, and processed through ethanol-mediated thawing with distilled water rinsing using identical protocols to the SFG scaffold preparation.

4.4.5 Silk-based scaffold with Polyethyleneimine (PEI)

The silk fibroin (SF) scaffolds were chemically crosslinked with polyethyleneimine (PEI) according to an established method with slight adaptations [106]. In this process, the SF composites were immersed in an aqueous PEI solution (5% by weight) and the pH was carefully titrated to neutral (pH 7.0) using 0.1 M hydrochloric acid. To enhance the polymerization kinetics, sodium cyanoborohydride (0.21 wt%) was subsequently introduced as a reducing agent, and the reaction system was subjected to ultrasonic treatment for 60 minutes to ensure homogeneous crosslinking.

4.4.6 Phage functionalization of scaffolds

Prefabricated scaffolds were immersed in phage lysates of graded titers (10^6-10^9 PFU/mL) in room temperature for 2 hrs to promote phages attach scaffolds then keep them in 4°C overnight. Following functionalization, scaffolds were subjected to three sequential gentle washes with either physiological saline (0.9% NaCl) or phosphate-buffered saline (pH 7.4) to remove loosely adsorbed phage particles while preserving surface-bound virions. Processed scaffolds were maintained in sterile humidified chambers at 4°C until subsequent antimicrobial assessments.

4.4.7. In Vitro swelling rate and water solubility determination of the scaffolds

The swelling behavior was evaluated following an adapted protocol based on Jin et al. [107]. Specimens were precisely sectioned into 10 mm diameter segments and immersed in PBS (pH 7.4) maintained at physiological temperature (37°C). The swelling kinetics were monitored over a 14-day period, with measurements taken at multiple timepoints ranging from initial immersion (t=0) to complete saturation.

At predetermined intervals, samples were carefully removed from the PBS solution, gently blotted with Kimwipes to remove excess surface liquid, and immediately weighed (Ws) to determine fluid uptake. Dimensional changes were quantified through precise measurements of both axial and radial diameters. The swelling equilibrium was considered achieved when consecutive measurements showed no significant mass variation. The swelling ratio was subsequently calculated using Equation (1):

$$E_{SR}/\% = \frac{m_t - m_0}{m_0} \times 100 \quad \text{Equation (1)}$$

Formula: E_{SR}, scaffold swelling rate, %; m_o, initial mass of scaffold, m_g; m_t, mass after swelling of the scaffold, mg.

4.4.8 Phage diffusion rate assessment

Following scaffold fabrication, each specimen was rinsed three times with sterile distilled water to remove unabsorbed phage. The washed scaffold was then immersed in 1 mL of sterile 0.1 M PBS (pH 7.4) and incubated at 37℃ in a humidified environment for 24 hours. Subsequently, the PBS buffer was collected and subjected to phage titration to quantify eluted bacteriophages. The same scaffold underwent repeated washing with sterile distilled water and was transferred to fresh sterile PBS daily. This elution-titration cycle was performed consecutively for 7 days to monitor sustained phage release kinetics.

4.4.9 Antibacterial function of scaffold in liquid medium

Experiment for *P. aeruginosa:* 4.5ml LB liquid was mixed with 30ul 10^9 CFU/mL bacteria suspension into a tube, then well-prepared phage scaffolds were added. After 280rpm, 37℃ overnight culture, observe the bacteria growth degree (according to transparency or OD590) each day. If necessary, check titer of remain bacteria in the tube

every day. Routine experiment lasts 5 days.

4.4.10 Antibacterial function of scaffold in semi-solid agar

5 ml 0.75% Agar-LB medium was added into tube when it was melted. 10ul 109 CFU/mL bacteria suspension was injected into semi-solid agar. Phage-scaffold was put nearby the injected bacteria. After 3-5 days incubation at 37 ℃, part of 3D clear zone can be observed around scaffold.

4.5 Transmission electron microscopy and electron tomography

Scaffolds were cut into small pieces (1x1 mm). The samples were fixed in 2% glutaraldehyde for 5 hours then washed with 0.1M Cacodylate buffer. After post-fix samples in 1% OsO4 in 0.1M cacodylate buffer, samples were dehydrated with a graded series of ethanol(50％,60％,70％ in 4℃, 80％ and 96％ in room temperature). Then samples were further dehydrated with acetone for 45min, this step was repeated 3 times at room temperature. Then samples are transferred into series of Epon (Embed 812 + DDSA (Dodecenylsuccinic anhydride) + MNA (Methylnadic anhydride) in 13:8:7 proportions) - acetone mixture (1:3, 1:1, 3:1) for 1 hour each. DMP-30 (Tris (dimethylaminomethyl) phenol) was added in Epon for polymerization. Before final embedding cells are placed in Epon for overnight incubation. Samples were polymerized at 37 ℃ for 24 hours and at 60 ℃ for 48 hours. Ultrathin sections were cut with a diamond knife on an ultramicrotome, transferred to copper grids, covered with formvar and contrasted with lead citrate, according to the Reynolds established procedure (Reynolds, 1963). The images are collected by transmission electron microscope JEOL JEM-2100

200 keV electron microscope equipped with a LaB6 electron source.

Electron tomography data were collected with SerialEM software with ±60° range and 1° step.

4.6 Scanning electron microscopy

For scaffolds structural analysis, the prepared samples underwent frozen at -80℃ for 10 minutes followed by complete dehydration via lyophilization (LABCONCO FreeZone 4.5L, USA) over 24 hours. Prior to imaging, specimens were mounted on aluminum stubs using conductive carbon tape and coated with a gold-palladium layer through argon plasma sputtering (KYKY SBC-12, China) under vacuum conditions. Structural visualization was performed using scanning electron microscopy (KYKY SEM6200, China) at varying magnifications ranging from 100× to 2,000×.

The biofilms formed by overnight bacterial cultures were collected using 5 mm × 5 mm aluminum foil strips. Biofilms were treated separately with two distinct phage lysates at a multiplicity of infection (MOI) of 0.1-0.01 and incubated for different time at 37℃. Following phage treatment, foil strips were fixed in 2.5% v/v glutaraldehyde for 40 min at room temperature then dehydrated through an ethanol gradient (30%, 50%, 70%, 90%, 100% v/v) and subjected to critical point drying (Hitachi HCP-2, Japan). Dried samples were sputter-coated with a gold layer using an ion coater.

Biofilm samples were imaged using scanning electron microscopes (JSM-6380LV, JEOL, Japan and KYKYSEM6200, China). Micrographs were acquired at magnifications ranging from 500× to 10,000×.

4.7 Crystal violet staining

Bacterial biofilms were cultured in 48-well plates. Overnight bacterial cultures (10 μL) were inoculated into 1 mL of fresh LB medium per well and incubated overnight. After incubation, the medium was carefully aspirated using syringe to minimize disruption of the biofilm. The biofilm was then washed twice with 1× phosphate-buffered saline (PBS) to remove planktonic cells. Then biofilms were treated with different phage lysates and incubated for 24 h. Following treatment, the reaction mixture was aspirated, and the biofilms were washed again with PBS.

The samples were stained with 1% (w/v) crystal violet solution for 15 min at room temperature. Unbound dye was removed by extensively washing the wells with PBS buffer (≥3 washes). Plates were air-dried overnight before imaging.

4.8 Fluorescent microscopy

Membrane Permeability Assessment: Bacterial membrane integrity was evaluated using propidium iodide (PI) and DAPI as fluorescent indicators. Following overnight culture, biofilms were collected by cell glass and then treated with phages overnight. Subsequently, samples were washed three times with sterile PBS (pH 7.4) to remove residual cells. Washed samples were stained in 1.5 mM staining solution and incubated in a light-protected environment at ambient temperature for 20 min to permit nucleic acid intercalation in membrane-compromised cells. Excess dye was removed through three additional PBS wash cycles to minimize background fluorescence. Finally, samples were mounted on glass slides, and immediately imaged using confocal microscopy with 340

nm, 488 nm, excitation detection parameters.

4.9 Raman spectrometry

Raman spectroscopic characterization was performed using a Renishaw InVia confocal Raman microscope system (Wotton-under-Edge, UK) featuring a Leica DM2700M optical microscope. The system was configured with a near-infrared excitation laser (780 nm wavelength, 50 mW power) and a high-resolution diffraction grating (1200 lines/mm). For each measurement location, multiple spectra (minimum of 3 replicates) were collected in static acquisition mode across the spectral range of 700-1800 cm^{-1} to ensure data reproducibility.

Post-acquisition spectral processing involved sequential data treatment: baseline correction was initially performed using WiRE 5.2 software, followed by spectral averaging in SpectraGryph 1.2. Final data visualization and graphical representation were accomplished using Origin 2021 software for scientific graphing and analysis.

4.10 Data analysis

Graphs and statistical data analysis was performed in GraphPad Prism. The diameters and width of cells was measured in Image J and Nanomeasurer1.2, and data analyzed in GraphPad Prism One-way ANOVA test, at 95% confidence interval. Measurements of pore size distribution and porosity of the scaffolds and the average area covered with the cells was performed using the the ImageJ software [108].

5. Results

5.1 Cryo-EM reconstruction: head-tail interface of phage Tapaz

The portal protein complex represents an essential structural and functional component of bacteriophages that mediates viral genome delivery during host cell infection. These specialized molecular assemblies form dodecameric ring structures that are precisely integrated at a single five-fold vertex of the icosahedral capsid. They are involved in crucial aspects of viral replication, such as virion assembly, DNA packaging and DNA delivery [41]. In this regard, the structural biology study of the portal proteins complex is helpful to study the interaction between phage and host, which is of great significance to the study of phage therapy.

Following CTF refinement and polishing (using default parameters), subsequent refinement of head-tail interface resulted in a final resolution of 3.18 Å (Fig. 13).

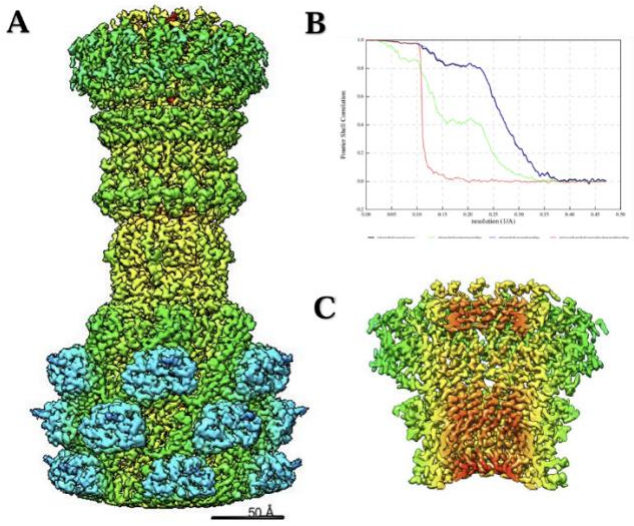

Figure 13 (A) Cryo-EM reconstruction of the TaPaz phage head-tail interface. Bar=50Å; (B) FSC curve indicates 3.18 Å resolution. Green – unmasked half-maps, blue – masked half-maps, red – phase randomized masked half-maps, black – corrected. (C) Inside view of portal protein part. (Wang et al, 2022)

The protein sequences of all parts of the structural part were uploaded into AlphaFold, and several predictions of the protein structure were generated.

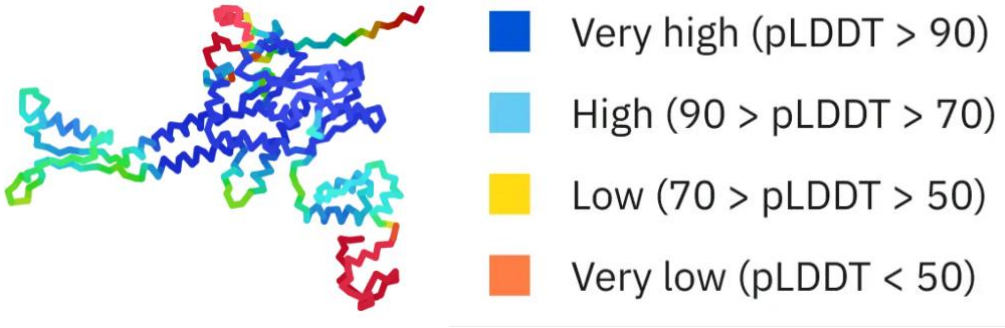

Figure 14 Prediction structure of portal protein from Alphafold. Colored according to the model confidence (legend on right).

The most confident structure was selected (Fig. 14), which was then fitted into the map using Chimera (Fig. 15). These confidence levels are frequently represented through color-coded visualization in molecular viewers, with a spectrum from blue (high confidence) to red (low confidence) mapped onto the protein structure. Subsequently, C12 symmetry copies were generated for this structure.

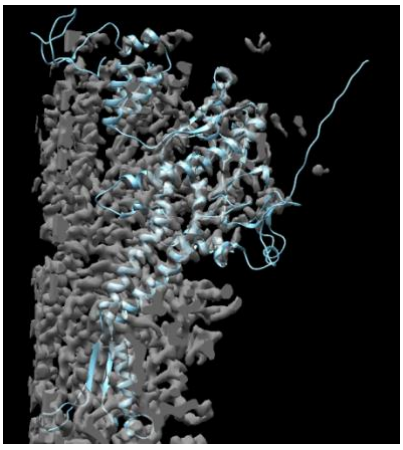

Figure 15 Fit the atomic structure in the map before obtaining C12 copies

After atomic model refinement in Coot and Phenix, the atomic model of head-tail interface structure was solved (Fig. 16), which included portal protein, head-tail adapter, head completion, tail terminator protein, tube protein and sheath protein (Fig. 16, 17).

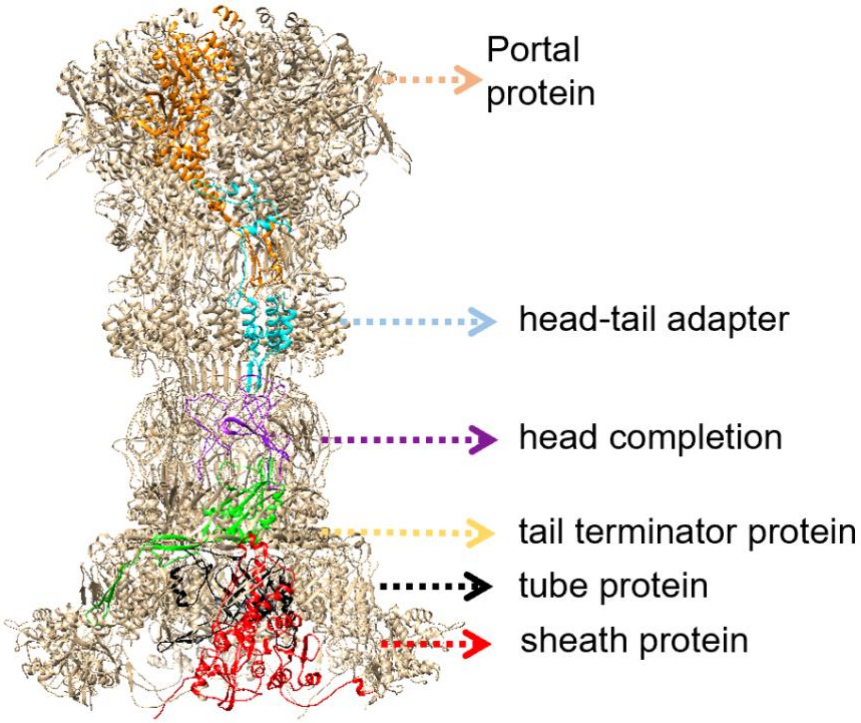

Figure 16 Atomic model of head-tail interface structure

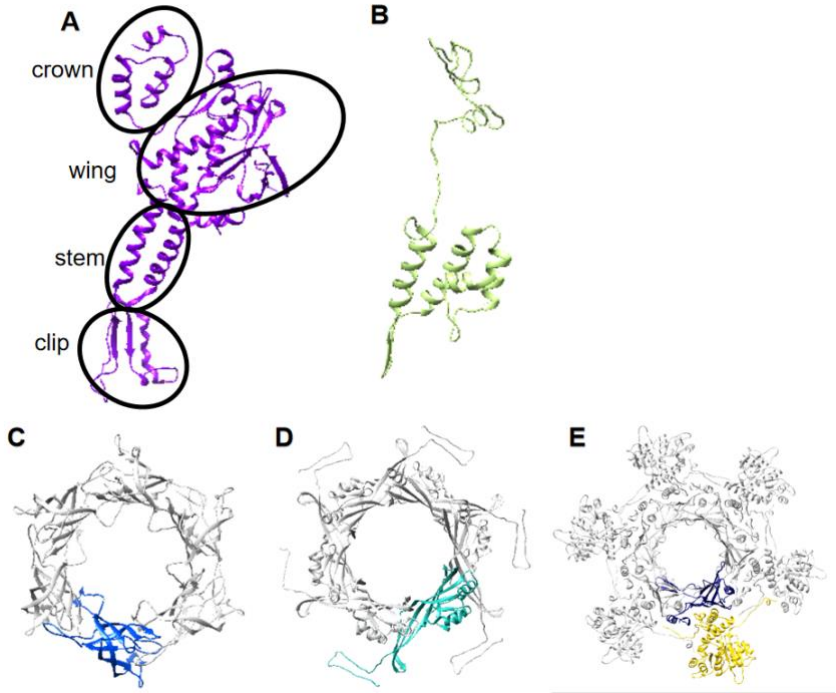

Figure 17 Atomic model of (A) Side view of a single subunit of portal protein; (B) Side view of a single subunit of head-tail adapter; (C) Top view of head completion; (D) Top view of tail terminator hexamer; (E) Top view of tube protein and sheath protein hexamer.

The portal protein is a crucial component for DNA packaging. DNA movements can happen through its central channel [109]. It can interact with the terminase ATPase to provide fuel for pumping DNA against a steep concentration gradient [110]. It is the first part of head-to-tail interface part which under one of 12 vertices of the icosahedral capsid and 12 portal proteins arranged into a ring with C12 symmetry. The structure of portal protein can be divided into 4 parts (Fig. 17). In the upper 2 part, the outward-tilted and untitled helix forms the portal, and the smallest internal diameter and the largest external diameter are 35Å and 150Å, respectively. The lower parts of portal proteins are surrounded by head-tail adapter. On the top, some loops surround the periphery of portal protein to fix the structure, then the untitled helix and sheets form the portal. The head completion hexamer is under the head-tail adapter oligomer with a 28Å diameter pore. The wall of the pore is formed by β-sheets coming from head completion hexamer. The tail terminator protein, which is the connection of head-to-tail interface and the tail tube, also forms a hexamer. The tube proteins are inside the end of tail terminator protein with an internal diameter about 50 Å. The sheath proteins under C6 symmetry which assemble around the tube in the form of a six-start helix are parts of the contractile molecular machinery.

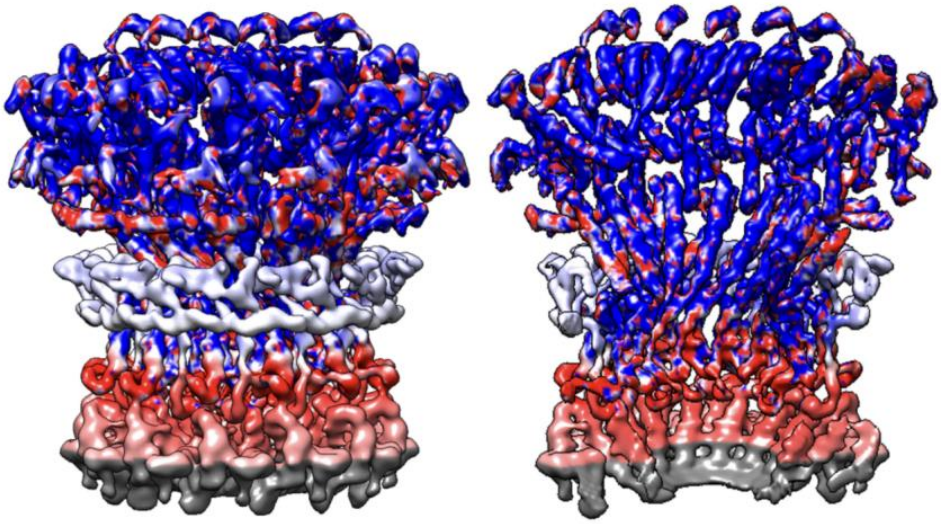

Figure 18 Cryo-EM reconstruction of the TaPaz phage portal interface, different colors stand each protein's electrostatic surface potential, red- -5kT/e, blue- +5kT/e. Left – outer side, right – inner side.

According to results of electrostatic surface potential analysis[1] (Fig. 18), most of the inner part of portal protein has more positive charge to efficiently bind to negatively charged DNA and the outer wing domain shows weak charge/neutral, to avoid binding with non-specific molecules and maintain structural stability. The bottom part has negative charge.

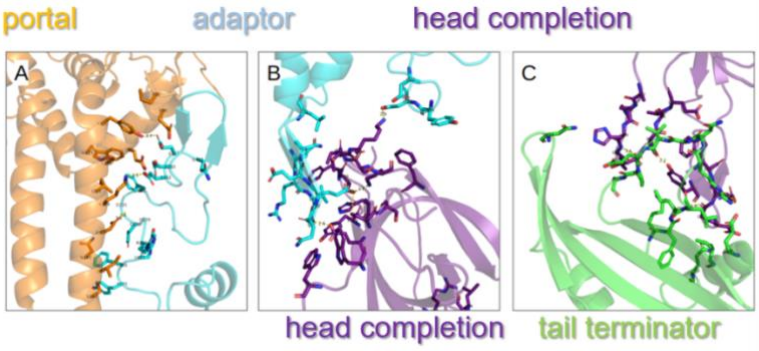

Figure 19 Interactions between (A), portal and adaptor; (B), adaptor and head completion; (C), head completion and tail terminator.

[1] With the help of Dr Marine Bozdaganyan, SMBU

The detailed potential contacts between amino acids across different chains of the proteins are shown in Tables S1-3. The interactions between chains from portal and adaptor exhibit significant number of electrostatic interactions, hydrogen bonds, and salt bridges, for example, GLU152 with LYS234 and GLU153 with TYR226 in Table S1. Chains between adaptor and head completion protein demonstrate strong hydrogen bonds and salt bridges such as those observed between GLU112 and GLN70, SER69 and GLU71 in Table S2. Head completion and tail terminator protein demonstrate the highest number of contacts as shown in Table S3, primarily characterized by hydrophobic forces (Fig. 19). The contacts between the chains were calculated with MAPIYA software [111]. The contact cutoff was set to 5 Å and pH state was set to 7.0.

5.2 Early phage infection vesicles in *P.aeruginosa*

Giant phiKZ-like phages contain a cylindrical inner body and unusually large virions [112]. These phages can construct a proteinaceous shell, the phage nucleus, which compartmentalizes replicating viral DNA, after infection [113]. This structure, assembled from ChmA protein, shields the genome from restriction-modification and CRISPR-Cas nucleases [114]. However, the phage nucleus appears only at mid-infection [113]. The pre-period immediately following genome ejection remained unexplored. Earlier work noted round compartments near phiKZ injection sites [113]. Comparable membrane-bound entities, designated early phage infection vesicles, were later described in related jumbo phages [114]. Those studies confirmed a lipid boundary and proposed protective functions. Despite these advances, the origin, and trafficking behavior of phiKZ Early Phage Infection (EPI) vesicles were not established. Whether the vesicle membrane

derived from host envelopes, which viral components it contained, and how it related to the maturing phage nucleus all remained open questions. This part was therefore undertaken to define the above questions.

From electron tomography, we observed that upon DNA delivery, the phage genome is sequestered within previously unidentified membrane-bound compartments, which we designate as EPI vesicles (Fig. 20, 21).

During the early stages of infection, phage DNA is rapidly ejected from the capsid through the portal complex and translocated into the host cytoplasm. We demonstrate that, within the initial 2–5 minutes post-infection, EPI vesicles are assembled to shield the viral DNA from host bacterial nucleases. These vesicles are enclosed by a membrane approximately 5 nm in thickness—consistent with the dimensions of the host inner membrane—and contain electron-dense internal structures. We postulate that these densities may represent phiKZ-encoded proteins, including phage-specific RNA polymerase. By 30 minutes post-infection, a distinct phage nucleus becomes evident at the center of the infected bacterium (Fig. 20). This compartment not only protects viral DNA from host defense systems but also serves as a dedicated site for viral DNA replication.

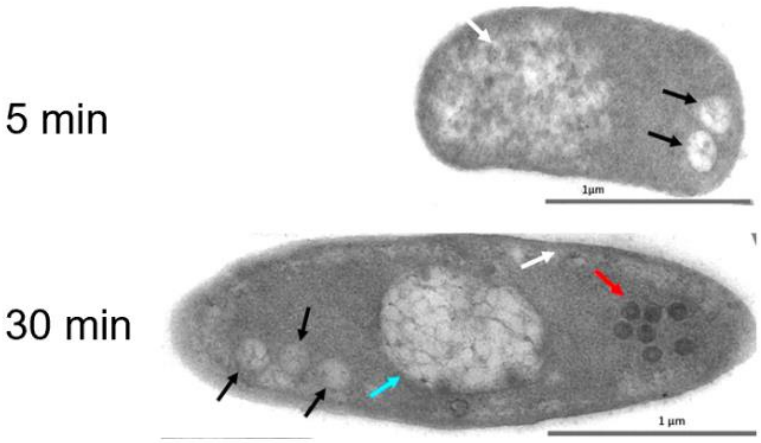

Figure 20 Phage nucleus maturation in *P. aeruginosa*. White arrows - bacterial nucleoid; black arrows - EPI vesicles; blue - phage nucleus; red - new phage capsids [113].

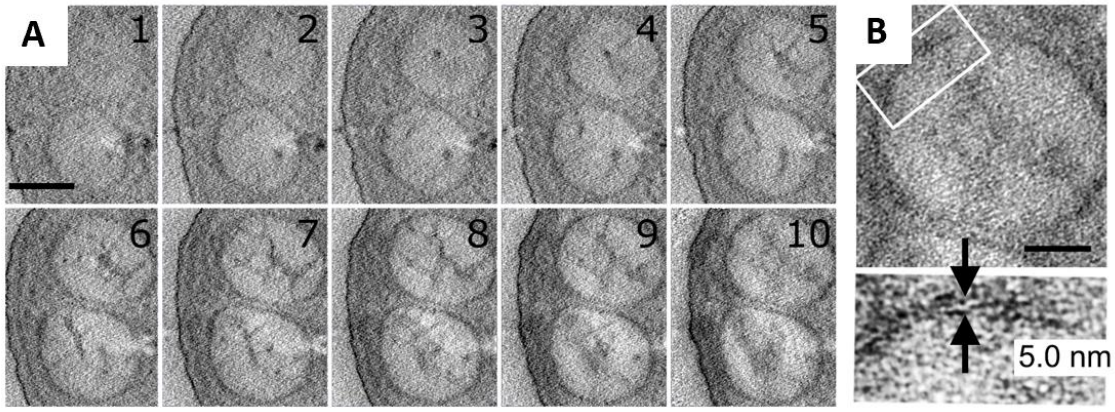

Figure 21 Electron tomography reconstruction of the EPI vesicles in *P.aeruginosa* plastic sections after infection 5 min. (A) A branched electron-dense internal structure. (B) Enlarged image of the membrane forming the EPI vesicle (black arrows) (Antonova…Wang et al, 2024).

Based on these observations, we propose a three-stage model for the early phase of phiKZ infection (Fig. 22):

Stage 1: DNA injection and EPI vesicle formation. Upon infection, the phage injects its genomic DNA along with virion-associated RNA polymerase into the host cytoplasm. Concurrently, invagination of the bacterial inner membrane gives rise to the EPI vesicle. The molecular mechanism governing this membrane remodeling event

remains to be characterized.

Stage 2: Vesicle trafficking and intracellular migration. Following formation, the EPI vesicle migrates directionally toward the cell center. This vesicle functions as a DNA protective place and also the place for early gene transcription by virion-associated RNA polymerase. In the meantime, phage nucleus shell proteins were synthesis.

Stage 3: Phage nucleus assembly and DNA transfer into nucleus. Upon reaching the central cellular locale, the shell proteins assemble into a defined nuclear structure—the phage nucleus. The viral DNA is subsequently transferred from the EPI vesicle into this nuclear compartment, where replication proceeds securely. The vesicle itself remains external to the nascent nucleus following DNA release.

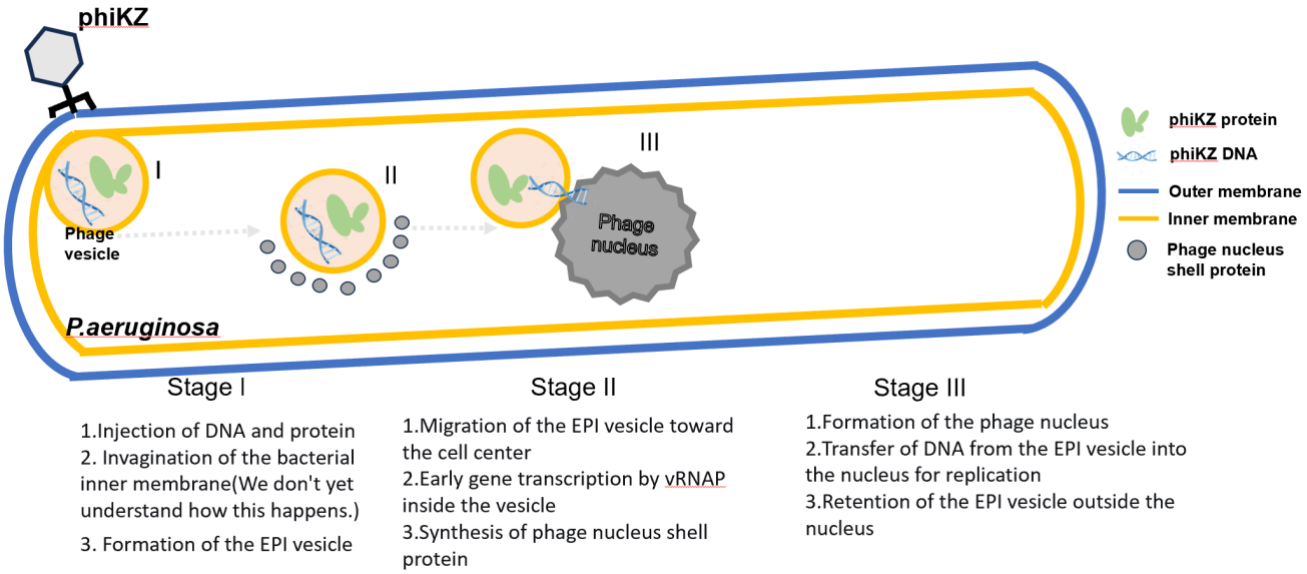

Figure 22 The three-stage hypothetical model of phiKZ bacteriophage early infection (Antonova…Wang et al, 2024).

This work establishes the three-stage model of phiKZ bacteriophage early infection. PhiKZ generates early infection vesicles from the inner bacterial membrane. These structures encapsulate both viral DNA and virion-associated RNA polymerase

immediately after genome injection. EPI vesicles migrate from the cellular pole toward the cell center, then phage DNA exit the vesicle and enter the phage nucleus for replication. These 3 stages reveal an organized strategy with membrane-based protection, genetic materials transport, and phage nuclear assembly during the unprotected early infection.

Several key questions are still unsolved. How viral DNA exits the EPI vesicle without membrane disruption is unknown. The molecular machinery governing vesicle biogenesis, cargo translocation, and membrane fusion has yet to be identified. Future investigations should dissect these mechanisms using genetic and biochemical approaches. Additionally, bacterial defense systems targeting this membrane compartment could also exist. Understanding how phage DNA is safely transported through hostile cytoplasm may inspire novel gene therapy vectors and inform the design of more effective antimicrobial phage therapies.

5.3 Biofilm-phage interactions on *B. subtilis*

B. subtilis, a Gram-positive soil bacterium, has been used as an effective model microorganism for studying the growth cycle that results in biofilm formation wherein motile cells assemble into visible multicellular structures that perform specialized functions. We therefore systematically explore phage interactions with *B. subtilis* biofilms using microscopy techniques. In-depth knowledge of these mechanisms will create new frontiers for broad applications of phages in various fields of microbiology, and biotechnology.

5.3.1 Formation of *B. subtilis* biofilm in different conditions

The experimental evaluation of culture media effects on pellicle biofilm development revealed biofilm formation across all tested media conditions. Scanning electron microscopy analysis of biofilms cultured at 37 °C demonstrated significant morphological variations depending on the growth medium composition. Notably, LB medium promoted the development of dense, robust biofilms characterized by tightly aggregated short bacterial cells forming a compact architecture (Fig. 23a). In contrast, biofilms cultivated in NB and DSM exhibited elongated cellular structures that organized into fibrous, interconnected networks (Fig. 23b). Further examination revealed that DSM-grown biofilms displayed substantially more extracellular matrix deposition compared to their NB counterparts, with the matrix material completely enveloping the cellular components (Fig. 23c). These observations demonstrate that medium composition significantly influences both cellular morphology and extracellular matrix production during pellicle biofilm formation.

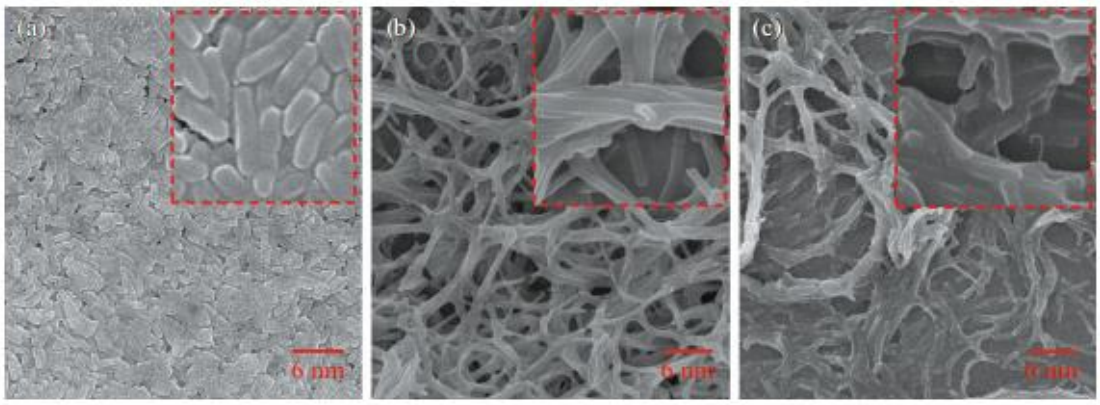

Figure 23 SEM monographs of biofilms after incubation 30h; (a) grown in LB, (b) NB, (c) DSM media at 37°C (inset: 5 K magnification, 6 nm) (Osire, Wang, et al, 2024).

When cultivated at 37°C in LB medium, *B. subtilis* 168 biofilms underwent

significant structural transformations over a five-day period. Initial examination at the air-liquid interface revealed thick biofilm development across all timepoints, with scanning electron microscopy capturing distinct morphological progression. After three days of incubation, biofilms exhibited highly ordered cellular arrangements characterized by tightly packed, uniformly aligned cells (Fig. 24a). These formed flat, homogeneous surfaces resembling woven textile matrices where cell clusters maintained rigorous spatial coherence.

By the fourth day, a clear architectural transition emerged. The initially regimented structures gave way to partial disorganization, with cellular bundles beginning to dissociate. While residual ribbon-like formations persisted, most regions displayed collapsing structural integrity as cells separated from their original configurations (Fig. 24b).

The transformation culminated on the fifth day with complete structural reorganization (Fig. 24c). Biofilms transitioned into randomly distributed, sponge-like fibrous networks where cells maintained proximity but lost all directional alignment. The resulting architecture featured irregular cell distribution across multiple planes, creating undulating surface topographies. This progression from ordered stratification to chaotic volumetric expansion illustrates the inherent dynamism of biofilm maturation under standardized nutrient conditions, suggesting progressive adaptation to microenvironmental constraints at the air-liquid interface.

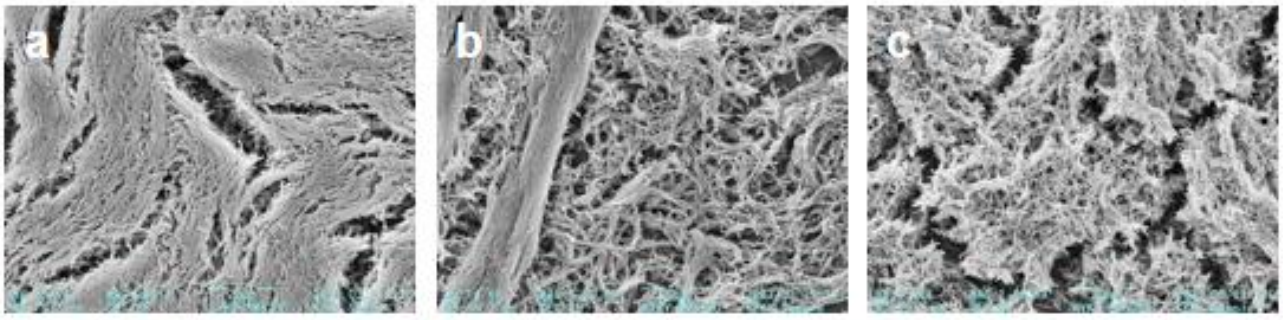

Figure 24 SEM monographs of biofilms grown in LB after incubation (a) 3d; (b) 4d; (c) 5d, Size bar - 20 μm.

5.3.2 Different arrangement of biofilm with AR9 phage treatment

Distinct biofilm architectures—representing compactly ordered versus loosely disordered cellular arrangements—were systematically exposed to bacteriophage lysate and monitored via scanning electron microscopy. In densely packed biofilms, initial structural integrity remained largely unaltered after two hours of treatment, with minimal observable changes to bacterial membranes or surface topography (Fig. 25A, D). By the fourth hour, however, significant fissures emerged within the biofilm matrix, accompanied by morphological distortions in a subset of bacteria (Fig. 25B, E). These early deformations signify the onset of phage-mediated lytic activity. After six hours of exposure, these compact biofilms exhibited pronounced extracellular polymeric substances thickening enveloping bacterial cells, potentially representing a defensive response to phage infiltration (Fig. 25C, F).

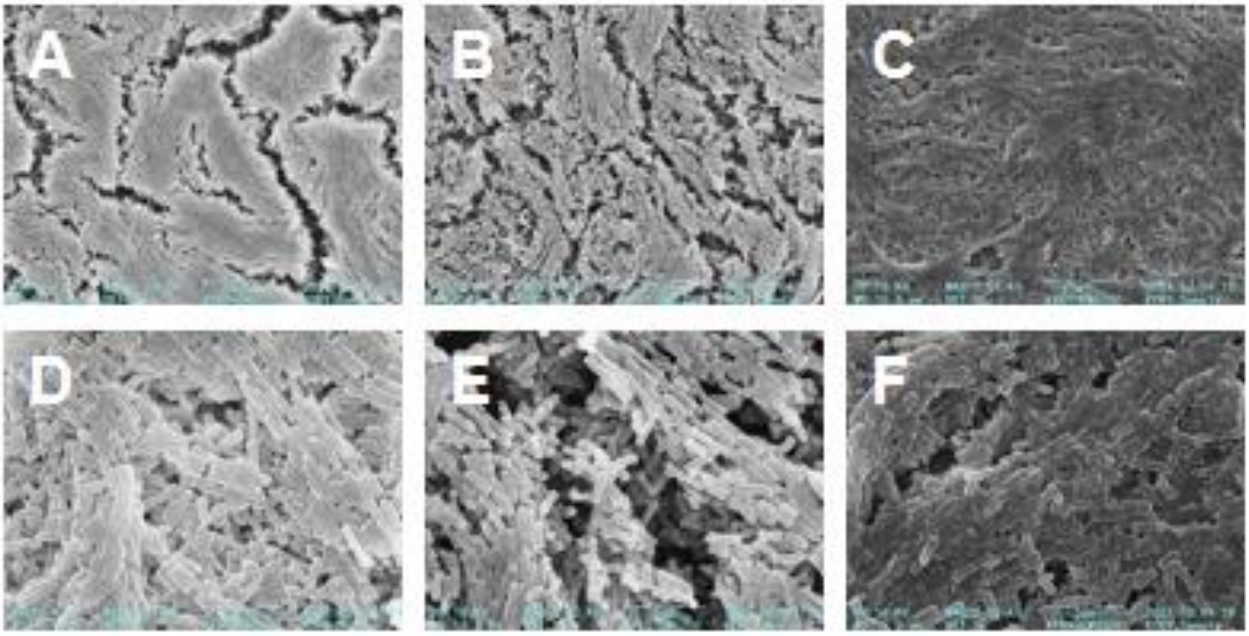

Figure 25 SEM monographs of tight arrangement biofilm with AR9 treatment after (A, D) 2h, (B, E) 4h, (C, F) 6h, A-C x1000 magnification with size bar 20 μm, D-F x5000 magnification with size bar 5 μm.

Conversely, in loosely organized *B. subtilis* 168 biofilms, phage lysate treatment elicited accelerated and pronounced structural alterations compared to compact architectures. Within three hours of exposure, significant contraction of bacterial cells became apparent (Fig. 26A, D), indicating early-stage morphological stress responses. By the sixth hour, dimensional changes affected most cells, with concurrent emergence of EPS on bacterial surfaces (Fig. 26B, E). This EPS production suggests activated defensive mechanisms against phage predation, potentially through matrix-mediated shielding.

The degradation trajectory culminated after 20 hours of treatment, when extensive cellular deformation dominated the biofilm landscape (Fig. 26C, F). Bacterial cells exhibited compromised membrane integrity while becoming increasingly dispersed within the residual matrix.

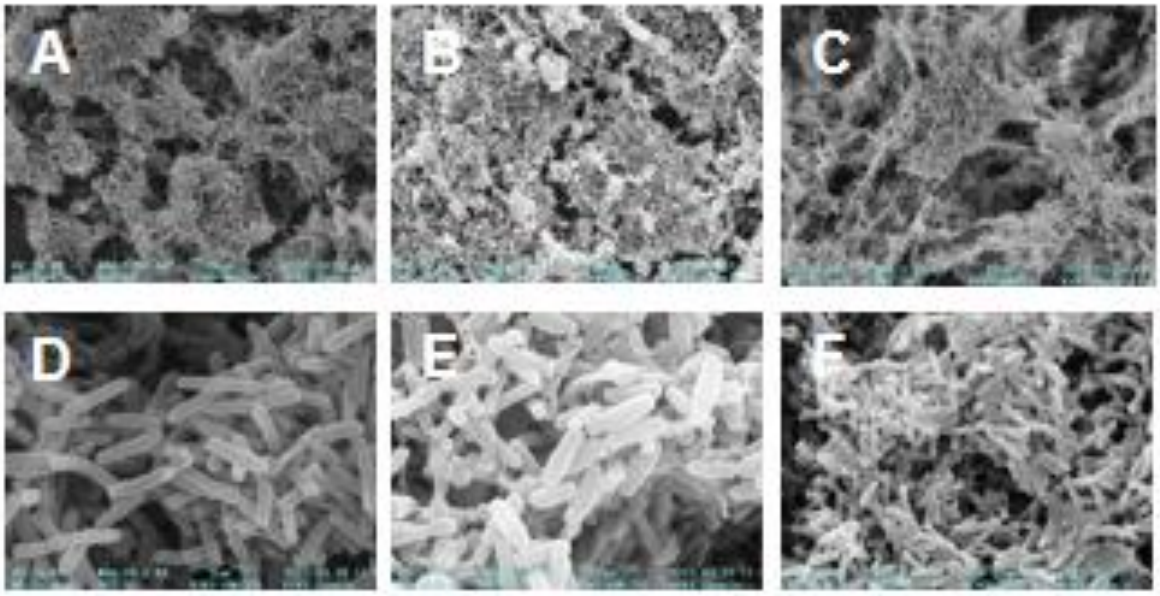

Figure 26 SEM monographs of loose arrangement biofilm with AR9 treatment after (A, D) 3h, (B, E) 6h, (C, F) 20h, A-C x1000 magnification with size bar 20 μm, D-F x5000 magnification with size bar 5 μm.

Systematic morphometric analysis was performed on phage lysate-treated *B. subtilis* 168 biofilms with loose architectures. One hundred bacterial cells were randomly selected from scanning electron micrographs at 3-hour, 6-hour, and 20-hour treatment intervals for dimensional quantification. Statistical analysis revealed significant increases in both cellular length and width between the 3-hour and 6-hour timepoints ($p^* < 0.001$ by ANOVA test). This dimensional expansion coincides temporally with initial phage penetration events and may be attributed to cytosolic DNA condensation and polarization during early lysis.

The observed sequence (Fig. 27), which from rapid dimensional changes (3 hr) through defensive EPS production (6 hr) to wholesale structural failure (20 hr), demonstrates how intrinsically disordered biofilms lack the protective inertia of compact structures. These biofilms are easier to destroy because the cell-cell adhesion and matrix

density are decreased, which can help phage penetration. These findings establish a clear correlation between biofilm structure and phage-mediated destruction, providing morphological reference for anti-biofilm phage-therapeutic development.

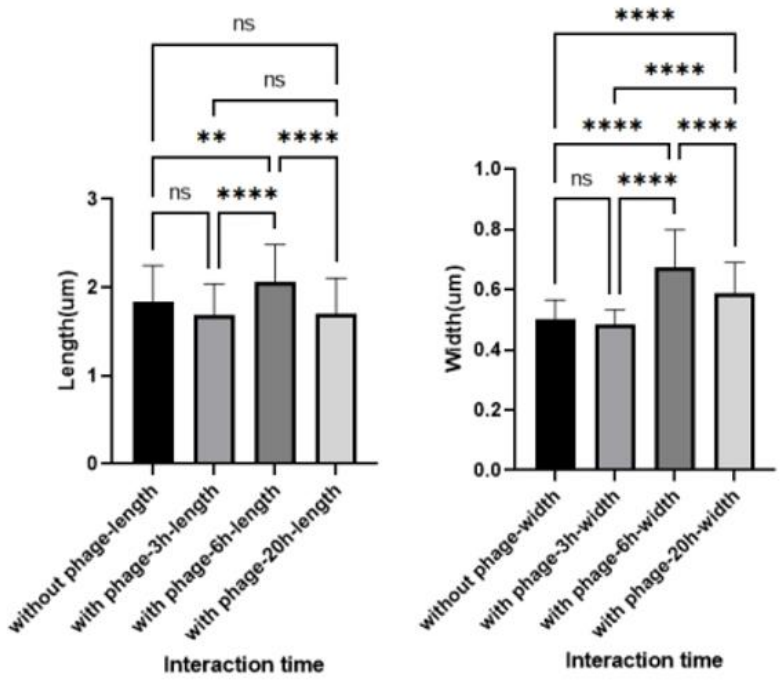

Figure 27 Significance analyzes of cell length and width changes, n=100

Biofilm formation is influenced by temperature and media composition, which affect microbe-environment interactions. Our studies revealed distinct structural patterns under different conditions, highlighting the importance of understand biofilm formation mechanisms for applications.

Biofilm structure showed strong media dependence, with LB forming compact cell aggregates and NB/DSM producing fibrous networks. Time-course studies in LB demonstrated progressive architectural changes: Day 3 showed woven patterns, Day 4 transitional states, and Day 5 disordered networks, revealing how nutrients and time shape biofilm topography.

Phage treatment responses varied by architecture. Ordered biofilms resisted initial

penetration (2 h) but developed cracks by 4 h, followed by EPS thickening (6 h). Disordered structures showed faster collapse, with cell elongation (3 h), EPS emergence (6 h), and complete disintegration by 20 h. Morphometric analysis confirmed significant cellular changes ($p<0.001$) during phage lysis, also it provides a new method reference for verifying the lysis of cells by phages.

5.4 Biofilm-phage interactions in *P. aeruginosa* isolates

5.4.1 PAO1 biofilm interaction with phages

For the *P. aeruginosa* pellicle biofilms after overnight grown at 37°C, results showed that a layer of thick biofilm was on the liquid-air interface of the broth medium. According to SEM images, biofilm has a dense structure with good three-dimensional matrix. Bacteria cells were tightly packed and uniform in size (about 1.2 μm). The light-colored microspheres and fibrous structures were considered to be EPS, most of cell surfaces were naked (Fig 28A, Fig 29A). After phage treatment for 2h, structure of biofilms significantly changes. Biofilm after 2h phiKZ treatment still shown compact arrangement of cells but large amount of EPS appeared as a collapsed network of filaments (Fig 28B). Less than half of bacteria cells are covered with filaments, and a few cells shown distortion (Fig 29B). While the cell arrangement of biofilm after 2h phiPB1 treatment was looser (Fig 28E). The viscosity of biofilms is lower, resulting in more cells shedding during sample processing (Fig 29E). In addition, the thin filaments are concerned not only EPS but also DNA from the destroyed cells after phage lysis, this speculation requires further studies to prove. After 4h phage phiKZ treatment, the biofilm structure was incomplete. The matrix becomes loose, and hollow structures appeared in

the middle of the biofilm (Fig 28C). A large number of bacteria cells were deformed and damaged, and more cells were covered with EPS compared with 2h-result (Fig 29C). Biofilm after 4h phiPB1 treatment shown similar performance in the low map (Fig 28F). However, the EPS matrix could not cover all bacteria cells and cell number became extremely low (Fig 29F). The biofilm-phage interaction was still in progress after 24h and became more complicated. In both samples, most of the biofilms lost their stickiness and were unable to adhere to the foil strips, however some exceptions can be seen in the figure. According to Fig 28D, EPS covered almost all the cells to defense phiKZ infection. And a new resistant colony with naked cells was shown clearly, this rapidly emerging phage resistance phenotype also leads to limitations in biofilm clearance. For phiPB1 treatment sample, there were only a few damaged cells and a large number of filament structures on the surface of the biofilm (Fig 29G).Moreover, the three-dimensional structure of the biofilm makes us suspect that there are still intact cells in the center or under the biofilm, which are protected by EPS and damaged cells from the surface (Fig 28G), and it may require more time for phage to lysis.

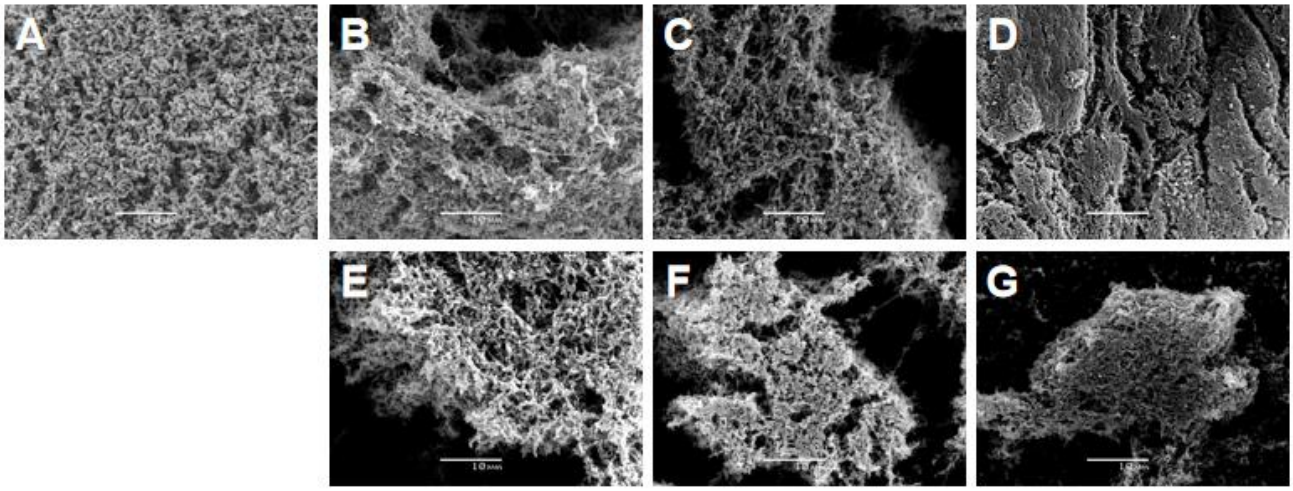

Figure 28 Scanning electron microscope images of PAO1 biofilm under 2500 x magnification after overnight culture (A) without phage treatment, (B) after 2hrs phage phiKZ treatment, (C) after 4hrs phage phiKZ treatment. (D) after 24hrs phage phiKZ treatment, (E) after 2hrs phage PB1 treatment, (F) after 4hrs phage PB1 treatment, (G) after 24hrs phage PB1 treatment Size bar-10um (Wang et al, 2025).

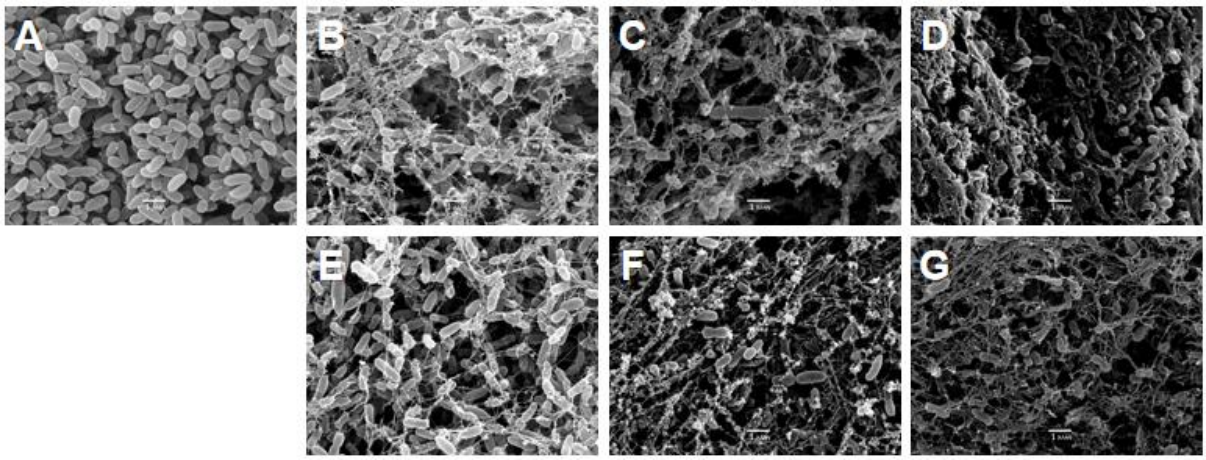

Figure 29 Scanning electron microscope images of PAO1 biofilm under 10000 x magnification after overnight culture (A) without phage treatment, (B) after 2hrs phage phiKZ treatment, (C) after 4hrs phage phiKZ treatment.， (D) after 24hrs phage phiKZ treatment, (E) after 2hrs phage PB1 treatment, (F) after 4hrs phage PB1 treatment, (G) after 24hrs phage PB1 treatment, size bar-1um (Wang et al, 2025).

Extended exposure of mature *P. aeruginosa* PAO1 biofilms to bacteriophages revealed developmental stage-dependent responses.

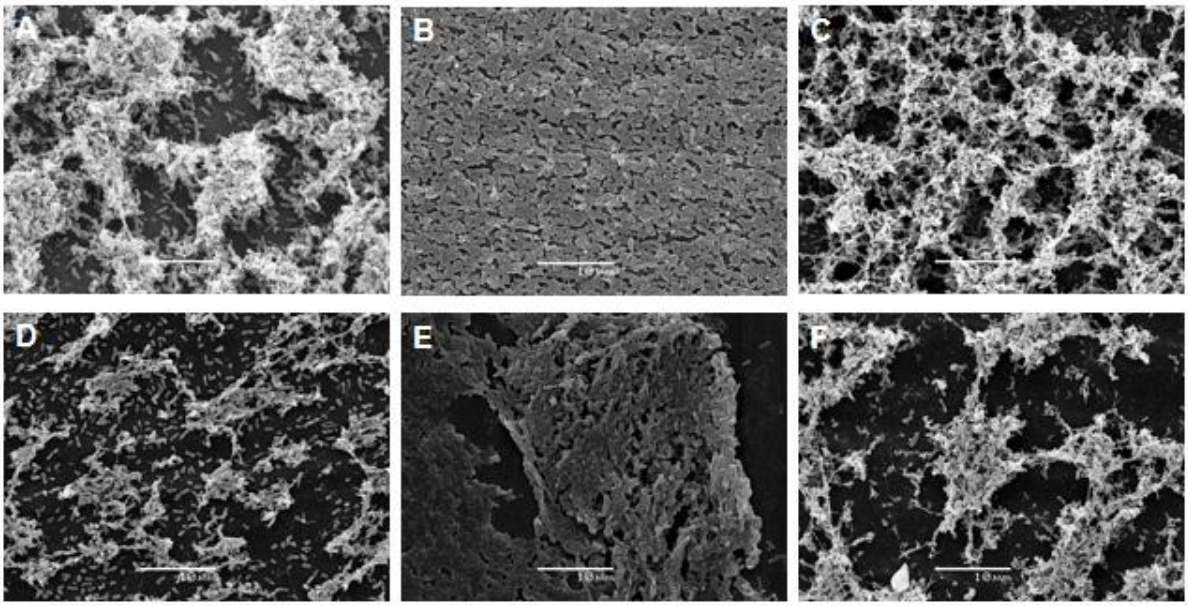

Figure 30 SEM images of PAO1 biofilm under 2500 times magnification after 2d culture (A) without phage treatment, (B) after 3d phage phiKZ treatment, (C) after 3d phage PB1 treatment; PAO1 biofilm under 2500 times magnification after 4d culture (D) without phage treatment, (E) after 3d phage phiKZ treatment, (F) after 3d phage PB1 treatment Size bar-10um

Two-day biofilms exhibited loosely aggregated cellular clusters with interwoven EPS networks, indicative of structural maturation (Fig. 30A). In contrast, four-day biofilms displayed reduced aggregation thickness and increased dispersed cells (Fig. 30D), characteristic of dispersal-phase transition. Following 72-hour phiKZ treatment, both biofilm ages developed thick EPS coatings—though with distinct distribution patterns. Two-day biofilms showed superficial EPS encapsulation limited to surface layers (Fig. 30B), while four-day counterparts demonstrated uniform 3D EPS encasement permeating the entire matrix (Fig. 30E). Conversely, PB1-treated biofilms retained control-like architecture with woven EPS networks but exhibited significant degradation markers: two-day structures displayed loosened cellular cohesion (Fig. 30C), and four-day biofilms accumulated extensive lytic debris (Fig. 30F).

Cell viability within *P. aeruginosa* PAO1 biofilms was quantified using differential fluorescent staining with DAPI (4',6-diamidino-2-phenylindole) and propidium iodide (PI). DAPI permeates intact membranes to label all cellular DNA, while PI exclusively enters membrane-compromised cells, serving as a death indicator.

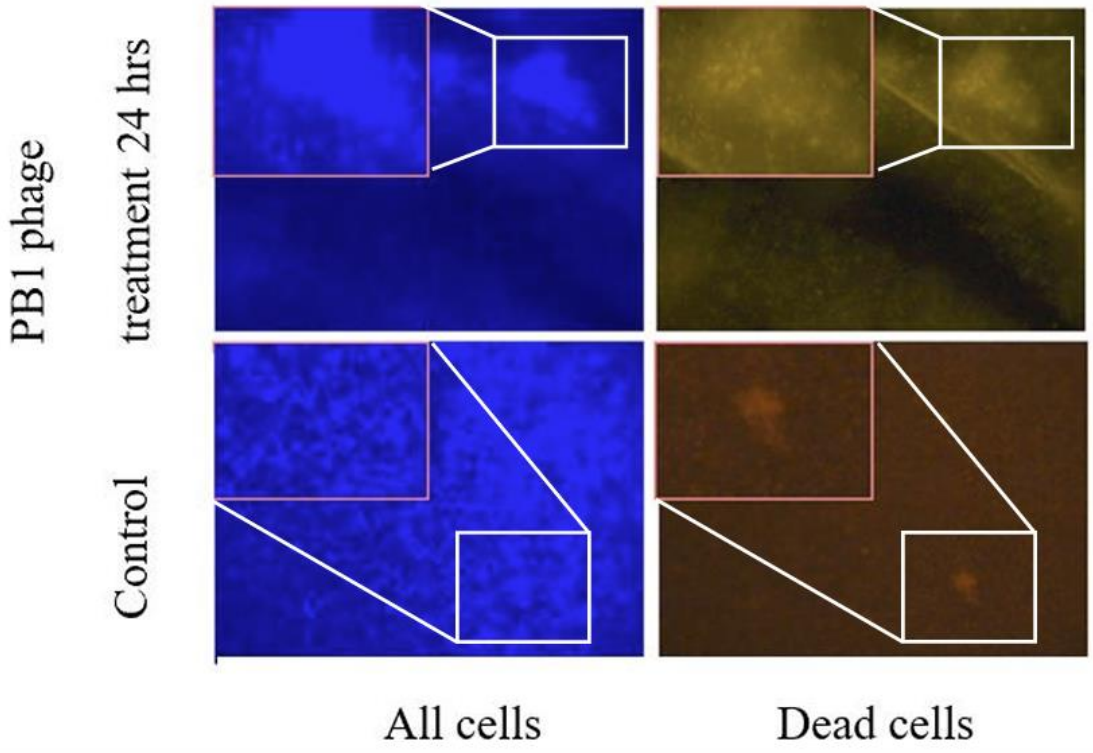

Figure 31 Fluorescent microscope images of PAO1 biofilm with live-dead assay (staining with DAPI-PI). Left - DAPI, right -PI. Insertions: 200× magnification

Control biofilms exhibited predominantly viable communities, with rare PI-positive cells confirming viability (Fig.31). In stark contrast, PB1-treated samples following overnight incubation demonstrated extensive PI staining throughout the biofilm architecture. This pervasive signal indicates widespread membrane disintegration consistent with phage-mediated lysis. These findings corroborate prior SEM observations of cellular distortion and structural collapse in PB1-exposed biofilms.

5.4.2 Effect of pH onto PAO1 biofilm - phage interactions

Saline and Phosphate-buffered saline(PBS) buffer are both widely used solvents in biological experiments and Saline Magnesium buffer (SM) is one of the most common buffer for preservation and dilution of bacteriophages. SM buffer is a neutral solution (pH value 7.0), whereas saline and PBS are weakly acidic solutions (pH value around 5.5).

All 24h control samples have significant changes compared with 24h phage treatment samples, which means the large morphology different in 24h phage treatment samples can due to phage-biofilm interaction. The lower magnification images show that the cells of the biofilm are more tightly packed when the biofilm interacts with the phage in acidic environments (Fig. 32-34). According to the 2h, 4h samples, the biofilms exposed to PBS presented more and denser EPS structure (Fig. 32A-D). Compared to the samples in saline (Fig. 34A-D), which may be due to the regulatory effect of the presence of potassium ions in PBS solution on the biofilms [115]. Moreover, biofilm in neutral pH solution SM has low amount of polysaccharide (Fig. 33), this may be due to SM buffer can decrease the viscosity of destroyed cell DNA/polysaccharide or the buffer may influence the physiological changes of bacteria thus produce less polysaccharide. Biofilm self-defense mechanisms may have changed under different pH conditions. Due to the extensive reduction of polysaccharides in biofilms, cells spontaneously align into a spatial topology in the SM-neutral environment, with cells closely connected by very few polysaccharides. The size of cells are smaller compare to the other samples. However, in the acidic solution, more cells were connected by fibrous structures, and the space between cells was large and irregular.

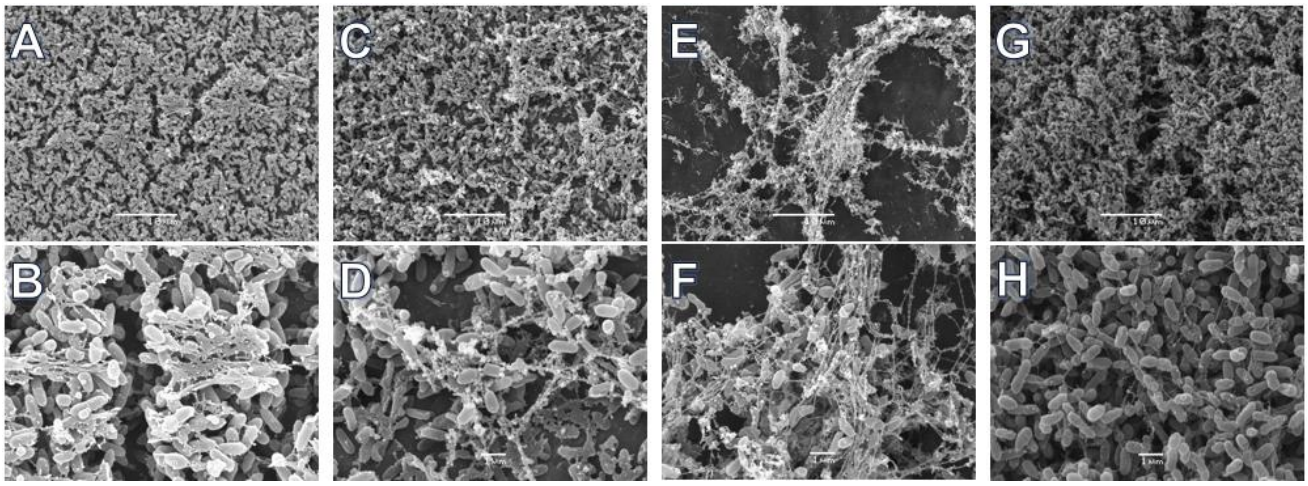

Figure 32 SEM study of biofilm degradation under PBS condition, (A-F) with phage PB1, (G, H) without phage. (A, B) after 2 hr phage treatment; (C, D) after 4 hr phage treatment; (E, F) after 24 hr phage treatment; (G, H) 24 hr control without phage. A, C, E, G: Magnification 2500x. Bar size – 10μm. B, D, F, H: Magnification 10000x. Bar size – 1μm (Wang et al, 2025).

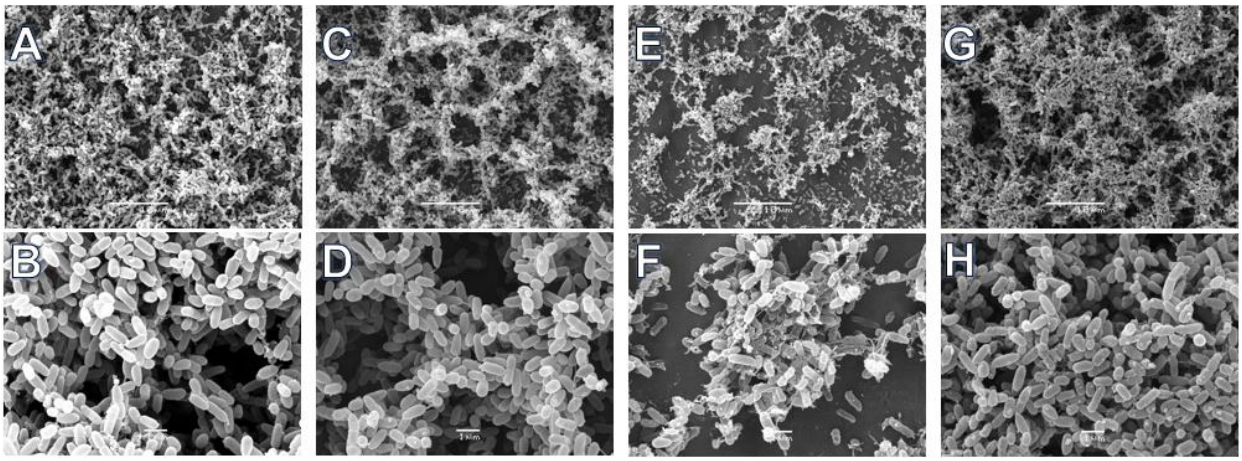

Figure 33 SEM study of biofilm degradation under SM condition, (A-F) with phage PB1, (G, H) without phage. (A, B) after 2 hr phage treatment; (C, D) after 4 hr phage treatment; (E, F) after 24 hr phage treatment; (G, H) 24 hr control without phage. A, C, E, G: Magnification 2500x. Bar size – 10μm. B, D, F, H: Magnification 10000x. Bar size – 1μm (Wang et al, 2025).

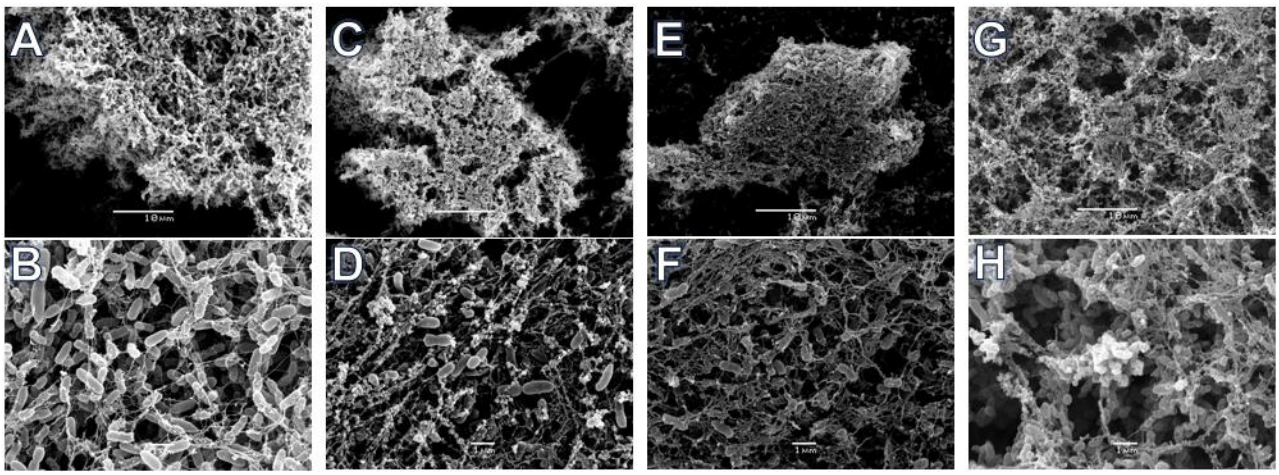

Figure 34 SEM study of biofilm degradation under saline condition, (A-F) with phage PB1,(G, H) without phage. (A, B) after 2 hr phage treatment; (C, D) after 4 hr phage treatment; (E, F) after 24 hr phage treatment; (G, H) 24 hr control without phage. A, C, E, G: Magnification 2500x. Bar size – 10μm. B, D, F, H: Magnification 10000x. Bar size – 1μm (Wang et al, 2025).

Mechanisms of biofilm antibiotic resistance have been described in previous research, and these are either the cause or the effect of pH changes within the biofilm [116]. *P. aeruginosa* biofilm can secrete the exopolysaccharides Psl, Pel and alginate which are significant elements involved in surfaces adhesion [117]. The impact of pH on the biofilm polysaccharide's synthesis corresponds to the impact of pH on biofilms [118]. The different behaviors from phage-biofilm interaction may also relate pH influence on bacteriophage activity. Environmental pH can change the charge state of the amino acids in bacteriophage capsids, thus lead to different behaviors such as virus aggregation [119]. In our study, we use saline, PBS buffer and SM buffer to evaluate effects of biofilm-phage interaction under different pH environments. The SEM images verified that the behaviors of phage-biofilm interaction can be changed with different buffers, including the number of polysaccharides, the size of cells and the biofilm structure matrix, so the conditions of

environment should be also considered during phage therapy. Moreover, we suggest that the efficiency of phage therapy shall be different *in vivo* based on human organs has different pH environment. In addition, our method based on the *P. aeruginosa* laboratory strain PAO1 and phage PB1 interaction under pH changes could also be used as a template for the study of the interaction between different strains and phages.

5.4.3 Clinical isolates of *P.aeruginosa* treatmemt

5.4.3.1 Clinical isolate Ur1

The clinical isolate *P. aeruginosa* Ur1 exhibited distinctive, yellow-pigmented colonies with smooth surface morphology and demonstrated pan-resistance to clinically relevant antibiotics including β-lactams, fluoroquinolones, and aminoglycosides, establishing a multidrug-resistant phenotype. Lytic phage screening identified PhiKZ (ΦKZ-like myovirus) and 14/1 (PB1-like podovirus) as highly effective agents, both producing well-defined inhibition zones in susceptibility assays (Fig. 35). Quantitative crystal violet analysis confirmed significant biofilm eradication after 24-hour phage treatment, with PhiKZ achieving 83.8% clearance and 14/1 reaching 81.1% efficiency.

Scanning electron microscopy revealed sequential architectural transformations during phage exposure. Initial low-magnification views depicted dense, planar biofilm matrices (Fig. 37A), while high-resolution examination showed characteristically loose cellular arrangements with substantial intercellular voids (Fig. 36A). After two hours of phage exposure, macrostructural integrity remained intact, though high-magnification imaging detected incipient cellular deformation - PhiKZ-treated samples developed fibrous EPS (Fig. 36B), whereas 14/1-exposed biofilms exhibited increased cellular

packing density with minimal EPS production (Fig. 36E). By four hours, both phage treatments induced extensive crack networks resembling jigsaw puzzles at low magnification (Fig. 37C, F), signaling structural compromise, while high-resolution views confirmed enhanced EPS secretion and progressive cellular dispersion (Fig. 36C, F). After 24 hours of exposure, macroscale divergence emerged: PhiKZ caused large-scale biofilm delamination with surface collapse (Fig. 37D), while 14/1 induced cellular disaggregation without bulk detachment (Fig. 37G); high-resolution views showed near-complete EPS encapsulation (Fig. 36D, G).

Ur1's biofilm architecture - characterized by high viscosity, low elastic recovery, and loose cellular organization with large intercellular spaces - facilitated deep phage penetration and high eradication efficiency. Despite substantial biomass removal, residual EPS networks maintained structural continuity, revealing a distinct dissociation between physical integrity and functional viability in phage-treated biofilms that underscores the complex interplay between matrix architecture and antimicrobial efficacy.

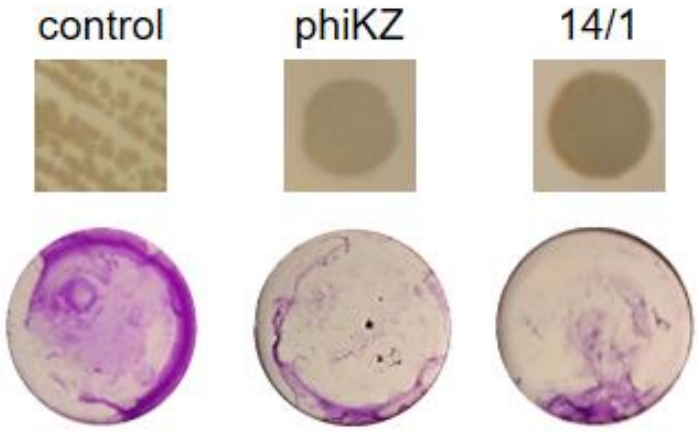

Figure 35 The colony, plaque assay of Ur1 (top) and biofilm crystal violent staining (bottom).

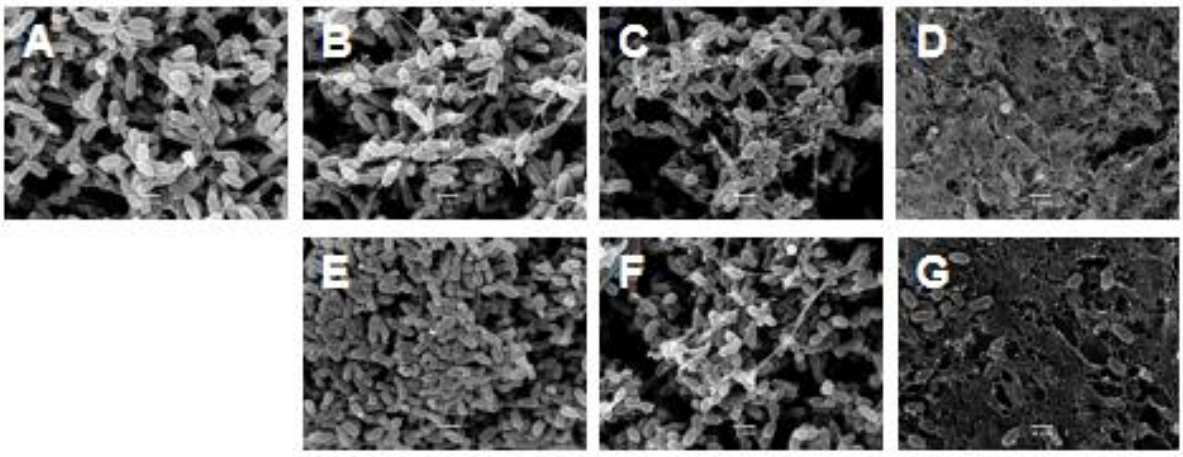

Figure 36 Scanning electron microscope images of Ur1 biofilm under 10000 times magnification (A) without phage treatment, (B) after 2h phage phiKZ treatment, (C) after 4h phage phiKZ treatment, (D)after 24h phage phiKZ treatment (E) after 2h phage 14/1 treatment, (F) after 4h phage 14/1 treatment, (G) after 24h phage 14/1 treatment, Bar size – 1μm.

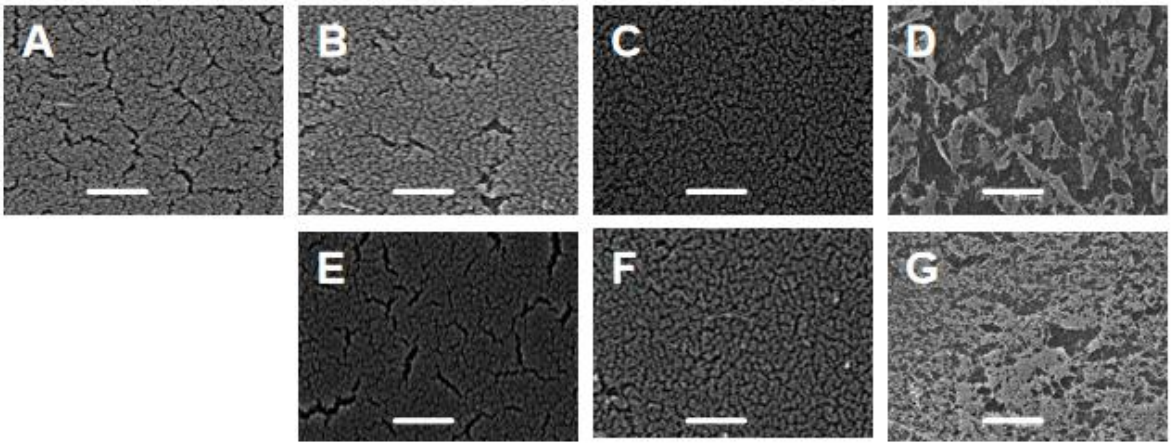

Figure 37 Scanning electron microscope images of Ur1 biofilm under 500 times magnification (A) without phage treatment, (B) after 2h phage phiKZ treatment, (C) after 4h phage phiKZ treatment, (D)after 24h phage phiKZ treatment (E) after 2h phage 14/1 treatment, (F) after 4h phage 14/1 treatment, (G) after 24h phage 14/1 treatment, Bar size – 50μm.

5.4.3.2 Clinical isolate Ur14

The clinical isolate Ur14 formed distinct, green-pigmented colonies with compact

morphology and demonstrated pan-resistance to all tested antibiotics. As the most recalcitrant biofilm in this study, it exhibited exceptional tolerance to five lytic phages spanning three taxonomic families: PhiKZ/NN (ΦKZ-like), 10/2 (PB1-like), and NFS/FMV (KMV-like), all producing clear inhibition zones of identical diameter at 10^8 PFU/mL. Scanning electron microscopy revealed its unique structural features: untreated biofilms displayed extraordinarily dense architectures with minimal intercellular space at 500× magnification, while 10,000× imaging confirmed near-impenetrable cellular packing.

Following phage exposure, SEM documented limited structural compromise. After 2 hours, all treatments induced superficial cracking, with FMV-treated biofilms retaining the greatest integrity. By 24 hours, block-like detachment occurred across samples, though residual cellular aggregates persisted - particularly in FMV-exposed specimens. High-resolution imaging revealed a rapid defensive response: within 2 hours, dense fibrous extracellular polymeric substances (EPS) completely enveloped cells, intensifying by 24 hours without significant biomass reduction. This pervasive EPS matrix formed physical barriers restricting phage diffusion, as evidenced by minimal cellular deformation or debris despite prolonged exposure (Fig. 39).

Quantitative crystal violet assays (Fig. 38) confirmed profound resistance: clearance efficiencies remained critically low across all phages (10/2:21.5%; NN:34.2%; PhiKZ:27.9%; FMV:23.5%; NFS:30.5%). Even combinatorial phage cocktails (phiKZ/PB1/NFS) achieved only marginal improvement (42.1%), indicating fundamental resistance mechanisms.

This recalcitrance stems from Ur14's hyper-biofilm phenotype: intense pyocyanin

secretion enhances matrix crosslinking, while rigid cellular packing provides structural resilience. The retained 3D architecture after treatment confirms persistent protected niches where subsurface cells evade phage penetration. These findings necessitate combinatorial approaches (e.g., EPS-degrading enzymes with phage cocktails) to overcome Ur14's multifactorial resistance, representing a critical challenge for clinical phage implementation against armored biofilm phenotypes. Future mechanistic studies should employ transcriptomics to delineate the genetic basis of its exceptional defensive capabilities.

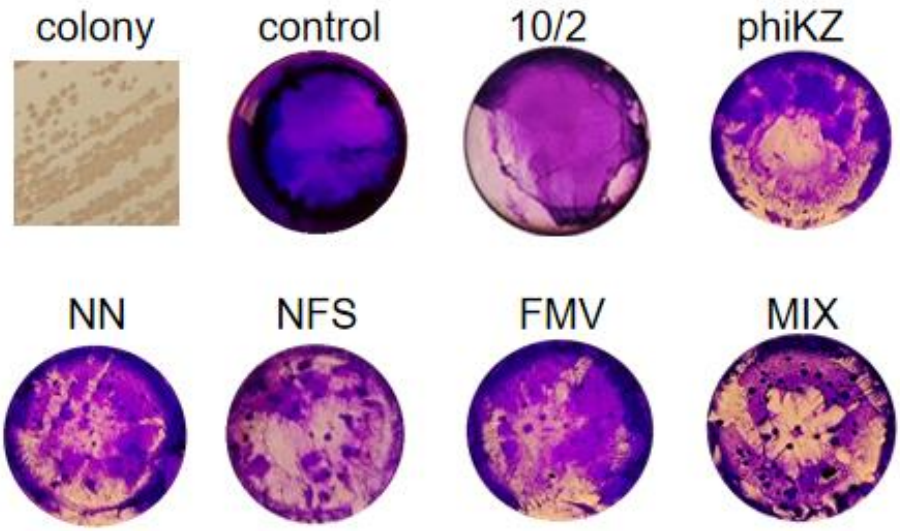

Figure 38 The colony of Ur14 and biofilm crystal violent staining.

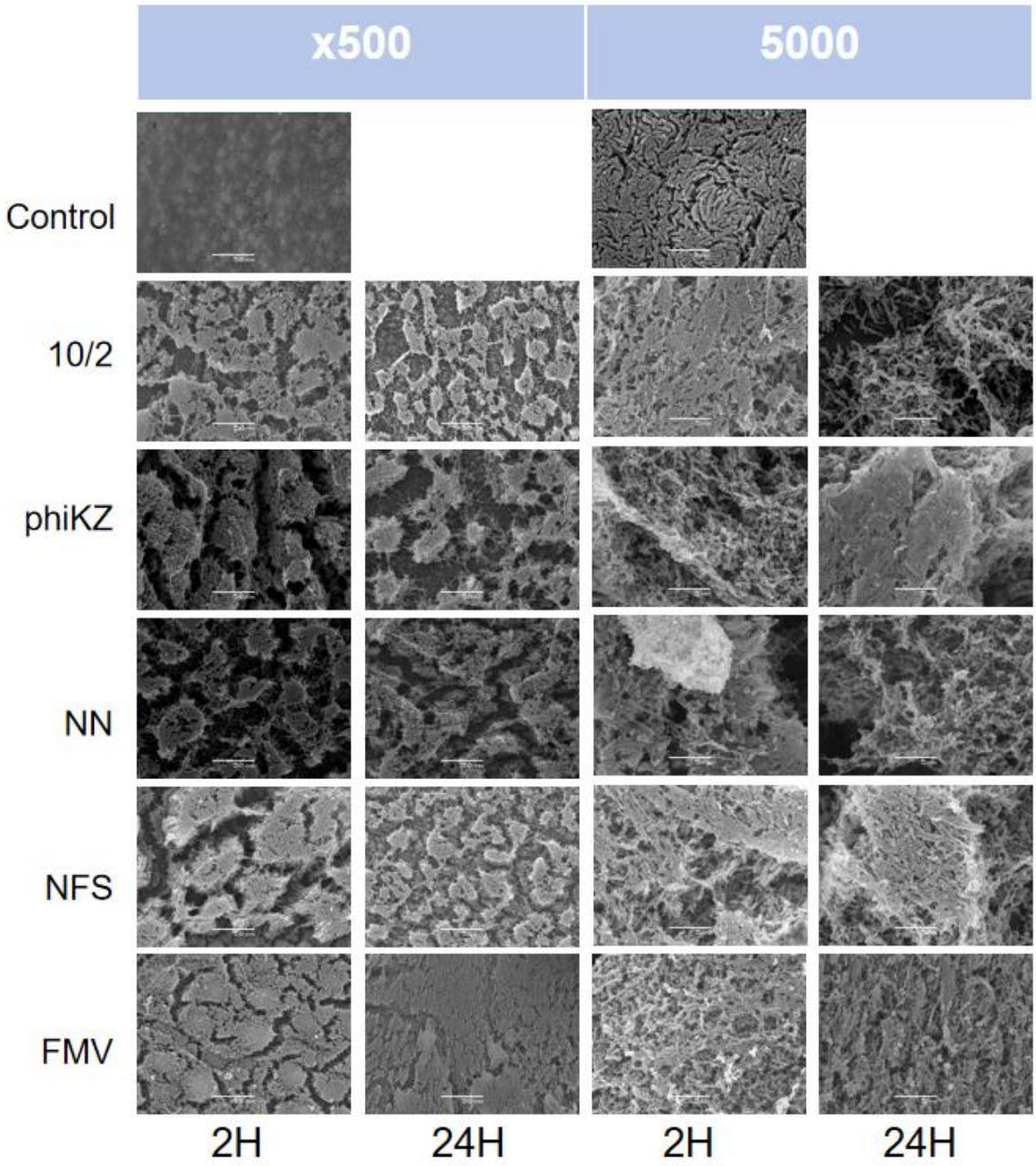

Figure 39 Scanning electron microscope images of Ur14 biofilm under 500 and 5000 times magnification with 2h and 24h different phages treatment. Bar size – 50μm for x500 and 5μm for x10000.

5.4.3.3Clinical isolate Lu3

The *P. aeruginosa* Lu3 isolate exhibited distinctive yellow-green pigmented colonies with smooth surface morphology and demonstrated pan-resistance to clinically relevant antibiotics. Phage susceptibility screening identified phiOP (ΦKZ-like) and 10/2

(PB1-like) as effective lytic agents, both producing inhibition zones of identical diameter (Fig. 40) at equivalent concentrations (10^8 PFU/mL). Scanning electron microscopy revealed architecture: untreated biofilms displayed thin, planar structures with pre-existing fissures at 500× magnification, while 10,000× imaging showed moderately compact cellular arrangements with minimal intercellular spacing (Fig. 41, 42).

Following 2-hour phage exposure, low-magnification imaging revealed divergent destruction patterns: 10/2-treated biofilms underwent uniform surface erosion with topographical roughening (Fig. 41E), whereas phiOP-exposed samples exhibited patchy delamination of intact cell clusters while preserving underlying structural integrity (Fig. 41B). By 4 hours, both treatments showed advanced disintegration - 10/2-treated matrices degraded to monolayer cellular coverage while phiOP-exposed specimens displayed progressive dissolution of cellular aggregates (Fig. 41C, F). Remarkably, 24-hour treatment induced contrasting architectural transformations: phiop-treated biofilms regressed to isolated cell clusters (Fig. 41D), while 10/2-exposed samples remained large amount of cellular aggregates (Fig. 41G).

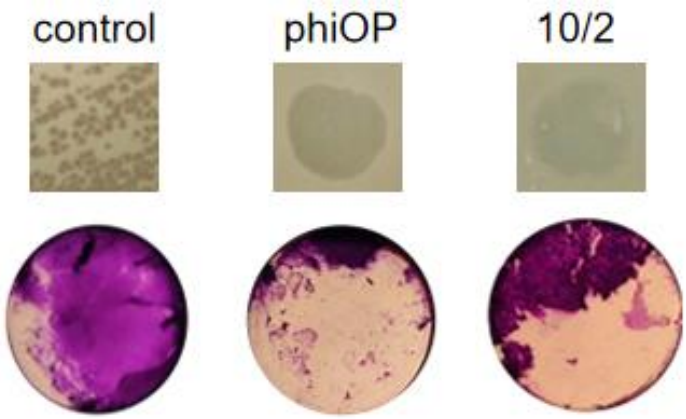

Figure 40 The colony, plaque assay of Lu3 (top) and biofilm crystal violent staining (bottom).

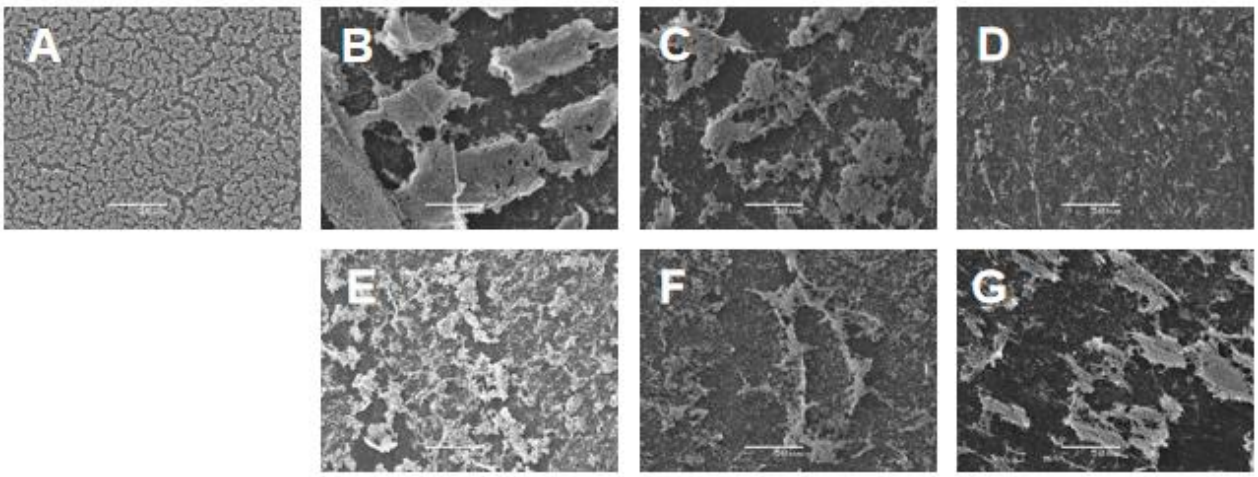

Figure 41 Scanning electron microscope images of Lu3 biofilm under 500 times magnification (A) without phage treatment, (B) after 2h phage phiOP treatment, (C) after 4h phage phiOP treatment, (D)after 24h phage phiOP treatment (E) after 2h phage 10/2 treatment, (F) after 4h phage 10/2 treatment, (G) after 24h phage 10/2 treatment, Bar size – 50µm.

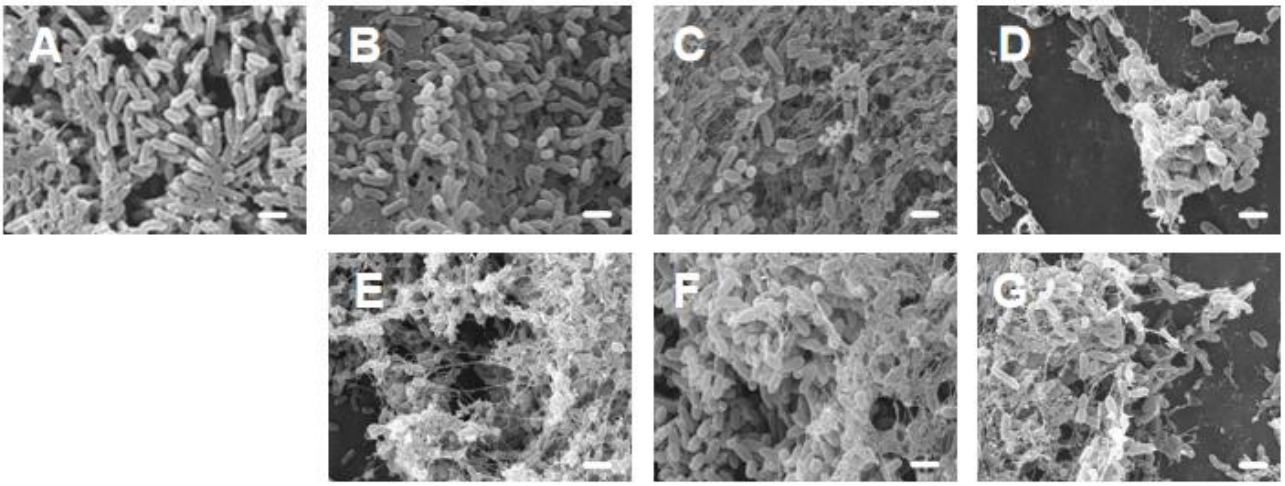

Figure 42 Scanning electron microscope images of Lu3 biofilm under 10000 times magnification (A) without phage treatment, (B) after 2h phage phiOP treatment, (C) after 4h phage phiOP treatment, (D)after 24h phage phiOP treatment (E) after 2h phage 10/2 treatment, (F) after 4h phage 10/2 treatment, (G) after 24h phage 10/2 treatment, Bar size – 1µm.

High-resolution imaging documented extensive fibrous extracellular polymeric substance (EPS) production within 2 hours post-exposure. The 10/2-treated specimens

developed significantly more disorganized EPS networks compared to phiOP-exposed counterparts (Fig. 42B, E). After 24 hours, both treatments showed substantial biomass reduction with pervasive EPS matrices enveloping residual structures, though phiop-treated biofilms exhibited more pronounced structural decomposition (Fig. 42D, G). Quantitative crystal violet assays confirmed differential clearance efficiencies aligning with structural observations: phiOP achieved 70.7% biofilm eradication, while 10/2 showed significantly lower efficacy at 59.1%.

These findings demonstrate that despite similar initial lytic effects, phiOP's capacity to penetrate and disintegrate cellular aggregates underlies its superior clearance performance. The extensive yet disorganized EPS networks in 10/2-treated specimens likely impeded complete biofilm eradication, exemplifying how phage-specific matrix modulation governs therapeutic outcomes.

5.4.3.4 Clinical isolate Lu9

The Lu9 isolate formed distinctive yellow colonies with larger morphology than other comparator strains. And it is shown multidrug resistance to common antibiotics while retaining susceptibility to amikacin, gentamicin and ciprofloxacin. Phage susceptibility screening identified phiKZ (ΦKZ-like) and PB1 (PB1-like) as effective lytic agents, both producing inhibition zones of identical diameter at standardized concentrations (10^8 PFU/mL) (Fig. 43). Scanning electron microscopy revealed time-dependent architectural alterations: untreated biofilms exhibited dense, porous matrices at low magnification (500×), with high-resolution imaging (10,000×) confirming compact cellular arrangements featuring minimal intercellular spacing.

Following phage exposure, initial structural changes were modest at 2 hours across both treatments (Fig. 44, 45). By 4 hours, low-magnification imaging showed convergent disruption patterns - surfaces developed uniform erosion with cellular detachment and topographical roughening. After 24 hours, extensive block-like delamination occurred in both groups, though PB1 treatment caused significantly larger areas of detachment (Fig. 44G). Residual biofilm segments maintained aggregated cluster formations in all specimens. High-resolution analysis revealed consistent cellular loosening without early-stage EPS production (Fig. 45B, C, E, F) - a distinctive feature separating Lu9 from other strains. Small number of fibrous EPS finally emerged after 24 hours (Fig. 45D, G), partially encapsulating residual cells with widespread biofilm decomposition. Notably, cellular debris was obviously absent, we suggested it is because of low biofilm viscosity and sample loss during processing.

Crystal violet assays confirmed quantitative efficiency of biofilm clearance: phiKZ achieved 62.6% eradication, while PB1 reached 79.0%. These results are corelated with Lu9's intermediate biofilm decomposition performance : less than Ur14's resistance but shown more susceptible than Ur1's loosely organized matrices. The delayed EPS production and less cell debris demonstrate unique viscoelastic property which can influence both structural changes and quantitative analytical results.

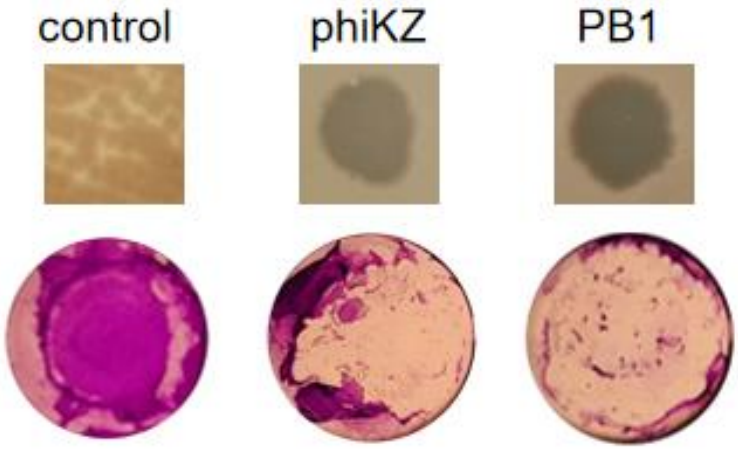

Figure 43 The colony, plaque assay of Lu9 (top) and biofilm crystal violent staining (bottom).

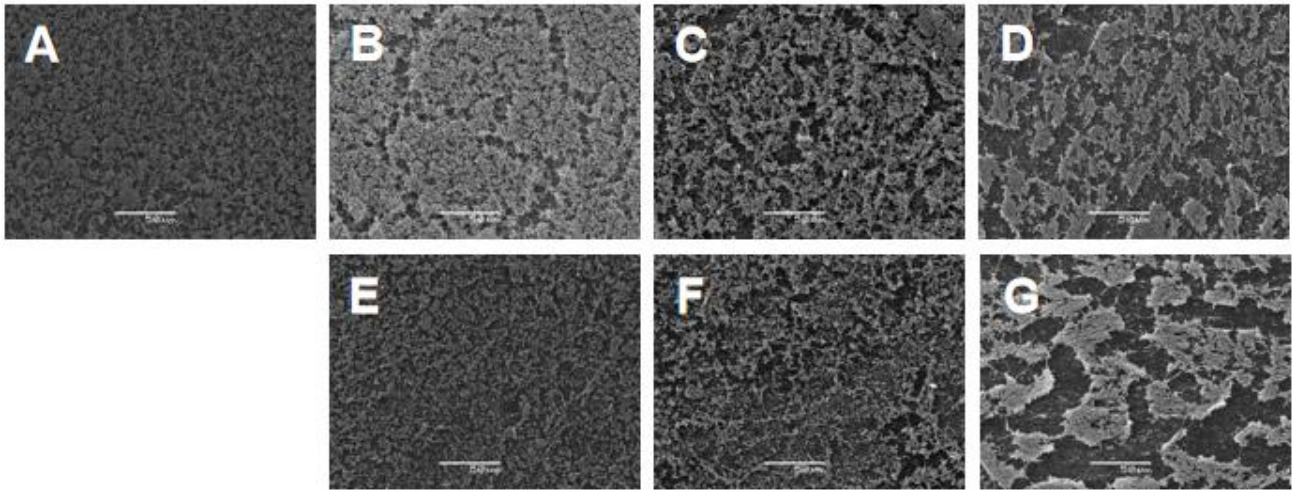

Figure 44 Scanning electron microscope images of Lu9 biofilm under 500 x magnification (A) without phage treatment, (B) after 2h phage phiKZ treatment, (C) after 4h phage phiKZ treatment, (D)after 24h phage phiKZ treatment (E) after 2h phage PB1 treatment, (F) after 4h phage PB1 treatment, (G) after 24h phage PB1 treatment, Bar size – 50µm.

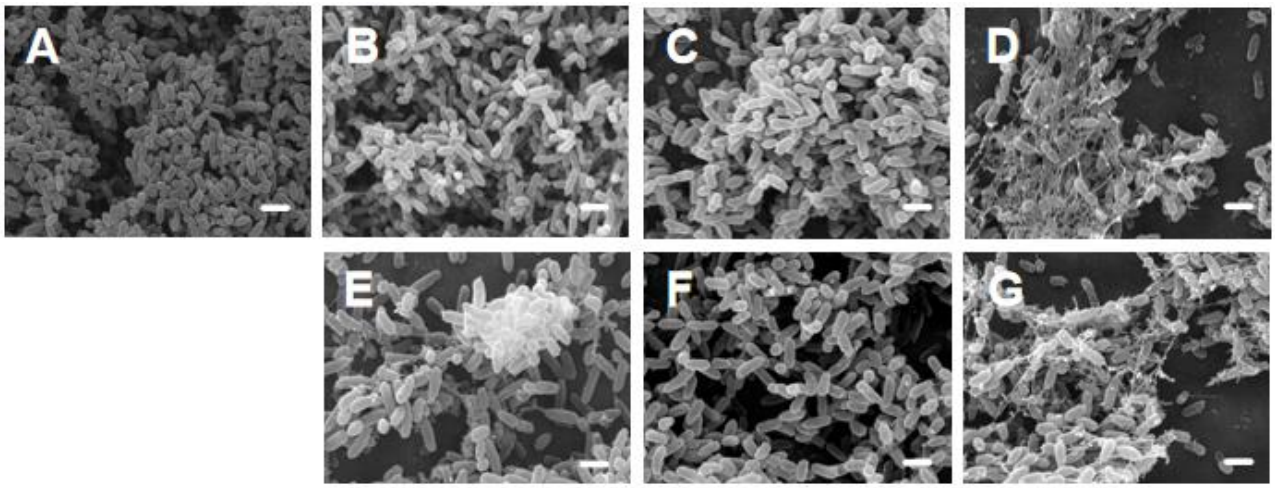

Figure 45. Scanning electron microscope images of Lu9 biofilm under 10000 x magnification (A) without phage treatment, (B) after 2h phage phiKZ treatment, (C) after 4h phage phiKZ treatment, (D)after 24h phage phiKZ treatment (E) after 2h phage PB1 treatment, (F) after 4h phage PB1 treatment, (G) after 24h phage PB1 treatment, Bar size – 1μm

5.5 Design of scaffolds with antimicrobial properties

To address the issues of easy volatilization and poor retention of liquid phage formulations at wound sites—particularly in specialized wound environments such as bone defect repair or dental treatments—it is necessary to construct functionalized carrier scaffolds. An ideal carrier should enable efficient phage loading and controlled release while maintaining physical stability at the implantation site and effectively overcoming microbial colonization on implant surfaces that may interfere with therapeutic efficacy. By systematically optimizing the physicochemical and biological properties of the carrier, we ultimately aim to develop a precision drug delivery system capable of meeting the diverse clinical needs of wound treatment. This chapter aims to develop a phage lysate-based carrier system for treating wound infections, the study comprehensively

characterizes the structural, physicochemical, and functional properties of silk fibroin (SF)-based scaffolds modified with polyethyleneimine (PEI) and/or chitosan and functionalized with bacteriophages.

5.5.1 Preparation of silk fibroin scaffolds

The SF solution was regenerated by dissolving SF in a ternary solvent system followed by dialysis and concentration adjustment to 20 mg/mL. Various scaffold formulations were then prepared: pure SF scaffolds were fabricated by blending the stock solution with 1% DMSO and cryopreserving at -80 ℃; SF-gelatin composites were prepared by mixing SF with gelatin (7:3 ratio) before freezing at -30 ℃; SF-gelatin-chitosan scaffolds incorporated chitosan at different ratios (7:3:1-7:3:5) using similar cryogenic processing. Additionally, SF scaffolds were chemically crosslinked with PEI through pH-controlled immersion and ultrasonic treatment. All scaffold types underwent standardized post-processing with pure ethanol thawing and distilled water rinsing. For phage functionalization, prefabricated scaffolds were incubated with phage lysates (10^6-10^9 PFU/mL) overnight. Then gentle washing to remove unbound phages on the surface. The final products were stored at 4 ℃ for subsequent experiment.

5.5.2 Biophysical characteristics of scaffolds

5.5.2.1 Swelling rate[2]

The swelling behavior of biomaterials can directly influence their permeability characteristics and play an important role in regulating the transport of essential nutrients,

[2] This work was done with the help of Dr Tolbert Osire (SMBU)

metabolic gases, and cellular waste products. As shown in Table 1, all the scaffolds had high swelling rates above 85 %. The data shows a clear result that PEI modification changed the swelling rate. This effect was consistent and happened in all four scaffold types, including SF20, SFG, SFGC731 and SFGC735. In each case, the PEI-modified sample exhibits a statistically significant reduction in swelling rate compared to the unmodified ones. Specifically, the swelling rates decreased by 5% (SF20-PEI: 91% with SF20: 96%), 6% (SFG-PEI: 88% with SFG: 94%), 6% (SFGC731-PEI: 92% with SFGC731: 98%), and 4% (SFGC735-PEI: 93% with SFGC735: 97%). This situation is mainly attributable to the introduction of PEI - a highly branched cationic polymer, which increases the scaffold's crosslinking density through ionic interactions and potential covalent bonding. This crosslinking creates a tight polymeric network, and reduces the average pore size of the scaffold matrix. Consequently, the smaller pore dimensions, combined with electrostatic repulsion from PEI cationic charge, significantly impede water molecule penetration and diffusion, which lead to lower water uptake and retention.

Table 1.The water swelling rate of the SF-based scaffolds

Scaffold Type	Swelling rate (%)
SF20	96
SF20-PEI	91
SFG	94
SFG-PEI	88
SFGC731	98
SFGC731-PEI	92
SFGC735	97
SFGC735-PEI	93

Scaffolds incorporating chitosan (SFGC731 and SFGC735) exhibit the highest baseline swelling rates among the unmodified groups (98% and 97% respectively), exceeding those of SF20 (96%) and SFG (94%). This increased hydrophilicity is directly linked to the intrinsic properties of chitosan. As a highly hydrophilic, linear polysaccharide rich in hydroxyl and amine groups, chitosan possesses a strong affinity for water molecules through hydrogen bonding. Its incorporation into the scaffold matrix enhances the material's capacity for hydration. Furthermore, the flexible chains of chitosan may contribute to a softer scaffold structure, potentially facilitating greater water absorption and swelling compared to scaffolds without chitosan. While PEI modification still reduced swelling in the chitosan-containing scaffolds (SFGC731-PEI and SFGC735-PEI), their absolute swelling rates remained relatively high (92% and 93%), reflecting the counteracting influence of chitosan's inherent hydrophilicity against the pore-restricting effect of PEI. Minor variations between SFGC731 and SFGC735 likely stem from differences in their specific chitosan content or processing parameters.

5.5.2.2 Degradation[1]

The biodegradation behavior of silk fibroin scaffolds was investigated in simulated physiological environments (0.01 M PBS, 37 °C) containing various enzymatic solutions: lysozyme (2 U/mL), Pronase E (5 U/mL), and *Streptomyces griseus* protease (1 U/mL), with monitoring periods up to two weeks. In PBS alone, minimal mass reduction was observed, with SF20 and SF20_PEI maintaining about 95% and 96% of their original mass, respectively (Fig. 46a). Lysozyme-mediated degradation proved more pronounced, leaving only 88.65% (SF20) and 89.28% (SF20_PEI) of material intact after one week

(Fig. 46b). Pronase E demonstrated considerably greater catalytic activity, resulting in residual masses of 68.73% for SF20 and 71.34% for SF20_PEI (Fig. 46c). Most strikingly, complete dissolution (~100% mass loss) occurred within just 12 hours when exposed to *Streptomyces griseus* protease (Fig. 46d). These degradation patterns correlate well with phage release profiles, indicating substantial matrix breakdown of both scaffold types in PBS after six days.

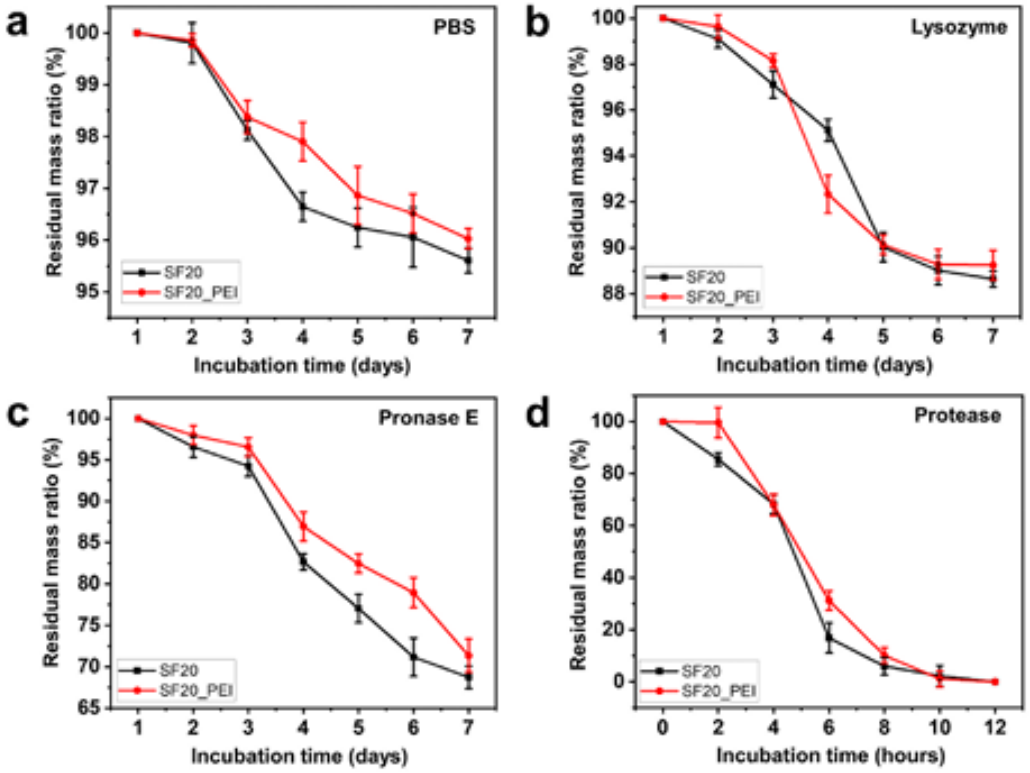

Figure 46 *In vitro* assays of functionalized silk-based scaffolds. (a), *In vitro* degradation profiles of silk fibroin scaffolds in PBS solution (0.01 M) (b), Lysozyme (2 U/ml in PBS solution (c), Pronase E (5 U/ml) (d), protease from Streptomyces griseus (1 U/ml)) in PBS. The data is shown as mean ± s.d.; n = 3 independent experiments

5.5.2.3 Pore morphology

The pore morphology and diameter distribution characteristics of silk fibroin -based composite scaffolds were studied using scanning electron microscopy (SEM).

Micrographs revealed that these scaffolds possessed a fine fibrous structure, constituting a porous architecture composed of a three-dimensional network of loosely arranged pores (Fig. 47). Notably, polymerization with polyethyleneimine (PEI) resulted in a reduction in pore size (Fig. 47 B, D). These fibers were arranged in a network-like pattern, exhibiting diameters ranging from 80 μm to 1000 μm. Regarding pore size distribution, the SF scaffold exhibited the lowest porosity and the most heterogeneous pore sizes (Fig. 47A). In contrast, both SF20-PEI and SFG scaffolds displayed similar, higher porosity levels and more uniform pore sizes. The SFG-PEI scaffold (Fig. 47D) demonstrated the highest porosity; however, due to the increased crosslinking density imparted by PEI, most pores became flattened, leading to a compromised liquid absorption capacity. This observation is consistent with the abovementioned results of water absorption for the scaffolds.

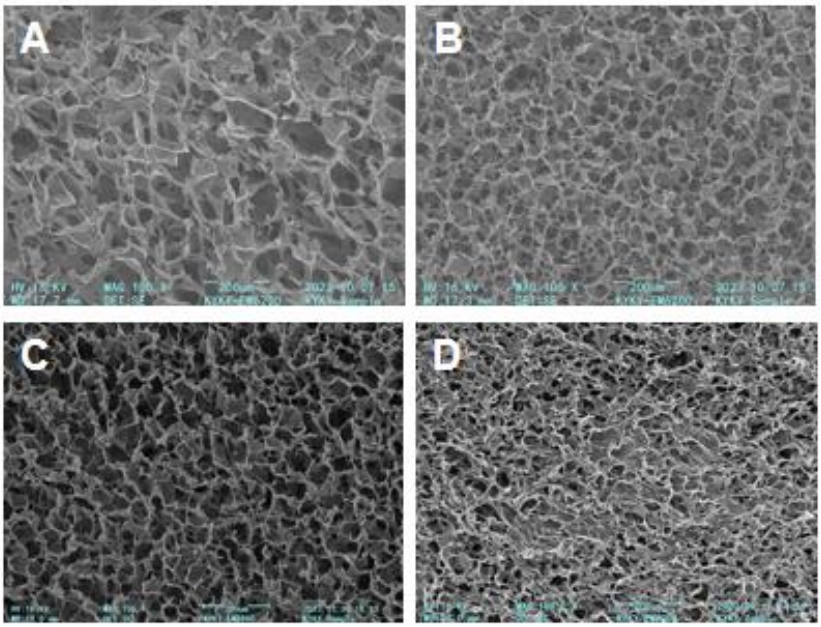

Figure 47 SEM images of scaffolds (A) SF20, (B) SF-PEI, (C) SFG, (D) SFG-PEI, size bar-200um

SEM revealed distinct structural characteristics in the SFGC731 and SFGC735 scaffolds compared to the SF20 scaffold, presumably attributable to the high hydrophilicity of chitosan. Specifically, the SFGC731 scaffold exhibited an irregular undulating morphology (Fig. 48A), while the SFGC735 scaffold displayed an irregular macroporous structure (Fig. 48C). However, following PEI treatment, both SFGC731-PEI (Fig. 48B) and SFGC735-PEI (Fig. 48D) underwent more pronounced structural alterations due to the strong cationic properties of both chitosan and PEI. This resulted in densely packed, relatively flattened architectures with reduced pore diameters.

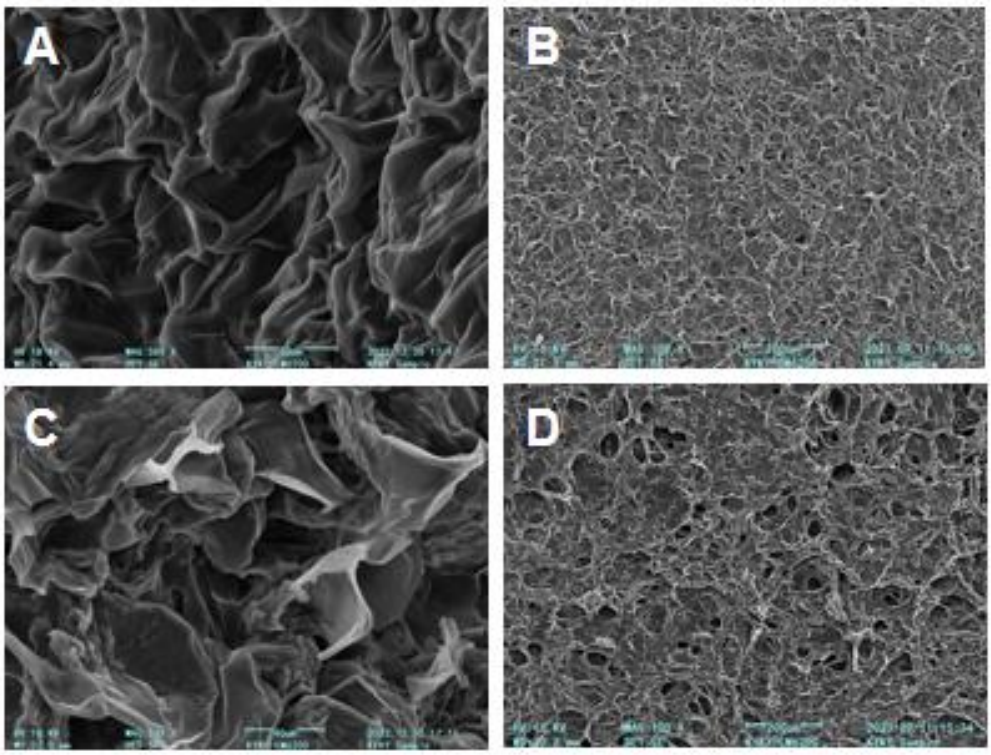

Figure 48 SEM images of scaffolds (A) SFGC731, (B) SFGC731-PEI, (C) SFGC735, (D) SFGC735-PEI, size bar-40um

5.5.2.4 Raman spectroscopic analysis[3]

Raman spectroscopic analysis of the scaffolds (Fig. 49a) revealed characteristic silk fibroin signatures, prominently featuring tyrosine-associated bands. The Fermi resonance doublet at ~830 cm^{-1} and 850 cm^{-1} indicates tyrosine hydrogen bonding states. Notably, the I_{683}/I_{642} ratio reflects tyrosine's hydrogen bonding environment (Fig. 49b). Elevated intensity at 680 cm^{-1} (C-S vibrations) in SF20-PEI-Bs168 and SF20-PEI-AR9 samples suggests residual biological contaminants, given fibroin's minimal sulfur-containing residues. Conformational changes were assessed via the I_{1083}/I_{1003} ratio (Fig. 49c) (C-C oscillations vs. phenylalanine's invariant ring vibration).

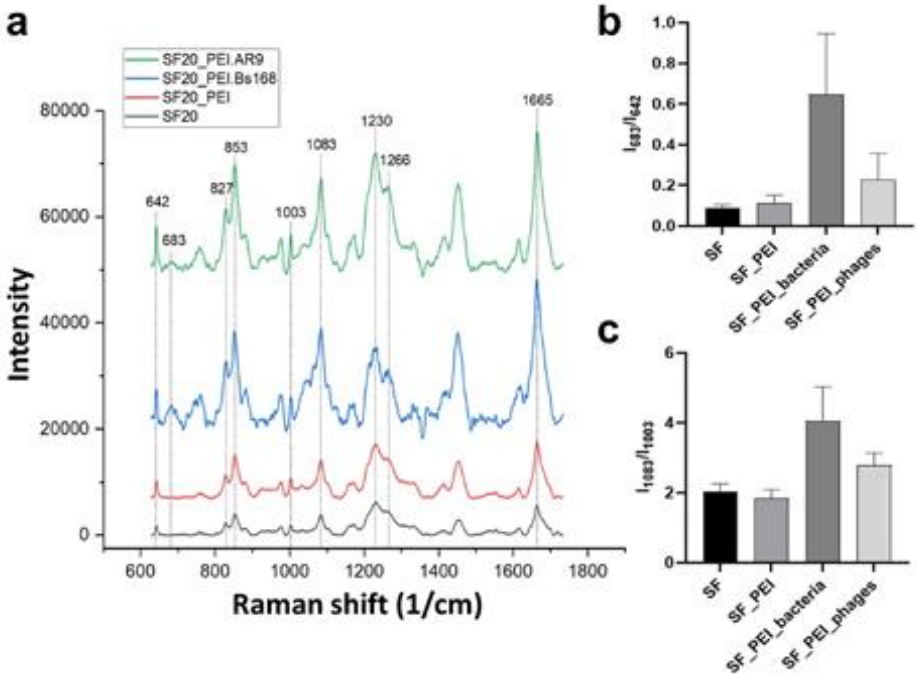

Figure 49 Raman spectra of scaffolds and functional groups characterization, (a), presents the averaged intensity of the Raman spectra, (b). assessed intensity parameters I683/l642, (c). I_{1083}/l_{1003} of Raman spectra. Statistical analysis, Student's test with P value, $p< 0.05$ (Osire*, Wang* et al, 2025).

[3] This work was done with the help of Lu Guojing (SMBU).

Raman analysis confirmed increased β-structure content and altered protein conformations in SF20-PEI-Bs168, attributable to new SF-PEI bond formation. These structural modifications significantly influence scaffold integrity and phage release kinetics, directly impacting antimicrobial functionality.

5.5.3 Functionalizing of SF-scaffolds with bacteriophages

The immobilization of bacteriophages onto SF scaffolds was achieved through cationic PEI crosslinking, leveraging PEI's high positive charge density to interact with negatively charged viral capsid proteins. The polymerization process was conducted in two stages: initial reaction at 25 °C followed by extended incubation at 4 °C for 12 hours to promote comprehensive bond formation, including ionic interactions, covalent linkages, and hydrogen bonding with both SF amino acid residues and phage surface proteins. This PEI-mediated phage stabilization approach establishes a robust platform for creating antimicrobial biomaterials. TEM analysis [4] confirmed predominant interaction between phage capsids and scaffold surfaces (Fig. 50).

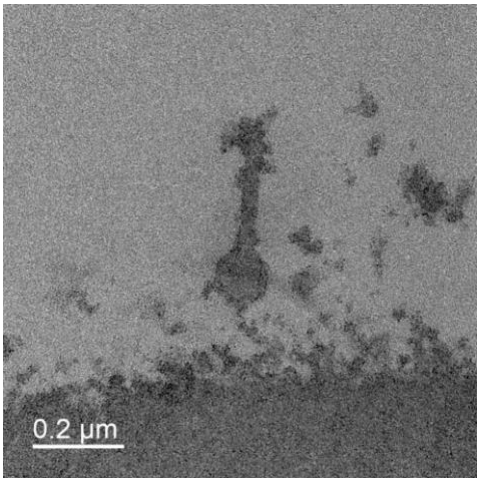

Figure 50 TEM image of phage functionalized SF20 scaffold

[4] This work was done with the help of Ms Zhang Licheng (MSU)

5.5.4 Phage diffusion assay

Next, we tested the possibility of functionalized scaffolds to release bacteriophages over long period of time. Herein, SF20-PEI scaffolds were functionalized with two distinct bacteriophages to comparatively assess their diffusion kinetics in liquid LB medium.

Table 2 Concentration of phages in liquid medium.

Time (Days)	0	3	4	5	6	7	10
AR9/PFU	10^9	$5*10^6$	$2*10^6$	$3*10^6$	$3*10^7$	$4*10^5$	$1*10^6$
PB1/PFU	10^9	$2.4*10^6$	$2.3*10^6$	$3.5*10^6$	10^7	$1.5*10^8$	$3.3*10^8$

As shown in Table 2, despite differences in phage type, both exhibited comparable diffusion rates during days 0–6, which indicating stable diffusion kinetics within the scaffold matrix. Beyond the sixth day, however, phage concentrations diverged significantly. This phenomenon may correlate directly with the degradation of scaffolds, which shown seriously structural destroy after day 6. Furthermore, the different behavior of SF20-AR9 and SF20-PB1 during days 7–10 may be attributed to phage characteristics: AR9 is a giant phage with a large capsid, while PB1 has smaller capsid structure. This differences of capsid dimensions modulates electrostatic interactions between the phage capsids and cationic PEI during scaffold degradation, leading to different diffusion rates in the later diffusion. Moreover, all the diffusion rate is larger than 10^6 PFU within 6 days, which means scaffold with phage can work stable under *vivo* condition.

5.5.5 The cytotoxic effect of PEI functionalized scaffold5

Finally, we tested the cytotoxicity of functionalized scaffolds with eukaryotic cells. Cell viability of NIH/3T3 fibroblasts was evaluated through CCK-8 assays following 24, 48 and 72 h exposure to scaffold extracts. Test groups included both PEI-modified (5% w/v) and unmodified scaffold materials, with complete growth medium serving as the negative control. Quantitative analysis revealed that PEI-functionalization at this concentration showed no cytotoxic effects, as evidenced by comparable metabolic activity across all experimental groups (Fig. 51). Statistical analysis confirmed the absence of significant differences in cellular viability between PEI-treated and untreated scaffolds at all time points examined.

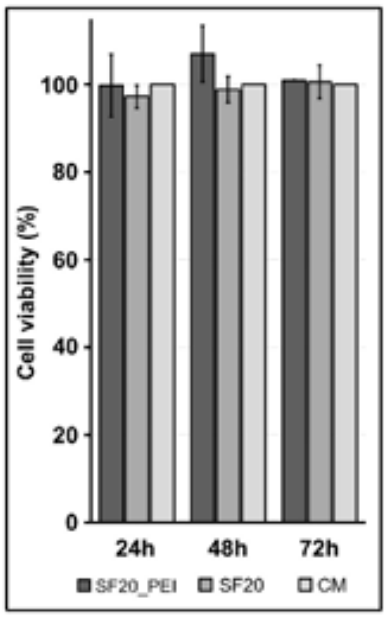

Figure 51 Cytotoxicity assay of PEI functionalized scaffold extracts (SF20_PEI). The viability of NIH/3T3 cells was measured by the CCK-8 assay after incubation with scaffold extracts for 24, 48 and 72 h. The complete medium (CM) was used as a control (Osire*, Wang* et al, 2025).

[5] This work was done with the help of Prof. Anastasia Arkhipova (SMBU)

5.6 Antibacterial functions of scaffolds

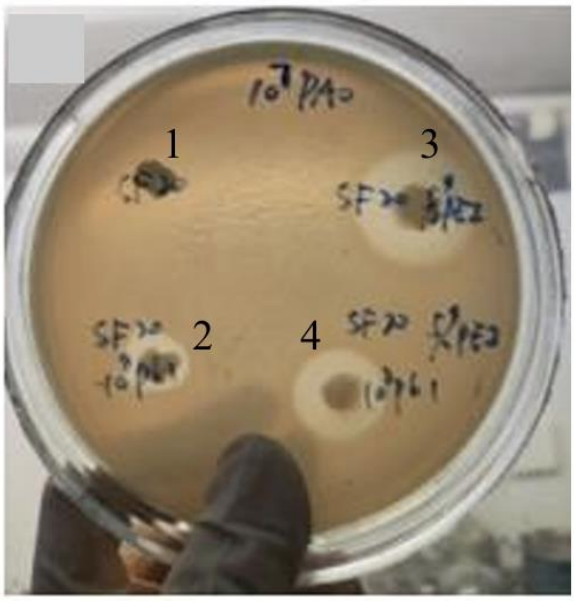

Figure 52 Representative overnight antimicrobial activity for the 1 - SF20, 2 - SF20_PEI and phage functionalized 3 - SF20_PB1 and 4 - SF20_PEI-PB1 scaffolds.

5.6.1 Antimicrobial tests on solid media

To simulate the antibacterial efficacy of scaffolds in early-stage infection scenarios, representative SF20 and SF20-PEI scaffolds were subjected to antimicrobial testing at varying concentrations. As demonstrated in Fig. 52, after overnight incubation (Day 1), the SF20 scaffold without bacteriophages exhibited negligible bacterial growth inhibition zones, whereas phage loaded SF20 scaffolds generated modest inhibition halos. In contrast, SF20-PEI scaffolds displayed significantly larger and distinct inhibition zones, confirming their enhanced potential for preventing initial infection onset. After 3 days of culture, the control SF20 scaffold without phages was completely overgrown by bacteria (data not shown).

Table 3 Inhibition zone diameters (mm) of functionalized scaffolds against *P. aeruginosa* PAO1

SF20-PEI	PAO CFU/ml	10^6	10^7	10^8	10^9
	10^8 PB1	15mm	12/14mm	9.5/14mm	8/10mm
	10^8 PhiKZ	16mm	14/17mm	9/14mm	8/14mm
	Without phage	18mm	16/18mm	9/17mm	6.5/15mm
SF20	Without phage	1mm	0mm	0mm	0mm

The antibacterial efficacy of functionalized silk fibroin scaffolds was systematically evaluated against *P. aeruginosa* PAO1 across bacterial concentrations spanning 10^6 to 10^9CFU/mL. Unmodified SF20 scaffolds lacking bacteriophages demonstrated negligible inhibition ($\leqslant$ 1 mm), confirming their limited inherent antimicrobial activity. In stark contrast, SF20-PEI scaffolds exhibited concentration-dependent inhibition zones, with distinct dual-zone patterns emerging at high bacterial densities (>10^7 CFU/mL). According to table 3, at 10^9 CFU/mL, phage-free SF20-PEI scaffolds generated partial inhibition zones of 6.5 – 15 mm diameter, while those functionalized with 10^8 PFU PB1 or phiKZ phages produced concentric zones: an inner zone of complete clearance (8 – 9.5 mm for PB1; 8 – 9 mm for phiKZ) surrounded by an outer zone of partial inhibition (10 – 14 mm for PB1; 14 – 17 mm for phiKZ). This bifurcation reflects the synergistic yet spatially distinct actions of PEI and phages—the inner sterile zone arises from rapid phage-mediated lysis, while the outer zone stems from sublethal membrane disruption by cationic PEI.

Notably, control experiments with non-PEI scaffolds revealed critical insights: At 10^9 CFU/mL, SF20 scaffolds functionalized with 10^8 PFU phiKZ or PB1 alone generated larger singular inhibition zones (11 mm and 9 mm, respectively) compared to the inner zones of their PEI-containing counterparts (8 – 9.5 mm). From the results, we can see that the modified scaffolds had larger but less clear zone. We suggested this inverse relationship indicates that cationic PEI chains electrostatically "grab" negatively charged phage particles. While this interaction stabilizes phage immobilization, it also restricts phage delivery through the matrix. Thus, phage availability at remotely sites is reduced, representing as smaller complete clear zones with better anti-bacterial activity.

Generally, these findings shown a dynamic interaction between scaffold modification and phages. PEI provides broad-spectrum anti-bacterial activity in low-density infections. Phages deliver targeted lysis but exhibit diffusion constraints when electrostatically bound to PEI. The dual-zone phenomenon uniquely visualizes this mechanism, while the comparative diffusion data highlight the trade-off between phage stabilization and mobility. These results position PEI-phage functionalized scaffolds as controllable systems, that it is necessary to control balances between phage stabilization and mobility requirements.

5.6.2 Antimicrobial tests on semi-agar and liquid media

Beyond conventional agar diffusion assays, the antimicrobial performance of functionalized scaffolds was further validated in simulated physiological environments. In three-dimensional solid matrices—mimicking internal wound sites such as infected bone tissue—SF20-PEI scaffolds functionalized with bacteriophages were embedded

within semi-solid agar inoculated with *P. aeruginosa* PAO1 (10^{10} CFU/mL). After four days of incubation, distinct inhibition zones developed beneath the implanted scaffolds (Fig. 53A), confirming significant radial diffusion of active phages through the matrix. This demonstrates the capacity of phage-functionalized SF20-PEI constructs to exert antibacterial effects in dense, tissue-like environments, supporting their potential application in deep-seated infections.

Conversely, liquid-phase testing revealed temporally stratified efficacy patterns. At 24 hours post-inoculation (Fig. 53B), all samples except non-functionalized SF20 scaffolds maintained optical clarity — indicating potent bacterial suppression. By day 4, sustained antibacterial activity was observed exclusively in SF20-1%PEI (phage-loaded), SF20-5%PEI (phage-free), and SF20-5%PEI (phage-loaded) groups (Fig. 53C). Crucially, only SF20-5%PEI scaffolds co-functionalized with bacteriophages retained complete clarity through day 7 (Fig. 53D). This progressive attenuation highlights a critical divergence from solid-phase results: the synergy between high-concentration PEI (5%) and immobilized phages confers superior durability in fluid environments.

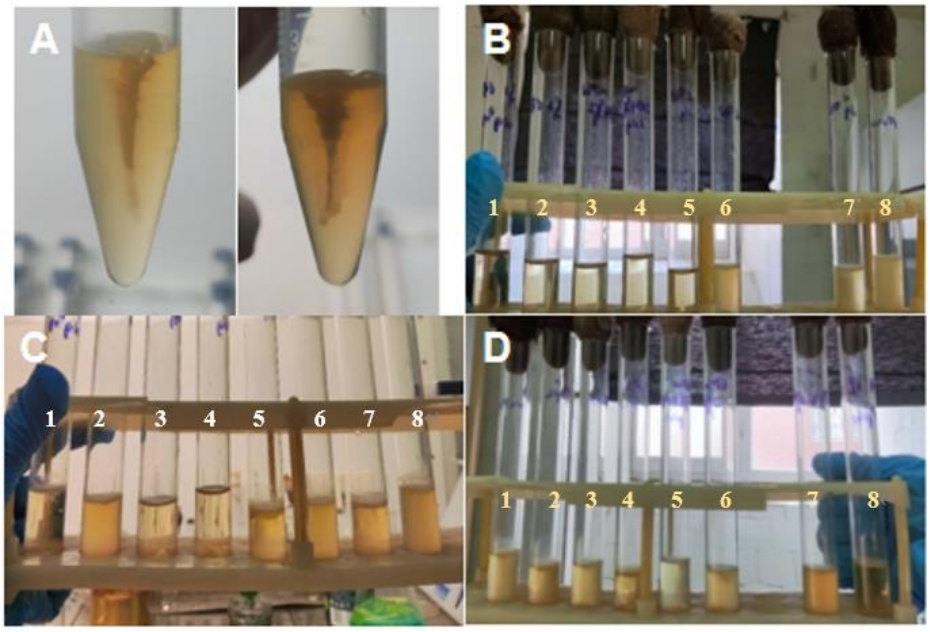

Figure 53 Representing overnight antimicrobial activity of different scaffolds in (A) semi-agar and liquid conditions: (B) after overnight culture; (C) after 4 days; (D) after 7 days. The samples are: 1. SF20-1%PEI-PB1; 2. SF20-1%PEI; 3. SF20-5%PEI; 4. SF20-5%PEI-PB1; 5. SF20-PB1; 6. SF20; 7. Positive control (only bacteria); 8. negative control (only phage without SF20).

The enhanced liquid-phase performance stems from two synergistic mechanisms. First, PEI's cationic chains continuously disrupt bacterial membranes via electrostatic interactions—a process amplified in aqueous media where molecular mobility is higher. Second, the sustained release of electrostatically bound phages from the swelling scaffold (as established in phage diffusion studies) enables iterative infection cycles, dynamically replenishing antibacterial activity. This fluid-mediated release compensates for the diffusion constraints observed in solid agar, where gravitational phage dispersion is physically restricted. Consequently, the SF20-5%PEI-phage system achieves prolonged bactericidal capacity unmatched by either component alone especially in liquid condition.

5.6.3 SEM of antimicrobial tests

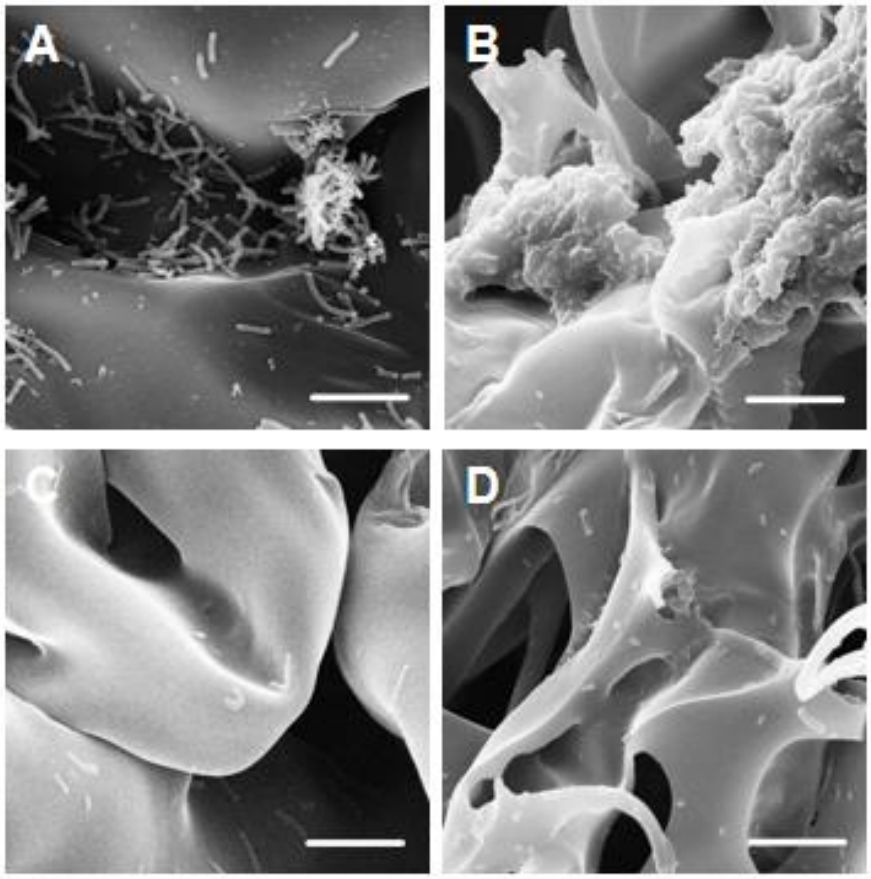

Figure 54 SEM micrographs of the antibacterial effect of (A) SF20, (B) phage functionalized SF20-AR9, (C) SF20-PEI, and (D) SF20-PEI-AR9 scaffolds. Scale Bar – 10 μm;

Scanning electron microscopy provided direct morphological evidence of differential antibacterial activity across functionalized scaffolds. Unmodified SF20 controls exhibited dense colonization by intact bacterial cells (Fig. 54A), confirming minimal antibacterial capacity. In contrast, SF20-PEI surfaces showed sparse bacterial attachment, demonstrating PEI's role in antibacterial function (Fig. 54C). The strongest antibacterial effects were observed on SF20-PEI.AR9 scaffolds (Fig. 54D), which full of cellular debris and fragmented structures. These morphological signatures shown large amount of bacteriophage lysis, and it beyond the activity of PEI-modified sample. Bacterial aggregates were observed in non-polymerized SF20-AR9 scaffolds (Fig. 54B),

the cell were arranged like biofilm. While surface cells within these aggregates showed clear damage, the viability of inside cells remains uncertain. Potentially bacterial defense mechanisms against phage penetration may happen in the absence of PEI-assisted dispersion. These visualized images are corelated with quantitative antibacterial assays, confirming that functionalized scaffold enhances bactericidal performance.

These microstructural observations validate the superior antibacterial functionality achieved through combined PEI modification and phage immobilization. And also provide the morphological correlation to solid inhibition zone and liquid-phase testing results.

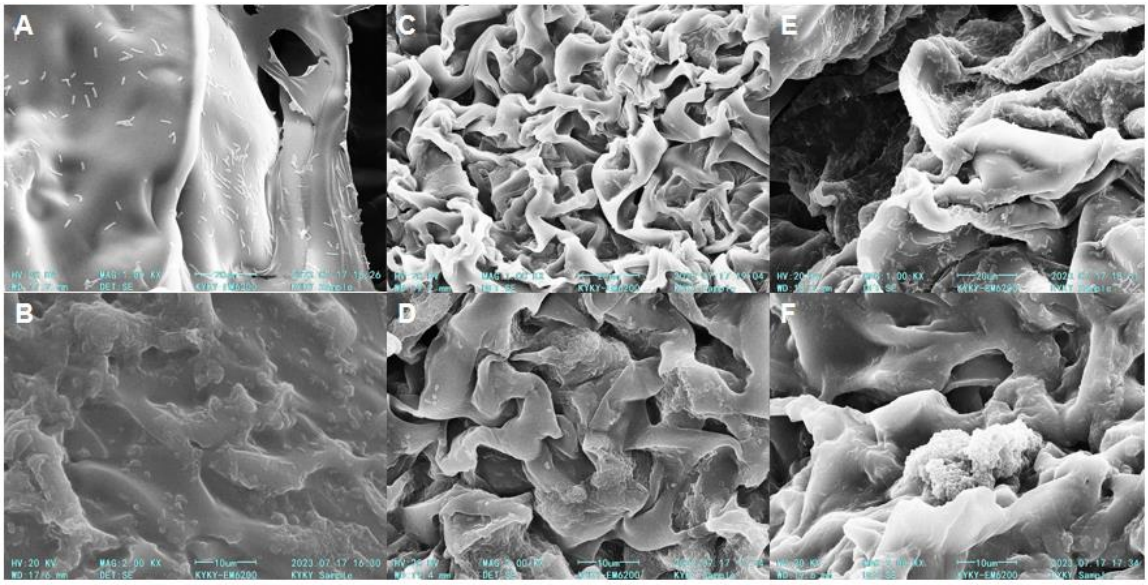

Figure 55 SEM micrographs of different scaffolds before (A, C, E) and after (B, D, F) phage functionalized, A, B - SFG scaffold; C, D - SFGC731 scaffold; E, F - SFGC733 scaffold; Scale Bar A, C, E – 20 μm, B, D, F – 10 μm.

Scanning electron microscopy evaluation of SFG, SFGC731, and SFGC733 scaffolds revealed consistent bacterial colonization patterns in unmodified states (Fig. 55A, C, E). All three scaffold variants exhibited morphologically intact bacterial cells adhering to the surfaces when neither PEI nor bacteriophages were applied. After phage

functionalization, however, these gelatin/chitosan-containing scaffolds displayed the same bacterial aggregation phenomena as observed in SF20 samples (Fig. 55B, D, F). Phage-treated SFG, SFGC731, and SFGC733 scaffold surfaces demonstrated characteristic cluster of bacteria. This result was the same across all scaffolds, which not corelated to whether were modified with gelatin and chitosan or not. We suggest that scaffold with only phage can induce bacterial aggregation without PEI modification.

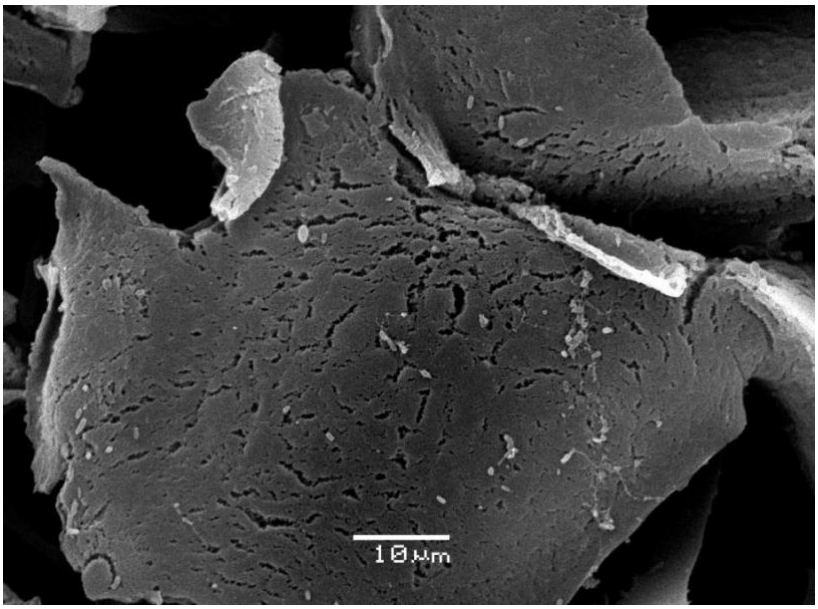

Figure 56 SEM micrographs of SF20-PEI-PB1 scaffold after overnight antimicrobial assay on agar plate. Size bar - 10µm.

Notably, scanning electron microscopy evaluation of SF20-PEI-PB1 scaffolds, which were used after overnight antimicrobial assay on agar plate, revealed large number of bacterial cellular debris adhered to the scaffold matrix (Fig. 56). This morphological evidence of lytic damage is corelated to quantitatively result of inhibition zone measurements, confirming the bactericidal activity. A distinct structural deviation was concurrently observed: these scaffolds exhibited pronounced surface fissuring and internal cracking not detected in pre-test counterparts. This physical compromise suggests

accelerated structural degradation under solid-phase incubation conditions. Our earlier findings demonstrated rapid scaffold degradation in protease environments, indicating susceptibility to enzyme. We propose that bacteriophage-mediated lysis may generate concentrated bacterial lytic enzymes at the scaffold interface, so that lead to the quick scaffold degradation.

This chapter comprehensively evaluates the antibacterial efficacy, functional mechanisms, and structural behavior of functionalized silk fibroin scaffolds across simulated physiological environments. Agar diffusion assays demonstrated potent concentration-dependent antimicrobial activity in SF20-PEI scaffolds, with distinct dual-zone inhibition patterns emerging at high bacterial concentrations (>10^7 CFU/mL): an inner zone of complete phage-mediated clearance (8–9.5 mm) surrounded by an outer zone of PEI-driven partial inhibition (10–17 mm). Control experiments revealed that non-PEI scaffolds functionalized solely with phages produced larger singular inhibition zones (9–11 mm), indicating that cationic PEI restricts phage dispersion through electrostatic sequestration while enhancing localized bactericidal efficacy. SF20-5%PEI functionalized scaffolds demonstrated particular prolonged time in liquid media. It can maintain complete antibacterial function within 7 days, which is significantly outperforming all other samples. Scanning electron microscopy provided morphological validation among different scaffold types. Unmodified controls exhibited dense bacterial aggregation, while PEI-functionalized surfaces showed sparse cell attachment and phage-functionalized scaffolds (SF20-PEI.AR9) displayed large number of cellular debris. The result confirm superior lytic activity of. phage-functionalized scaffolds. SEM of agar-tested SF20-PEI-PB1 scaffolds shown both bacterial debris and structural fissuring,

suggesting degradation in solid media. Collectively, these findings establish scaffolds with PEI-phage functionalization as a controllable strategy for infection treatment biomaterials.

6. Discussion

In the medical field, bacteriophages demonstrate significant capacity to inhibit and disrupt bacterial biofilms on tissues and medical devices. They also eliminate biofilms on implants, as evidenced by phage cocktails [120].

Complementing engineering advances, novel delivery systems enhance therapeutic precision. Wroe et al. [121] developed an injectable hydrogel that encapsulates *Pseudomonas* phages and controls their release kinetics at bone infection sites. Encapsulated phages exhibit superior anti-biofilm efficacy compared to free phages. These innovations highlight how integrating phage engineering with advanced delivery platforms could establish new industrial and clinical paradigms. Nevertheless, several technical and regulatory barriers require resolution before widespread implementation.

While phage therapy demonstrates significant efficacy against biofilm-associated infections, its clinical translation faces several challenges. First, the narrow antibacterial spectrum of phages—though advantageous for precision targeting and microbiome preservation—necessitates careful phage selection in polymicrobial infections. This selection process may impact treatment efficacy and timeliness [122]. Second, bacterial resistance to phages remains incompletely resolved. Although phage-antibiotic combinations (PACs) reduce resistance emergence, evolutionary escape mechanisms persist [123]. Furthermore, administered phages may face rapid clearance by host immune systems through both humoral and cellular pathways [124]. Balancing therapeutic effectiveness with immune evasion thus represents a critical translational challenge. Finally, comprehensive safety evaluations are imperative. Studies indicate

phage therapy may alter neutrophil turnover and function while triggering release of bacterial toxins and superantigens during lysis. These components risk inducing adverse reactions including fever, inflammatory responses, and endotoxic shock [124]. Rigorous assessment of these potential risks remains essential for clinical adoption.

Bacteriophage TaPaz is a lytic phage that uses *A. baumannii* with K47 capsular polysaccharide structure [109] as the host and it belongs to the Myoviruses family, which is characterized by a contractile tail. The bacteriophage TaPaz has an icosahedral head with 830Å long and 780Å wide, and a long tail containing a central tube surrounded by sheath with C6 symmetry. The head-to-tail interface part is formed by portal protein, head-tail adapter, head completion protein and tail terminator protein. The head-to-tail interface part has a specialized portal for DNA entry and exit from icosahedral capsid. A detailed description of the structure of head-to-tail interface part is significant for a full understanding of the bacteriophage TaPaz DNA packaging mechanism.

We solved the structure of head-to-tail interface of bacteriophage TaPaz at 3.18 Å resolution (Fig. 13). We investigated the portal complex structure using a localized reconstruction approach, which involved extracting and refining sub-particles from specific regions. This method not only improved the resolution but also resolved the symmetry mismatch issue. The cryo-EM pipeline—combining symmetry expansion, focused classification, and local refinement—overcame pseudo-icosahedral averaging to resolve asymmetric elements, a strategy is applicable to other complex tailed phages.

2) Giant bacteriophages of the phiKZ lineage are distinguished by their large virions and unique structural features such as an inner body within the capsid [112]. During infection, these phages assemble a proteinaceous shell termed the phage nucleus,

primarily composed of the shell protein, which encloses and shields replicating viral DNA from host defense systems including CRISPR-Cas and restriction-modification enzymes [114]. Previous observations identified round compartments immediately following phiKZ infection [113]. Nevertheless, the origin, molecular composition, and functional role of phiKZ EPI vesicles remained elusive.

We demonstrate that phiKZ EPI vesicles are derived from the bacterial inner membrane, encapsulate both viral DNA and virion-associated RNA polymerase, and facilitate the directed transport of phage DNA to the cell center, where the phage nucleus ultimately assembles. These findings establish a previously unrecognized strategy for genome protection and intracellular trafficking during the earliest stage of phage infection.

3) Here we designed several types of SF-based scaffolds, and characterized them with different method such as swelling rate and SEM. Then we conducted a series assay to test the antimicrobial activity of scaffolds. PEI's cationic chains electrostatically immobilize phages while disrupting bacterial membranes, creating a dual-action system. The degradation-phage release correlation further suggests scaffold materials could be tuned to match infection timelines—e.g., chitosan-SF composites for prolonged urinary tract infection applications.

4) *P. aeruginosa* PAO1 biofilms exhibited architecturally complex pellicles at air-liquid interfaces, characterized by densely packed cellular matrices. We show that environmental conditions profoundly modulated therapeutic efficacy. Acidic environments (saline/PBS, pH~5.5) stimulated potassium-dependent EPS overproduction that restricted phage diffusion, whereas neutral SM buffer (pH 7.0) suppressed polysaccharide synthesis through altered bacterial physiology, enhancing phage

accessibility. Such spatiotemporal heterogeneity confirms that microenvironmental conditions must be integrated into therapeutic planning.

5) This comprehensive analysis of four *P. aeruginosa* clinical isolates reveals profound strain-specific heterogeneity in biofilm architecture and phage susceptibility. Phenotypic variations were evident through differential pyocyanin production, with Ur14 and Lu3 exhibiting intense green pigmentation indicative of robust redox activity. Biofilm structural characteristics diverged significantly: Ur1 and Lu9 formed thick, high-viscosity biofilms with loose cellular arrangements and low elastic recovery, while Ur14 and Lu3 developed thinner yet mechanically rigid architectures characterized by densely packed cell. These inherent structural properties governed phage accessibility and therapeutic efficacy.

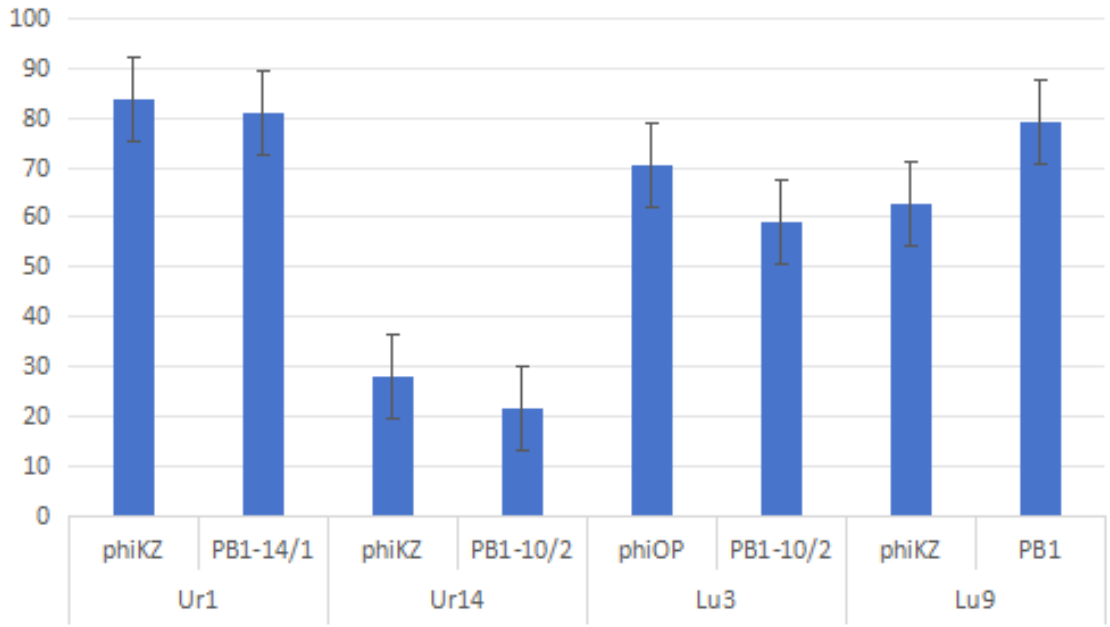

Figure 57 The percentage of Ur and Lu biofilms destruction by phiKZ/PB1-like phages.

Phage susceptibility assays demonstrated strain-dependent eradication patterns despite consistent lytic efficiency in plaque formation. Quantitative biofilm clearance analysis revealed a spectrum of responses (Fig. 57): Ur1 showed exceptional vulnerability

(>80% clearance), Lu3 and Lu9 exhibited intermediate susceptibility (>60%), while Ur14 displayed profound resistance (<35% clearance across all phages). Scanning electron microscopy further illuminated divergent defensive strategies - while all strains produced fibrillar extracellular matrices post-phage exposure, Ur14 generated thick amorphous EPS barriers that physically restricted phage diffusion and protected subsurface cell clusters.

These findings establish a paradigm for precision phage therapy: personalized phage selection based on strain-specific biofilm characteristics can achieve clinically relevant eradication in most MDR isolates. For exceptional cases like Ur14, integrated approaches combining phage cocktails with EPS-degrading adjuvants represent promising investigative pathways. Future research should delineate the genetic basis of hyper-resistance through transcriptomic profiling while exploring biofilm-phage dynamics in physiologically relevant microenvironments to optimize clinical translation.

Biofilm eradication efficacy hinges on architectural vulnerability. Loosely structured biofilms (e.g., *B. subtilis* Day 5, *P. aeruginosa* Ur1) permitted rapid phage infiltration andlysis, whereas dense matrices (e.g., Ur14) employed EPS overproduction as a shield. Ur14's resilience—despite multi-phage cocktails—highlights limitations of monotherapy against hyper-biofilm formers. Future work may integrate EPS-degrading enzymes (e.g., DNase, alginate lyase) with phages, which could breach these barriers. Furthermore, the stark efficacy differences among clinical isolates underscore the need for personalized phage selection based on biofilm phenotyping.

Future work should explore *in vivo* scaffold performance in infection models, particularly regarding immune compatibility. While PEI-functionalized scaffolds showed

no cytotoxicity (NIH/3T3 viability >95%), long-term inflammatory responses warrant investigation. In conclusion, this study integrates phage structural biology with functional biomaterial engineering, revealing how portal complex architecture enables DNA translocation and how scaffold-tailored phage delivery can overcome bacterial resistance. The interplay between biofilm matrix and phage efficacy emphasizes the need for precision approaches in translating phage therapy to clinical practice.

7. Findings

An integrated approach, including modern biophysical methods, made it possible to determine the nature of the interaction of bacteriophages with bacterial biofilms at different stages. As a result, a molecular model of the portal complex of *A. baumannii* bacteriophage TaPaz was built, and the role of individual amino acids in the interaction with the adapter protein, ensuring the mechanical stability of the "head-tail" connection, was revealed. Analysis of the electrostatic surface potential of the portal established the presence of a positively charged region in the upper part and a negatively charged region in the area of interaction with the adapter protein. Such structural features of the portal provide the formation of an extensive interface for interaction with negatively charged DNA and prevent premature DNA ejection during infection.

The study of EPIV showed that when, at the initial stage of infection, phiKZ injects its DNA and some proteins into the host cell, a lipid bilayer, presumably originating from the inner cell membrane, encapsulates them, forming vesicles. This encapsulation protects viral components from bacterial defense mechanisms, facilitating phage DNA transcription.

Work was carried out to select conditions for obtaining three-dimensional porous substrates based on silk fibroin. This biomaterial is non-toxic, characterized by high biocompatibility and biodegradability. Various biophysical parameters of the obtained substrates were investigated: swelling rate, degradation under the action of enzymes, pore morphology, changes in the secondary structure of protein polymers in the samples.

Polymerization with PEI led to a decrease in pore size and β-sheet content in silk

fibroin. This apparently results in a less organized fibroin structure and the appearance of new charged sites that promote better phage attachment. Indeed, the diffusion rate of bacteriophages from the substrate material was 10^6 CFU/ml over 6 days, meaning that phage-functionalized substrates can deliver the phage to the infection site and release it over an extended period in liquid media, confirming their potential for preventing primary infection.

We studied clinical isolates of *P. aeruginosa* with multiple antibiotic resistance and varying biofilm-forming abilities. The tested bacteriophages of 2 genera (PhiKZvirus and Pbunavirus) of the class Caudoviricetes affected biofilms with varying intensity; 6 phages destroyed over 50% of the biofilm, and 2 phages — over 75% of the biofilm. In most cases, the ability of a phage to destroy biofilms was directly dependent on the multiplicity of infection (MOI). To achieve the most complete biofilm destruction, individual phage selection for each bacterial strain is required. Assessing the ability to destroy bacterial biofilms is an additional criterion for selecting phages for personalized PT and allows considering bacteriophages as effective agents for combating biofilms.

Conclusions

1. High-resolution cryo-EM (3.18 Å) revealed the C12-symmetric architecture of the protein complex in the head-tail region of A. baumannii phage TaPaz. The distribution of the electrostatic surface potential of portal amino acids revealed extensive areas with negative potential inside the portal channel, presumably controlling DNA position both during head filling and during infection.

2. The early stages of phiKZ phage infection are characterized by the formation

of EPIV using the inner membrane of the host bacterium. The vesicles protect the phage DNA from bacterial nucleases until the formation of the "phage nucleus".

3. The effectiveness of phages against *P. aeruginosa* biofilms depends on their structure and environmental pH. Loose biofilms were quickly destroyed by bacteriophages, whereas dense structures exhibited resistance, associated with the presence of a thick protective layer of exopolysaccharides (EPS). Phage PB1 exhibits the greatest antimicrobial activity at neutral pH.

4. Substrates based on silk fibroin (SF), functionalized with PEI and bacteriophages, demonstrated controlled long-term phage release (>10^6 CFU/ml over 6 days) and increased structural stability, and cytotoxicity assays confirmed substrate biocompatibility (NIH/3T3 viability >95%); they provided sustained bacterial suppression in liquid media for 6 days and demonstrated stable inhibition of bacterial growth in agar media, significantly outperforming non-functionalized substrates in effectiveness.

8. Acknowledgments

I would like to express my deepest gratitude to all those who have contributed to this doctoral research. First and foremost, I am deeply grateful to my supervisor, Professor Olga Sokolova. Her excellent guidance and unwavering support have been instrumental throughout this journey. Her insightful mentorship not only shaped the scientific direction of my work but also provided me constant encouragement during challenging moments. Beyond academic supervision, Professor Sokolova's care for both my personal and professional development has been truly encouraging me. What's more, Dr. M. V. Bourkaltseva provided valuable guidance on scaffold antimicrobial testing protocols and phage-biofilm assays, they are greatly enhanced the reliability of our work. Also, I'm really appreciate for the support and help from I.I. Mechnikov Research Institute and bacteriophage genetics laboratory. This work was supported by RSF (24-44-02003) and part - by Shenzhen Municipal Government and Shenzhen MSU-BIT University.

The successful execution of this research would not have been possible without the generous contributions of several collaborators and institutions. I am particularly grateful to Professor Liu Zheng and his team at the Chinese University of Hong Kong (Shenzhen) for their expertise in cryo-EM specimen preparation and data collection. Special thanks are due to Dr. Konstantin Miroshnikov from the Institute of Bioorganic Chemistry RAS in Moscow for providing the purified TaPaz phage and Dr Maria Yakunina from Peter the Great St.Petersburg Polytechnic University for providing the purified AR9 phage. The various *P. aeruginosa* strains and phages from the Laboratory of Bacteriophage Genetics at the I.I. Mechnikov Research Institute were invaluable resources that significantly

enhanced the scope of this work.

I extend my sincere appreciation to the many colleagues who provided specialized technical assistance. Mr. Andrey Moiseenko's expertise in atomic model building and TEM imaging was crucial for our structural analyses. Professor Anastacia Arkhipova's guidance in scaffold design and cytotoxicity testing greatly strengthened our biomaterials approach. I am thankful to Zhang Licheng for her TEM sample preparation, Lu Guojing for conducting Raman spectroscopy experiments, and A. I. Burykin for biofilm CV staining techniques. Dr. T. Osire's expert on scaffold design and performance evaluation significantly improved the quality of our experimental work. I sincerely thank to Prof. Andrey Letarov and his team for suggestions and corrections for my thesis. Many thanks to Prof. Anton Bonartsev and his team for opinions on my thesis.

Finally, I acknowledge the less visible but equally important support from family, friends, and fellow researchers who provided encouragement throughout this demanding yet rewarding process. This thesis represents not just individual effort but the collective contribution of a supportive scientific community.

9. List of publications

1. Antonova D, Nichiporenko A, Sobinina M, **Wang Y**, Vishnyakov IE, Moiseenko A, Kurdyumova I, Chesnokov YM, Stepanchikova E, Bourkaltseva M, Samygina VR, Khodorkovskii M, Sokolova OS, Yakunina MV. Genomic transfer via membrane vesicle: a strategy of giant phage phiKZ for early infection / Antonova D // J Virol. — 2024. — Vol. 98. — P. e00205-24.

2. Osire T, **Wang Y**, Burtseva O, Sokolova O. Structural Heterogeneity and Diversity of *Bacillus subtilis* 168 Biofilms under Different Conditions / Osire T // Moscow University Biological Sciences Bulletin. — 2024. — Vol. 78. — P. S40-S44.

3. **Wang Y**, Bourkaltseva MV, Burykin AI, Sokolova OS. Study of the Effect of Virulent Bacteriophages on *Pseudomonas aeruginosa* PAO1 Bacterial Biofilms by Scanning Electron Microscopy / Wang Y // Microbiology. — 2025. — Vol. 94. — P. 282-285.

4. Osire T*, **Wang Y***, Popova L*, et al. Silk fibroin-based scaffolds functionalized with Bacteriophages exhibit substantial Antimicrobial Potential / Osire T // Materials Chemistry and Physics. — 2025. — Vol. 339. — P. 130650.

* Authors contributed equally to this work.

10. References

1. Tacconelli E. Linking infection control to clinical management of infections to overcome antimicrobial resistance / Tacconelli E // J Hosp Infect. — 2021. — Vol. 114. — P. 1-9.

2. Nathwani D, Raman G, Sulham K, et al. Clinical and economic consequences of hospital-acquired resistant and multidrug-resistant *Pseudomonas aeruginosa* infections: a systematic review and meta-analysis / Nathwani D // Antimicrob Resist Infect Control. — 2014. — Vol. 3(1). — P. 32.

3. Chibeu A, Lingohr EJ, Masson L, et al. Bacteriophages with the ability to degrade uropathogenic *Escherichia coli* biofilms / Chibeu A // Viruses. — 2012. — Vol. 4(4). — P. 471-487.

4. Aleshkin AV, Rubalskii EO, Volozhantsev NV, et al. A small-scale experiment of using phage-based probiotic dietary supplement for prevention of *E. coli* traveler's diarrhea / Aleshkin AV // Bacteriophage. — 2015. — Vol. 5(3). — P. e1074329.

5. Ackermann HW. Tailed bacteriophages: the order caudovirales / Ackermann HW // Adv Virus Res. — 1998. — Vol. 51. — P. 135-201.

6. Borcan AM, Rotaru E, Caravia LG, et al. Trends in Antimicrobial Resistance of *Acinetobacter baumannii* and *Pseudomonas aeruginosa* from Bloodstream Infections: An Eight-Year Study in a Romanian Tertiary Hospital / Borcan AM // Pharmaceuticals (Basel). — 2025. — Vol. 18(7). — P. 948.

7. Arnaouteli S, Bamford NC, Stanley-Wall NR, et al. *Bacillus subtilis* biofilm formation and social interactions / Arnaouteli S // Nat Rev Microbiol. — 2021. — Vol. 19. — P. 600-614.

8. Hibstu Z, Belew H, Akelew Y, et al. Phage Therapy: A Different Approach to Fight Bacterial Infections / Hibstu Z // Biologics. — 2022. — Vol. 16. — P. 173-186.

9. Timoshina OY, Shneider MM, Evseev PV, et al. Novel *Acinetobacter baumannii* Bacteriophage Aristophanes Encoding Structural Polysaccharide Deacetylase / Timoshina OY // Viruses. — 2021. — Vol. 13(9). — P. 1688.

10. Nang SC, Lin YW, Petrovic Fabijan A, et al. Pharmacokinetics/pharmacodynamics of phage therapy: a major hurdle to clinical translation / Nang SC // Clin Microbiol Infect. — 2023. — Vol. 29(6). — P. 702-709.

11. Luong T, Salabarria AC, Roach DR. Phage Therapy in the Resistance Era: Where Do We Stand and Where Are We Going? / Luong T // Clin Ther. — 2020. — Vol. 42(9). — P. 1659-1680.

12. Bichet MC, Patwa R, Barr JJ. Protocols for studying bacteriophage interactions with in vitro epithelial cell layers / Bichet MC // STAR Protoc. — 2021. — Vol. 2(3). — P. 100697.

13. Mendoza SD, Nieweglowska ES, Govindarajan S, et al. *A bacteriophage* nucleus-like compartment shields DNA from CRISPR nucleases / Mendoza SD // Nature. — 2020. — Vol. 577(7789). — P. 244-248.

14. Febvre HP, Rao S, Gindin M, et al. PHAGE Study: Effects of Supplemental Bacteriophage Intake on Inflammation and Gut Microbiota in Healthy Adults / Febvre HP // Nutrients. — 2019. — Vol. 11(3). — P. 666.

15. Torres-Barceló C. Phage Therapy Faces Evolutionary Challenges / Torres-Barceló C // Viruses. — 2018. — Vol. 10(6). — P. 323.

16. Richter Ł, Księżarczyk K, Paszkowska K, et al. Adsorption of bacteriophages on

polypropylene labware affects the reproducibility of phage research / Richter Ł // Sci Rep. — 2021. — Vol. 11(1). — P. 7387.

17. Mirghani R, Saba T, Khaliq H, et al. Biofilms: Formation, drug resistance and alternatives to conventional approaches / Mirghani R // AIMS Microbiol. — 2022. — Vol. 8(3). — P. 239-277.

18. Farooq U, Ullah MW, Yang Q, et al. High-density phage particles immobilization in surface-modified bacterial cellulose for ultra-sensitive and selective electrochemical detection of *Staphylococcus aureus* / Farooq U // Biosens Bioelectron. — 2020. — Vol. 157. — P. 112163.

19. Mojtabavi M, Greive SJ, Antson AA, et al. High-Voltage Biomolecular Sensing Using a Bacteriophage Portal Protein Covalently Immobilized within a Solid-State Nanopore / Mojtabavi M // J Am Chem Soc. — 2022. — Vol. 144(49). — P. 22540-22548.

20. Ayala R, Moiseenko AV, Chen TH, et al. Nearly complete structure of bacteriophage DT57C reveals architecture of head-to-tail interface and lateral tail fibers / Ayala R // Nat Commun. — 2023. — Vol. 14(1). — P. 8205.

21. Rao VB, Fokine A, Fang Q. The remarkable viral portal vertex: structure and a plausible model for mechanism / Rao VB // Curr Opin Virol. — 2021. — Vol. 51. — P. 65-73.

22. Garcia SN, Osburn BI, Cullor JS. A one health perspective on dairy production and dairy food safety / Garcia SN // One Health. — 2019. — Vol. 7. — P. 100086.

23. Collaborators AR. Global burden of bacterial antimicrobial resistance in 2019: a systematic analysis / Collaborators AR // The Lancet. — 2022. — Vol. 399(10325).

— P. 629-655.

24. Collaborators GAAR. Global mortality associated with 33 bacterial pathogens in 2019: a systematic analysis for the Global Burden of Disease Study 2019 / Collaborators GAAR // The Lancet. — 2022. — Vol. 400(10369). — P. 2221-2248.

25. Hatfull GF, Dedrick RM, Schooley RT. Phage therapy for antibiotic-resistant bacterial infections / Hatfull GF // Annual Review of Medicine. — 2022. — Vol. 73. — P. 197-211.

26. Reardon S. Phage therapy gets revitalized / Reardon S // Nature. — 2014. — Vol. 510(7503). — P. 15-16.

27. Dion MB, Oechslin F, Moineau S. Phage diversity, genomics and phylogeny / Dion MB // Nature Reviews Microbiology. — 2020. — Vol. 18(3). — P. 125-138.

28. Pye HV, Krishnamurthi R, Cook R, et al. Phage diversity in One Health / Pye HV // Essays in Biochemistry. — 2024. — Vol. 68(5). — P. 607-619.

29. Thacker PD. Set a microbe to kill a microbe: drug resistance renews interest in phage therapy / Thacker PD // JAMA. — 2003. — Vol. 290(24). — P. 3183-3185.

30. Ackermann HW. Phage classification and characterization / Ackermann HW // Methods Mol Biol. — 2009. — Vol. 501. — P. 127-140.

31. Summers WC. Bacteriophage therapy / Summers WC // Annual Review of Microbiology. — 2001. — Vol. 55. — P. 437-451.

32. Diallo K, Dublanchet A. A century of clinical use of phages: a literature review / Diallo K // Antibiotics. — 2023. — Vol. 12(4). — P. 751.

33. Cong C, Li JB, Wang LL, et al. Research on the early historical literature of bacteriophages in China / Cong C // World Notes on Antibiotics. — 2023. — Vol.

44(2). — P. 73-82.

34. Cook R, Brown N, Redgwell T, et al. Infrastructure for a PHAge Reference Database: Identification of large-scale biases in the current collection of cultured phage genomes / Cook R // Phage(New Rochelle). — 2021. — Vol. 2(4). — P. 214-223.

35. Camargo AP, Nayfach S, Chen IA, et al. IMG/VR v4: an expanded database of uncultivated virus genomes within a framework of extensive functional, taxonomic, and ecological metadata / Camargo AP // Nucleic Acids Research. — 2023. — Vol. 51(D1). — P. D733-D743.

36. Weinheimer AR, Aylward FO. Infection strategy and biogeography distinguish cosmopolitan groups of marine jumbo bacteriophages / Weinheimer AR // ISME. — 2022. — Vol. 16(6). — P. 1657-1667.

37. Ma B, Wang Y, Zhao K, et al. Biogeographic patterns and drivers of soil viromes / Ma B // Nature Ecology & Evolution. — 2024. — Vol. 8(4). — P. 717-728.

38. Adriaenssens EM, Farkas K, McDonald JE, et al. Tracing the fate of wastewater viruses reveals catchment-scale virome diversity and connectivity / Adriaenssens EM // Water Research. — 2021. — Vol. 203. — P. 117568.

39. Zhao L, Shi Y, Lau HC, et al. Uncovering 1058 novel human enteric DNA viruses through deep long-read third-generation sequencing and their clinical impact / Zhao L // Gastroenterology. — 2022. — Vol. 163(3). — P. 699-711.

40. Wagh RV, Priyadarshi R, Rhim JW. Novel Bacteriophage-Based Food Packaging: An Innovative Food Safety Approach / Wagh RV // Coatings. — 2023. — Vol. 13(3). — P. 609.

41. Leiman PG, Shneider MM. Contractile tail machines of bacteriophages / Leiman PG // Adv Exp Med Biol. — 2012. — Vol. 726. — P. 93-114.

42. Fokine A, Rossmann MG. Molecular architecture of tailed double-stranded DNA phages / Fokine A // Bacteriophage. — 2014. — Vol. 4(1). — P. e28281.

43. Ge X, Wang J. Structural mechanism of bacteriophage lambda tail's interaction with the bacterial receptor / Ge X // Nat Commun. — 2024. — Vol. 15. — P. 4185.

44. Taylor MW. The Discovery of Bacteriophage and the d'Herelle Controversy / Taylor MW // Viruses and Man: A History of Interactions. — 2014. — P. 53-61.

45. Fruciano DE, Bourne S. Phage as an antimicrobial agent: d'Herelle's heretical theories and their role in the decline of phage prophylaxis in the West / Fruciano DE // Can J Infect Dis Med Microbiol. — 2007. — Vol. 18(1). — P. 19-26.

46. Kutateladze M. Experience of the Eliava Institute in bacteriophage therapy / Kutateladze M // Virol. Sin. — 2015. — Vol. 30. — P. 80-81.

47. Tang KWK, Millar BC, Moore JE. Antimicrobial Resistance (AMR) / Tang KWK // Br J Biomed Sci. — 2023. — Vol. 80. — P. 11387.

48. Sawa T, Moriyama K, Kinoshita M. Current status of bacteriophage therapy for severe bacterial infections / Sawa T // j intensive care. — 2024. — Vol. 12. — P. 44.

49. Palma M, Qi B. Advancing Phage Therapy: A Comprehensive Review of the Safety, Efficacy, and Future Prospects for the Targeted Treatment of Bacterial Infections / Palma M // Infect Dis Rep. — 2024. — Vol. 16(6). — P. 1127-1181.

50. García-Cruz JC, Huelgas-Méndez D, Jiménez-Zúñiga JS, et al. Myriad applications of bacteriophages beyond phage therapy / García-Cruz JC // PeerJ. — 2023. — Vol. 11. — P. e15272.

51. Perera MN, Abuladze T, Li M, et al. Bacteriophage cocktail significantly reduces or eliminates *Listeria monocytogenes* contamination on lettuce, apples, cheese, smoked salmon and frozen foods / Perera MN // Food Microbiology. — 2015. — Vol. 52. — P. 42-48.

52. Kawacka I, Olejnik-Schmidt A, Schmidt M, et al. Effectiveness of phage-based inhibition of *Listeria monocytogenes* in food products and food processing environments / Kawacka I // Microorganisms. — 2020. — Vol. 8(11). — P. 1764.

53. EFSA Panel on Biological Hazards(BIOHAZ). Evaluation of the safety and efficacy of Listex™ P100 for reduction of pathogens on different ready-to-eat (RTE) food products / EFSA Panel on Biological Hazards(BIOHAZ) // EFSA Journal. — 2016. — Vol. 14(8). — P. e04565.

54. Everhart E, Carson S, Atkinson K, et al. Commercial bacteriophage preparations for the control of *Listeria monocytogenes* and Shiga toxin-producing *Escherichia coli* in raw and pasteurized milk / Everhart E // Food Microbiology. — 2025. — Vol. 125. — P. 104652.

55. Acosta A, Tirkaso W, Nicolli F, et al. The future of antibiotic use in livestock / Acosta A // Nat Commun. — 2025. — Vol. 16(1). — P. 2469.

56. Strathdee SA, Hatfull GF, Mutalik VK, et al. Phage therapy: From biological mechanisms to future directions / Strathdee SA // Cell. — 2023. — Vol. 186(1). — P. 17-31.

57. Furfaro LL, Payne MS, Chang BJ. Bacteriophage Therapy: Clinical Trials and Regulatory Hurdles / Furfaro LL // Front Cell Infect Microbiol. — 2018. — Vol. 8. — P. 376.

58. Chopra H, Islam MA, Sharun K, et al. Recent advances in the treatment of biofilms induced surgical site infections / Chopra H // International Journal of Surgery. — 2023. — Vol. 109(1). — P. 65-67.

59. Hrynyshyn A, Simões M, Borges A. Biofilms in surgical site infections: recent advances and novel prevention and eradication strategies / Hrynyshyn A // Antibiotics. — 2022. — Vol. 11(1). — P. 69.

60. Leitner L, Ujmajuridze A, Chanishvili N, et al. Intravesical bacteriophages for treating urinary tract infections in patients undergoing transurethral resection of the prostate: a randomised, placebo-controlled, double-blind clinical trial / Leitner L // The Lancet Infectious Diseases. — 2021. — Vol. 21(3). — P. 427-436.

61. Nadareishvili L, Hoyle N, Nakaidze N, et al. Bacteriophage therapy as a potential management option for surgical wound infections / Nadareishvili L // Phage (New Rochelle). — 2020. — Vol. 1(3). — P. 158-165.

62. Tkhilaishvili T, Winkler T, Müller M, et al. Bacteriophages as adjuvant to antibiotics for the treatment of periprosthetic joint infection caused by multidrug-resistant *Pseudomonas aeruginosa* / Tkhilaishvili T // Antimicrobial Agents and Chemotherapy. — 2019. — Vol. 64(1). — P. e00924-19.

63. Bhartiya SK, Prasad R, Sharma S, et al. Biological therapy on infected traumatic wounds: a case-control study / Bhartiya SK // The International Journal of Lower Extremity Wounds. — 2024. — Vol. 23(4). — P. 504-512.

64. Racenis K, Rezevska D, Madelane M, et al. Use of phage cocktail BFC 1.10 in combination with ceftazidime-avibactam in the treatment of multidrug-resistant *Pseudomonas aeruginosa* femur osteomyelitis---a case report / Racenis K // Frontiers

in Medicine. — 2022. — Vol. 9. — P. 851310.

65. Church D, Elsayed S, Reid O, et al. Burn wound infections / Church D // Clinical Microbiology Reviews. — 2006. — Vol. 19(2). — P. 403-434.

66. Azzopardi EA, Azzopardi E, Camilleri L, et al. Gram negative wound infection in hospitalised adult burn patients: systematic review and metanalysis / Azzopardi EA // PLoS One. — 2014. — Vol. 9(4). — P. e95042.

67. Young MJ, Hall LML, Merabishvilli M, et al. Phage therapy for diabetic foot infection: a case series / Young MJ // Clinical Therapeutics. — 2023. — Vol. 45(8). — P. 797-801.

68. Mohamed WF, Askora AA, Mahdy MMH, et al. Isolation and characterization of bacteriophages active against *Pseudomonas aeruginosa* strains isolated from diabetic foot infections / Mohamed WF // Archives of Razi Institute. — 2022. — Vol. 77(6). — P. 2187-2200.

69. Liu ZH, Liang Y, Liu D, et al. Dispersion: a new perspective for eradicating bacterial biofilm / Liu ZH // Acta Microbiologica Sinica. — 2023. — Vol. 63(12). — P. 4451-4466.

70. Yan J, Bassler BL. Surviving as a community: antibiotic tolerance and persistence in bacterial biofilms / Yan J // Cell Host & Microbe. — 2019. — Vol. 26(1). — P. 15-21.

71. Srivastava A, Verma N, Kumar V, et al. Biofilm inhibition/eradication: exploring strategies and confronting challenges in combatting biofilm / Srivastava A // Archives of Microbiology. — 2024. — Vol. 206(5). — P. 212.

72. Ban-Cucerzan A, Imre K, Morar A, et al. Persistent Threats: A Comprehensive

Review of Biofilm Formation, Control, and Economic Implications in Food Processing Environments / Ban-Cucerzan A // Microorganisms. — 2025. — Vol. 13(8). — P. 1805.

73. Di Domenico EG, Oliva A, Guembe M. The current knowledge on the pathogenesis of tissue and medical device-related biofilm infections / Di Domenico EG // Microorganisms. — 2022. — Vol. 10(7). — P. 1259.

74. Gholizadeh O, Ghaleh HEG, Tat M, et al. The potential use of bacteriophages as antibacterial agents against *Klebsiella pneumoniae* / Gholizadeh O // Virol J. — 2024. — Vol. 21(1). — P. 191.

75. Wang Y, Dai J, Wang X, et al. Mechanisms of interactions between bacteria and bacteriophage mediate by quorum sensing systems / Wang Y // Appl Microbiol Biotechnol. — 2022. — Vol. 106. — P. 2299-2310.

76. Fernandes S, São-José C. Enzymes and Mechanisms Employed by Tailed Bacteriophages to Breach the Bacterial Cell Barriers / Fernandes S // Viruses. — 2018. — Vol. 10(8). — P. 396.

77. Chang C, Yu X, Guo W, et al. Bacteriophage-mediated control of biofilm: a promising new dawn for the future / Chang C // Frontiers in Microbiology. — 2022. — Vol. 13. — P. 825828.

78. Sharma U, Vipra A, Channabasappa S. Phage-derived lysins as potential agents for eradicating biofilms and persisters / Sharma U // Drug Discovery Today. — 2018. — Vol. 23(4). — P. 848-856.

79. Topka-Bielecka G, Dydecka A, Necel A, et al. Bacteriophage-derived depolymerases against bacterial biofilm / Topka-Bielecka G // Antibiotics. — 2021.

— Vol. 10(2). — P. 175.

80. Amankwah S, Abdella K, Kassa T. Bacterial biofilm destruction: a focused review on the recent use of phage-based strategies with other antibiofilm agents / Amankwah S // Nanotechnology, Science and Applications. — 2021. — Vol. 14. — P. 161-177.

81. Quan K, Hou J, Zhang Z, et al. Water in bacterial biofilms: pores and channels, storage and transport functions / Quan K // Crit Rev Microbiol. — 2022. — Vol. 48(3). — P. 283-302.

82. Figueiredo CM, Malvezzi Karwowski MS, et al. Bacteriophages as tools for biofilm biocontrol in different fields / Figueiredo CM // Biofouling. — 2021. — Vol. 37(6). — P. 689-709.

83. Markowska K, Szymanek-Majchrzak K, Pituch H, et al. Understanding Quorum-Sensing and Biofilm Forming in Anaerobic Bacterial Communities / Markowska K // Int J Mol Sci. — 2024. — Vol. 25(23). — P. 12808.

84. van Kessel JC, Mukherjee S. Another battle won in the phage-host arms race: *Pseudomonas* phage blocks quorum sensing regulator LaSR / van Kessel JC // Molecular Cell. — 2021. — Vol. 81(3). — P. 420-422.

85. Duddy OP, Silpe JE, Fei C, et al. Natural silencing of quorum-sensing activity protects *Vibrio parahaemolyticus* from lysis by an autoinducer-detecting phage / Duddy OP // PLoS Genetics. — 2023. — Vol. 19(7). — P. e1010809.

86. Patel H, Buchad H, Gajjar D. *Pseudomonas aeruginosa* persister cell formation upon antibiotic exposure in planktonic and biofilm state / Patel H // Scientific Reports. — 2022. — Vol. 12(1). — P. 16151.

87. Liu Y, Dai L, Dong J, et al. Covalent modifications of the bacteriophage genome

confer a degree of resistance to bacterial CRISPR systems / Liu YP // Journal of Virology. — 2020. — Vol. 94(23). — P. e01630-20.

88. Samson JE, Magadán AH, Sabri M, et al. Revenge of the phages: defeating bacterial defences / Samson JE // Nature Reviews Microbiology. — 2013. — Vol. 11(10). — P. 675-687.

89. Stokar-Avihail A, Fedorenko T, Hör J, et al. Discovery of phage determinants that confer sensitivity to bacterial immune systems / Stokar-Avhai A // Cell. — 2023. — Vol. 186(9). — P. 1863-1876.e16.

90. Watson BNJ, Steens JA, Staals RHJ, et al. Coevolution between bacterial CRISPR-Cas systems and their bacteriophages / Watson BNJ // Cell Host & Microbe. — 2021. — Vol. 29(5). — P. 715-725.

91. Kebriaei R, Lev KL, Shah RM, et al. Eradication of biofilm-mediated methicillin-resistant *Staphylococcus aureus* infections in vitro: bacteriophage-antibiotic combination / Kebriaei R // Microbiology Spectrum. — 2022. — Vol. 10(2). — P. e0041122.

92. Uchiyama J, Shigehisa R, Nasukawa T, et al. Piperacillin and ceftazidime produce the strongest synergistic phage-antibiotic effect in *Pseudomonas aeruginosa* / Uchiyama J // Archives of Virology. — 2018. — Vol. 163(7). — P. 1941-1948.

93. Liu C, Hong Q, Chang RYK, et al. Phage-antibiotic therapy as a promising strategy to combat multidrug-resistant infections and to enhance antimicrobial efficiency / Liu C // Antibiotics. — 2022. — Vol. 11(5). — P. 570.

94. Mukhopadhyay S, Zhang P, To KKW, et al. Sequential treatment effects on phage-antibiotic synergistic application against multi-drug-resistant *Acinetobacter*

baumannii / Mukhopadhyay S // International Journal of Antimicrobial Agents. — 2023. — Vol. 62(5). — P. 106951.

95. Loganathan A, Bozdogan B, Manohar P, et al. Phage-antibiotic combinations in various treatment modalities to manage MRSA infections / Loganathan A // Frontiers in Pharmacology. — 2024. — Vol. 15. — P. 1356179.

96. Kropinski AM, Clokie MR. Examination of bacteriophages / Kropinski AM // Methods in Molecular Biology. — 2009. — Vol. 502. — P. 21-30.

97. Hyman P, Abedon ST. Practical methods for determining phage growth parameters / Hyman P // Methods in Molecular Biology. — 2009. — Vol. 501. — P. 175-202.

98. O'Toole GA. Microtiter dish biofilm formation assay / O'Toole GA // J Vis Exp. — 2011. — Vol. 47. — P. 2437.

99. Krasowska A, Biegalska A, Augustyniak D, et al. Isolation and Characterization of Phages Infecting *Bacillus subtilis* / Krasowska A // Biomed Res Int. — 2015. — Vol. 2015. — P. 179597.

100. Bae HW, Choi SY, Ki HJ, et al. *Pseudomonas aeruginosa* as a model bacterium in antiphage defense research / Bae HW // FEMS Microbiol Rev. — 2025. — Vol. 49. — P. fuaf014.

101. Abramson J, Adler J, Dunger J, et al. Accurate structure prediction of biomolecular interactions with AlphaFold 3 / Abramson J // Nature. — 2024. — Vol. 630(8016). — P. 493-500.

102. Pfab J, Phan NM, Si D. DeepTracer for fast de novo cryo-EM protein structure modeling and special studies on CoV-related complexes / Pfab J // Proceedings of the National Academy of Sciences (PNAS). — 2021. — Vol. 118(2). — P. e2017525118.

103. Emsley P, Cowtan K. Coot: model-building tools for molecular graphics / Emsley P // Acta Crystallogr. Sect. D., Biol. Crystallogr. — 2004. — Vol. 60. — P. 2126-2132.

104. Adams PD, Afonine PV, Bunkóczi G, et al. PHENIX: a comprehensive Python-based system for macromolecular structure solution / Adams PD // Acta Crystallogr. Sect. D., Biol. Crystallogr. — 2010. — Vol. 66. — P. 213-221.

105. Ajisawa AJ. Dissolution of silk fibroin with calciumchloride/ethanol aqueous solution Studies on the dissolution of silk fibroin / Ajisawa AJ // Journal of Sericultural Science of Japan. — 1998. — Vol. 67. — P. 91-94.

106. Li C, Zhang M, Liu SY, et al. Chitin nerve conduits with three-dimensional spheroids of mesenchymal stem cells from sd rats promote peripheral nerve regeneration / Li C // Polymers. — 2021. — Vol. 13. — P. 3957.

107. Jin X, Xiang Z, Liu Q, et al. Polyethyleneimine-bacterial cellulose bioadsorbent for effective removal of copper and lead ions from aqueous solution / Jin X // Bioresource Technology. — 2017. — Vol. 244. — P. 844-849.

108. Schneider CA, Rasband WS, Eliceiri KW. NIH Image to ImageJ: 25 years of image analysis / Schneider CA // Nat Methods. — 2012. — Vol. 9(7). — P. 671-675.

109. Shchurova AS, Shneider MM, Arbatsky NP, et al. Novel *Acinetobacter baumannii* Myovirus TaPaz Encoding Two Tailspike Depolymerases: Characterization and Host-Recognition Strategy / Shchurova AS // Viruses. — 2021. — Vol. 13(6). — P. 978.

110. Valpuesta JM, Carrascosa JL. Structure of viral connectors and their function in bacteriophage assembly and DNA packaging / Valpuesta JM // Quart. Rev. Biophys.

— 1994. — Vol. 27. — P. 107-155.

111. Badaczewska-Dawid AE, Nithin C, Wroblewski K, et al. MAPIYA contact map server for identification and visualization of molecular interactions in proteins and biological complexes / Badaczewska-Dawid AE // Nucleic Acids Research. — 2022. — Vol. 50(W1). — P. W474-W482.

112. Krylov VN, Dela Cruz DM, Hertveldt K, et al. "phiKZ-like viruses", a proposed new genus of myovirus bacteriophages / Krylov VN // Arch Virol. — 2007. — Vol. 152. — P. 1955-1959.

113. Danilova YA, Belousova VV, Moiseenko AV, et al. Maturation of pseudo-nucleus compartment in *P. aeruginosa*, infected with giant phiKZ phage / Danilova YA // Viruses. — 2020. — Vol. 12. — P. 1197.

114. Laughlin TG, Deep A, Prichard AM, et al. Architecture and self-assembly of the jumbo bacteriophage nuclear shell / Laughlin TG // Nature. — 2022. — Vol. 608. — P. 429-435.

115. Zhang C, Zhang R, Yuan J. Potassium-mediated bacterial chemotactic response / Zhang C // eLife. — 2023. — Vol. 12. — P. RP91452.

116. Stewart PS. Mechanisms of antibiotic resistance in bacterial biofilms / Stewart PS // Int. J. Med. Microbiol. — 2002. — Vol. 292. — P. 107-113.

117. Strempel N, Neidig A, Nusser M, et al. Human host defense peptide LL-37 stimulates virulence factor production and adaptive resistance in *Pseudomonas aeruginosa* / Strempel N // PLoS One. — 2013. — Vol. 8. — P. e82240.

118. Yu Z, Kong Y, Luo Z, et al. Anti bacterial activity of mutant chensinin -1 peptide against multidrug resistant *Pseudomonas aeruginosa* and it effects on biofilm

associated gene expression / Yu ZY // Experimental and Therapeutic Medicine. — 2019. — Vol. 17(3). — P. 2031-2038.

119. Scarascia G, Yap SA, Kaksonen AH, et al. Bacteriophage Infectivity Against *Pseudomonas aeruginosa* in Saline Conditions / Scarascia G // Front Microbiol. — 2018. — Vol. 9. — P. 875.

120. Mirzaei A, Wagemans J, Nasr Esfahani B, et al. A phage cocktail to control surface colonization by *Proteus mirabilis* in catheter-associated urinary tract infections / Mirzaei A // Microbiology Spectrum. — 2022. — Vol. 10(5). — P. e0209222.

121. Wroe JA, Johnson CT, García AJ. Bacteriophage delivering hydrogels reduce biofilm formation in vitro and infection in vivo / Wroe JA // Journal of Biomedical Materials Research Part A. — 2020. — Vol. 108(1). — P. 39-49.

122. Meng XP, Sun JH. New insights into the control of bacterial biofilm: bacteriophage / Meng XP // Animal Husbandry & Veterinary Medicine. — 2010. — Vol. 42(1). — P. 97-101.

123. Alqahtani A. Bacteriophage treatment as an alternative therapy for multidrug-resistant bacteria / Alqahtani A // Saudi Medical Journal. — 2023. — Vol. 44(12). — P. 1222-1231.

124. Grygorcewicz B, Wojciuk B, Roszak M, et al. Environmental phage-based cocktail and antibiotic combination effects on *Acinetobacter baumannii* biofilm in a human urine model / Grygorcewcz B // Microbial Drug Resistance. — 2021. — Vol. 27(1). — P. 25-35.

11. Supplementary material

Table S1. Distances and possible interaction forces between amino acids of head-tail adapter and portal protein as calculated by MAPIYA.

Head-tail adapter	Amino acid #	Portal protein	Amino acid #	Distance, Å	Possible interaction forces
GLU	153	TYR	226	2.692	anion-π stacking,π-π stacking, electrostatic: ion-dipole, hydrogen bond
PHE	126	SER	244	3.067	dipole-π stacking
GLY	131	ASP	237	3.203	induction + dispersion
GLU	152	LYS	234	3.327	salt bridge, hydrogen bond
PHE	132	GLU	50	3.352	anion-π stacking
GLU	153	GLU	38	3.383	ionic repulsion
PHE	126	ASN	240	3.53	π-π stacking
GLY	131	ILE	233	3.593	hydrophobic
PHE	132	ILE	233	3.597	hydrophobic
GLN	130	ASP	237	3.628	electrostatic: ion-dipole, hydrogen bond
PHE	132	LYS	234	3.648	cation-π stacking
TYR	125	SER	244	3.676	electrostatic: dipole-dipole, hydrogen, bond,dipole-π stacking
PHE	132	SER	230	3.683	dipole-π stacking
GLY	129	ASP	237	3.729	induction + dispersion
PHE	132	TRP	229	3.789	π-π stacking, hydrophobic
ARG	128	ILE	241	3.818	induction + dispersion
PHE	126	ILE	241	4.006	hydrophobic
TYR	127	ILE	241	4.114	hydrophobic
GLU	152	GLU	38	4.400	ionic repulsion
TYR	127	ASP	237	4.600	anion-π stacking, π-π stacking, electrostatic: ion-dipole, hydrogen bond
GLU	150	LYS	234	4.645	salt bridge,hydrogen bond
GLY	131	GLU	50	4.841	induction + dispersion
PHE	132	ASP	237	4.852	anion-π stacking
ARG	128	ASP	237	4.853	salt bridge, hydrogen bond
GLN	154	GLU	38	4.858	electrostatic: ion-dipole, hydrogen bond
GLU	153	PRO	36	4.959	induction + dispersion

Table S2. Distances and possible interaction forces between amino acids of head completion and head-tail adapter as calculated by MAPIYA.

Head completion	**Amino acid #**	**Head-tail adapter**	**Amino acid #**	**Distance, Å**	**Possible interaction forces**
LYS	9	GLU	71	2.594	salt bridge, hydrogen bond
GLU	112	GLN	70	2.612	electrostatic: ion-dipole,hydrogen bond
LYS	6	ASP	25	2.881	salt bridge,hydrogen bond
HIS	110	VAL	68	3.035	induction + dispersion
TRP	48	GLN	70	3.184	hydrogen bond, π-π stacking, dipole-π stacking
SER	69	GLU	71	3.185	electrostatic: ion-dipole,hydrogen bond
SER	3	GLU	71	3.223	electrostatic: ion-dipole,hydrogen bond
THR	5	GLU	71	3.345	electrostatic: ion-dipole, hydrogen bond
TYR	104	GLY	69	3.413	hydrophobic
GLY	108	VAL	68	3.416	hydrophobic
PHE	107	VAL	68	3.487	hydrophobic
HIS	110	GLU	71	3.519	salt bridge, hydrogen bond,anion-π stacking
PHE	107	GLN	66	3.57	π-π stacking
VAL	4	GLN	66	3.581	induction + dispersion
GLU	112	GLY	69	3.581	induction + dispersion
TYR	104	VAL	68	3.611	hydrophobic
LYS	6	ASP	22	3.675	salt bridge, hydrogen bond
TRP	67	GLN	70	3.752	hydrogen bond, π-π stacking, dipole-π stacking
GLU	112	VAL	68	3.847	induction + dispersion
VAL	4	ALA	73	3.866	hydrophobic
GLU	112	GLU	71	3.875	ionic repulsion
VAL	4	GLU	71	3.964	induction + dispersion
THR	5	GLU	72	3.997	electrostatic: ion-dipole, hydrogen bond
THR	5	ALA	73	4.015	induction + dispersion
VAL	4	LEU	75	4.025	hydrophobic
PHE	107	ARG	67	4.237	cation-π stacking
HIS	110	GLN	70	4.349	electrostatic: ion-dipole, hydrogen bond
HIS	110	GLY	69	4.39	induction + dispersion
SER	70	GLU	71	4.65	electrostatic: ion-dipole, hydrogen bond

VAL	4	GLU	72	4.772	induction + dispersion
PHE	41	TYR	24	4.987	π-π stacking, hydrophobic, dipole-π, stacking

Table S3. Distances and possible interaction forces between amino acids of tail terminator and head completion as calculated by MAPIYA.

Tail terminator	**Amino acid #**	**Head completion**	**Amino acid #**	**Distance, Å**	**Possible interaction forces**
VAL	28	TYR	25	2.241	hydrophobic
ARG	25	GLU	29	2.33	salt bridge, hydrogen bond
LEU	22	GLY	28	2.894	hydrophobic
ASN	26	TRP	30	3.117	hydrogen bond, π-π stacking, dipole-π stacking
ALA	31	GLY	80	3.173	hydrophobic
GLU	29	HIS	79	3.19	salt bridge, hydrogen bond,anion-π stacking
ILE	8	ASP	27	3.236	induction + dispersion
PHE	20	GLY	28	3.238	hydrophobic
ASN	124	HIS	79	3.278	electrostatic: ion-dipole hydrogen bond,π-π
VAL	28	ARG	78	3.331	induction + dispersion
LEU	22	GLU	29	3.344	induction + dispersion
GLU	29	GLY	80	3.376	induction + dispersion
ASN	26	GLU	85	3.442	electrostatic: ion-dipole hydrogen bond
GLY	27	TRP	30	3.466	hydrophobic
ALA	31	THR	81	3.478	induction + dispersion
GLN	12	ASP	27	3.557	electrostatic: ion-dipole hydrogen bond
VAL	28	LEU	84	3.588	hydrophobic
PRO	30	GLY	80	3.603	hydrophobic
ILE	21	TYR	25	3.631	hydrophobic
VAL	28	GLU	85	3.644	induction + dispersion
ILE	21	GLY	28	3.685	hydrophobic
GLU	29	PRO	83	3.700	induction + dispersion
VAL	28	PRO	83	3.805	hydrophobic
ILE	8	GLY	28	3.83	hydrophobic
GLY	27	TYR	25	3.835	hydrophobic
LYS	19	TYR	25	3.844	cation-π stacking,hydrogen bond

VAL	28	HIS	79	3.853	induction + dispersion
PRO	30	TYR	25	4.033	hydrophobic
VAL	28	TRP	30	4.046	hydrophobic
VAL	28	ALA	77	4.085	hydrophobic
GLU	29	TYR	25	4.107	anion-π stacking,π-π stacking, electrostatic
GLU	4	GLU	29	4.23	ionic repulsion
GLN	12	GLY	28	4.255	induction + dispersion
ARG	25	TRP	30	4.272	cation-π stacking
LEU	22	ASP	27	4.385	induction + dispersion
PHE	20	TYR	25	4.453	π-π stacking, hydrophobic, dipole-π stacking
GLY	27	GLU	85	4.548	induction + dispersion
PRO	30	PRO	83	4.636	hydrophobic
PRO	30	HIS	79	4.707	induction + dispersion
ARG	25	GLY	28	4.758	induction + dispersion
GLU	29	ARG	78	4.911	salt bridge, hydrogen bond